ASYMMETRY DEPENDENCE OF SPECTROSCOPIC FACTORS: A STUDY OF TRANSFER REACTIONS ON ARGON ISOTOPES AT 70 MEV/U

By

Juan José Manfredi Jr.

A DISSERTATION

Submitted to
Michigan State University
in partial fulfillment of the requirements
for the degree of

Physics — Doctor of Philosophy

2018

ABSTRACT

ASYMMETRY DEPENDENCE OF SPECTROSCOPIC FACTORS: A STUDY OF TRANSFER REACTIONS ON ARGON ISOTOPES AT 70 MEV/U

By

Juan José Manfredi Jr.

Nuclear reactions are useful tools to study the structure of the atomic nucleus. One of the most popular reactions over the last several decades is the transfer reaction, and the advent of rare isotope beam facilities has opened up new swaths of the nuclear chart available for exploration with this technique. In principle, different techniques should give consistent nuclear structure information (like the spectroscopic factor which quantifies single-particle occupancy) for a given isotope. However there is a well-established discrepancy between spectroscopic factors extracted from transfer reaction data and those extracted from knockout reaction data. In particular, reduction factors (ratios of extracted spectroscopic factors to theoretical expectation) from knockout data show a strong dependence on nuclear asymmetry, whereas the transfer measurements show at most a weak dependence. This discrepancy not only raises important questions on the influence of nucleon-nucleon correlations in nuclear structure, but also calls into question the validity of the relevant nuclear reaction techniques.

This dissertation describes the measurement of the $^{34}\mathrm{Ar}(p,d)^{33}\mathrm{Ar}$ and $^{46}\mathrm{Ar}(p,d)^{45}\mathrm{Ar}$ single-neutron transfer reactions at 70 MeV/u. The motivation of this study is to measure the same transfer reactions on argon examined in earlier work at low energy, while matching the high beam energy of previous knockout measurements on argon. Raising the beam energy to a regime where few reliable measurements exist could illuminate potential defects in the transfer reaction mechanism. We performed a kinematically complete measurement

of the differential cross sections for these (p, d) reactions at the National Superconducting Cyclotron Laboratory using several detector systems. The High Resolution Array (HiRA) detected the outgoing deuterons, the S800 Spectrograph detected the heavy argon recoil, and two Microchannel Plates (MCPs) tracked the incoming beam to normalize the cross section and to better localize the transfer on the reaction target. We carried out various calibrations on each individual detector system (including a detailed characterization of silicon detectors in HiRA) before merging and normalizing the data to generate the cross sections of interest.

We extracted spectroscopic factors using the adiabatic distorted wave approximation (ADWA) framework implemented in the TWOFNR code. Both the CH89 global optical potential as well as the microscopic Jeukenne, Lejeune, and Mahaux (JLM) optical potential produced spectroscopic factors for each reaction system. The resulting reduction factors corroborate the low-energy results and disagree with the knockout data by showing a weak asymmetry dependence between the neutron-rich ^{46}Ar and the proton-rich ^{34}Ar. Therefore, the transfer reaction mechanism yields consistent results even at a high beam energy. We advocate for further transfer reaction measurements at high asymmetry, as well as a deeper theoretical understanding of both the transfer and knockout reaction mechanisms.

ACKNOWLEDGMENTS

Having come to the end of this challenging endeavor called graduate school, I find myself in a grateful mood. Although my name is on the title page of this dissertation, the work presented here would have been impossible without the help of many amazing people. I hope the reader will indulge me as I do my best to express sincere appreciation to them.

First, I would like to express my utmost gratitude to Professor Betty Tsang, my advisor. I have relied heavily on her support and wisdom, especially during the most trying times of my graduate career. Enumerating all the lessons I learned from her would take an entire chapter of this thesis, but I have especially admired her tenacity in the face of challenges, her organized approach, and her willingness to search out and open doors for her students. I will forever be grateful for her patience and guidance during my scientific education.

I would also like to thank Professor Bill Lynch, who advised me extensively over the last several years. From him I learned the extraordinary value of asking simple questions, as well as how to solve a problem by breaking it down into its most basic components. I must also thank him for his patience in helping me with my research, despite my occasional stubbornness.

In addition to Profs. Tsang and Lynch, I would like to thank Profs. Wolfgang Mittig, Ed Brown, and Norman Birge for serving on my dissertation guidance committee. I have sincerely appreciated their advice and their ability to keep in mind the big picture of my graduate career trajectory to ensure the timely completion of my degree.

Of course, I am extraordinarily grateful for my funding sources. From 2013 to 2017, I had the privilege to participate in the Department of Energy National Nuclear Security Administration Stewardship Science Graduate Fellowship. I am indebted to this fellowship

for funding that allowed me to perform this thesis work, as well as professional opportunities (like the chance to spend three months at Lawrence Livermore National Laboratory) and a fantastic network of fellows. I would especially like to thank the Krell Institute for administering the fellowship and providing excellent support over the years. I also thank the National Science Foundation for their continued support of rare isotope research at the NSCL, and the Graduate School for funding during my final year. I wish to thank Kim Crosslan for her help in navigating the sometimes confusing bureaucracy of Michigan State, as well as for her encouragement.

Fortunately, I have enjoyed many exceptional classes during my time at Michigan State. In particular I would like to thank Profs. Morten Hjorth-Jensen, Filomena Nunes, Norman Birge, Dave Morrissey, Mark Iwen, Paul Mantica, and Wade Fisher for teaching excellent courses. I would also like to thank Prof. Brian O'Shea for advising me in my pursuit of a CMSE graduate certificate, as well as supervising my independent study. I thank Prof. Saul Beceiro Novo (as well as the ISEE PDP program) for teaching me about teaching. Of course, I also owe a debt of gratitude to the many excellent teachers I had before arriving at MSU. Thank you to Profs. Guido Weiss and Jason Woods for guiding me through my mathematics and physics college coursework. Thank you also to Prof. Demetrios Sarantites, Mrs. Yacamelli, Mr. Matusiak, and Mr. Zellmer for having a particularly large impact on my development as a student.

I have had the privilege of working with many incredible people as part of the HiRA group. I am grateful for the mentorship of Prof. Zbigniew Chajecki early in my graduate career, as well as for his patience in helping me learn the basics of experimental science. I would like to thank Dr. Kyle Brown for his collaboration during my thesis experiment, his advice on difficult analysis issues, and for many years of his friendship and office visits. I

have valued working with other post-docs as well, especially Drs. Rebecca Shane, Pierre Morfouace, Giordano Cerizza, Genie Jhang, and Daniele Dell'Aquila. Working with the other graduate students of the group has also been a privilege. I would like to thank Dr. Jack Winkelbauer and Dr. Rachel Hodges Showalter for helping me learn the ropes of the HiRA group as well as for their assistance running my experiment. I would also like to thank Jon Barney and Justin Estee for playing important roles in running my thesis experiment, and also for their valued friendship. Special thanks to Jon for giving me a cat, and to Justin for showing me how much fun Japanese baseball games are. I am grateful for the chance to have worked with the younger students in the group, including Sean Sweany, Zhu Kuan, Tommy Tsang, and Chi-En Teh: as I leave it is nice to know that the HiRA group is in good hands. I would also like to thank the many excellent undergraduates who have passed through our group, especially Corinne Anderson for her role in the CsI crystal repair project.

It is difficult to overstate how tremendously lucky I am to have worked at the NSCL. Nuclear physics is a team sport, and the team at the NSCL is second to none. In particular I would like to thank Dr. Tom Ginter, Dr. Daniel Bazin, Craig Snow, Cody Norat, Dr. Dave Sanderson, the safety office, the cyclotron operators and Dr. Jeremy Tompkins for their help in running my thesis experiment. I am thankful to Profs. Remco Zegers, Artemis Spyrou, and Michael Thoennessen for their sincere effort to make the lab a welcoming and healthy place for students to do excellent science. Thank you to the lab leadership, who have fostered an incredible scientific environment, and will certainly continue to do so in the upcoming transition to FRIB.

The research described herein was only possible with the help of many amazing scientists around the world. First of all, I must express my most sincere gratitude to Prof. Jenny Lee, who originally proposed the measurement described in this thesis. Beyond serving as

the PI of the experiment, her work is the foundation that this dissertation is built upon. I am incredibly grateful for her invitation to come work with her in Hong Kong for an entire summer. I would also like to thank Prof. Andy Rogers for all of his work during the experimental setup, as well as for his collaboration developing the analysis code. Thank you to all the other people who collaborated on running the experiment, especially Dr. Zhengyu Xu, Cole Pruitt, Jon Elson, Prof. Lee Sobotka, Prof. Zbigniew Chajecki, Dr. Karl Smith, and Prof. Zhigang Xiao. I also thank Chenyang Niu for his analysis collaboration on the E detector characterization (as well as for his hospitality during my visit to Beijing). I am grateful to the theorists who took the time to help me understand the details of reaction theory, in particular Prof. Jeff Tostevin, Dr. Gregory Potel, and Prof. Filomena Nunes.

I must take a moment to especially thank Prof. Lee Sobotka at Washington University for serving as an absolutely fantastic undergraduate advisor. I am tremendously grateful that he responded to the email I sent him in my freshman year of college asking about research opportunities. I certainly do not exaggerate when I say that I would not be where I am today without his advice and support. I would also like to thank Prof. Robert Charity for teaching me about ROOT during my undergraduate years.

One of the best features of the NSCL is the vibrant graduate student community which has allowed me to avoid the feelings of isolation that graduate students sometimes experience. Thank you to all the graduate students I have had the privilege to interact with over the past six years here at Michigan State. I am in particular grateful to Dr. Chris Prokop for years of friendship as roommates, as well as to Dr. Sam Lipschutz for ensuring that a boring day never transpired at the NSCL. I am thankful to my wonderful officemates, especially Dr. Wei Jia Ong, Zach Matheson, Katie Childers, and honorary officemember Becky Lewis. Outside of the NSCL, I am thankful to Dr. Connor Glosser for his friendship and for showing

me the best places to eat and drink in the Lansing area.

Despite what it feels like, I did not spend every minute of my time in graduate school working on this thesis. I am grateful to Zach Constan for giving me the chance to engage in science outreach both for the satisfaction of pursuing a noble mission as well as the practical benefits of improved communication skills. I would also like to thank everyone at WaMPS for organizing so many fantastic outreach events, and for bringing to life the SL@MS program. My participation in organizations outside of science, especially Crossing Water, Michigan for Bernie, and MSU Men's Volleyball, kept me sane during the long slog of graduate school and introduced me to incredible people and lifelong friends.

Most importantly, I would like to thank my incredible family. My father taught me the importance and the beauty of science, and I would not have pursued this degree (or persevered until the end) without his guidance. My mother is the kindest person I know, and raised me to respect myself and others. My little sister always makes me laugh and also inspires me with her perseverance through difficult circumstances. And, of course, I must thank our dog. I would also like to thank my extended family in Spain and Argentina. Although we are literally oceans apart, I feel the powerful influence of their love and support in my daily life: gracias! Last but not least, my partner continues to inspire me each and every day, and I am not sure this endeavor would have been possible without the personal growth she has inspired within me. Her support, as well as that of our precious cat, during the trials and tribulations of graduate school has proven inestimably important. Thank you.

TABLE OF CONTENTS

LIST OF TABLES

LIST OF FIGURES

Chapter 1

Introduction

I, a universe of atoms, an atom in the universe.

Richard Feynman

1.1 The Atomic Nucleus

The world around us is made of *atoms*. Since Democritus first theorized the existence of the atom in ancient Greece, science has ventured within this building block of matter to study its secrets. Each atom consists of a *nucleus* made up of protons (that have positive electric charge) and neutrons (no electric charge) surrounded by a cloud of negatively-charged electrons. Ernest Rutherford's 1911 discovery of the atomic nucleus immediately made clear two of its remarkable properties [1]. First, the nucleus is heavy, making up over 99.9% of the total mass of the atom. Protons and neutrons, collectively referred to as nucleons, are much heavier than electrons, and therefore constitute almost all the mass of ordinary matter. Secondly, the nucleus is small. Typically the radius of the atom is more than 10,000 times bigger than the nuclear radius. This extraordinarily dense collection of interacting neutrons and protons contains a rich and complex set of phenomena that is the focus of *nuclear physics*.

Since the positively-charged protons in the nucleus repel each other via the electrical force, there must be another force overpowering this repulsion to bind the nucleons together.

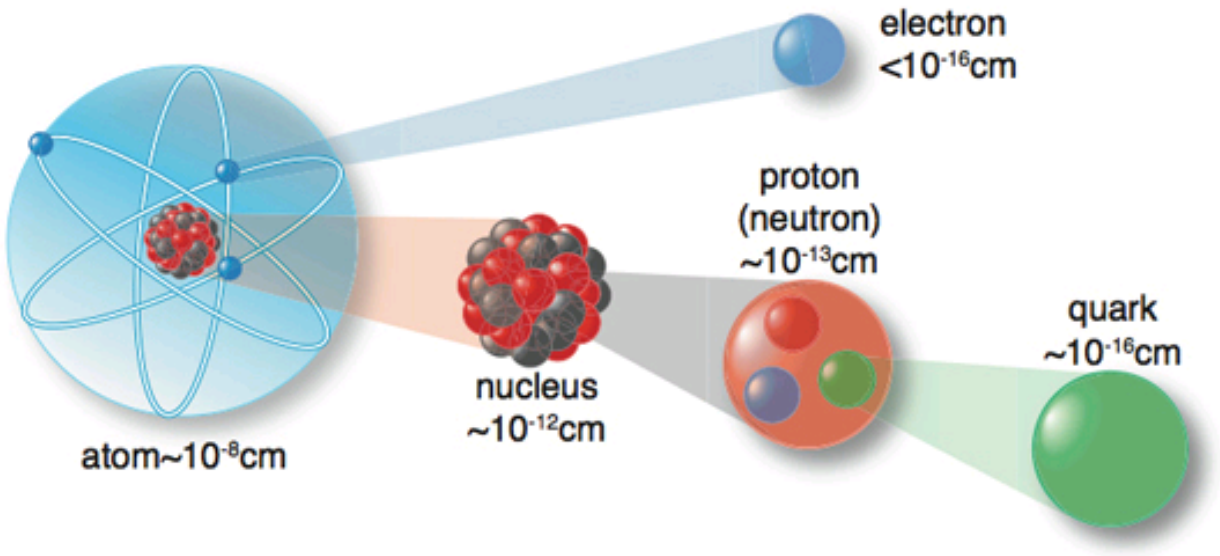

Figure 1.1: Components of an atom (from [2]).

This *nuclear force* is a residual effect of the strong interaction between the constituent quarks that make up protons and neutrons, as shown in Figure 1.1 [2]. The aptly-named strong force is the most powerful fundamental force in the universe, and the source of energy tapped by nuclear energy and nuclear weapons.

Although the exact mathematical form of the nuclear force is not known, we do know that this force acts only at very short distances. In contrast, the electrostatic force (also called the Coulomb force) acts at long distances. The balance between short-range nuclear attraction and long-range Coulomb repulsion limit the possible configurations of neutrons and protons that form into allowed nuclei. Figure 1.2 shows the landscape of possible nuclei, known as the *chart of the nuclides* [3]. Each square represents a single isotope, denoted by proton number on the y-axis and neutron number on the x-axis. The black squares indicate *stable* nuclei that make up most of the ordinary matter on Earth, and are collectively referred to as *the valley of stability*. The green squares indicate all other observed nuclei, which are *unstable* (also called exotic or rare) and will eventually decay towards the valley of stability.

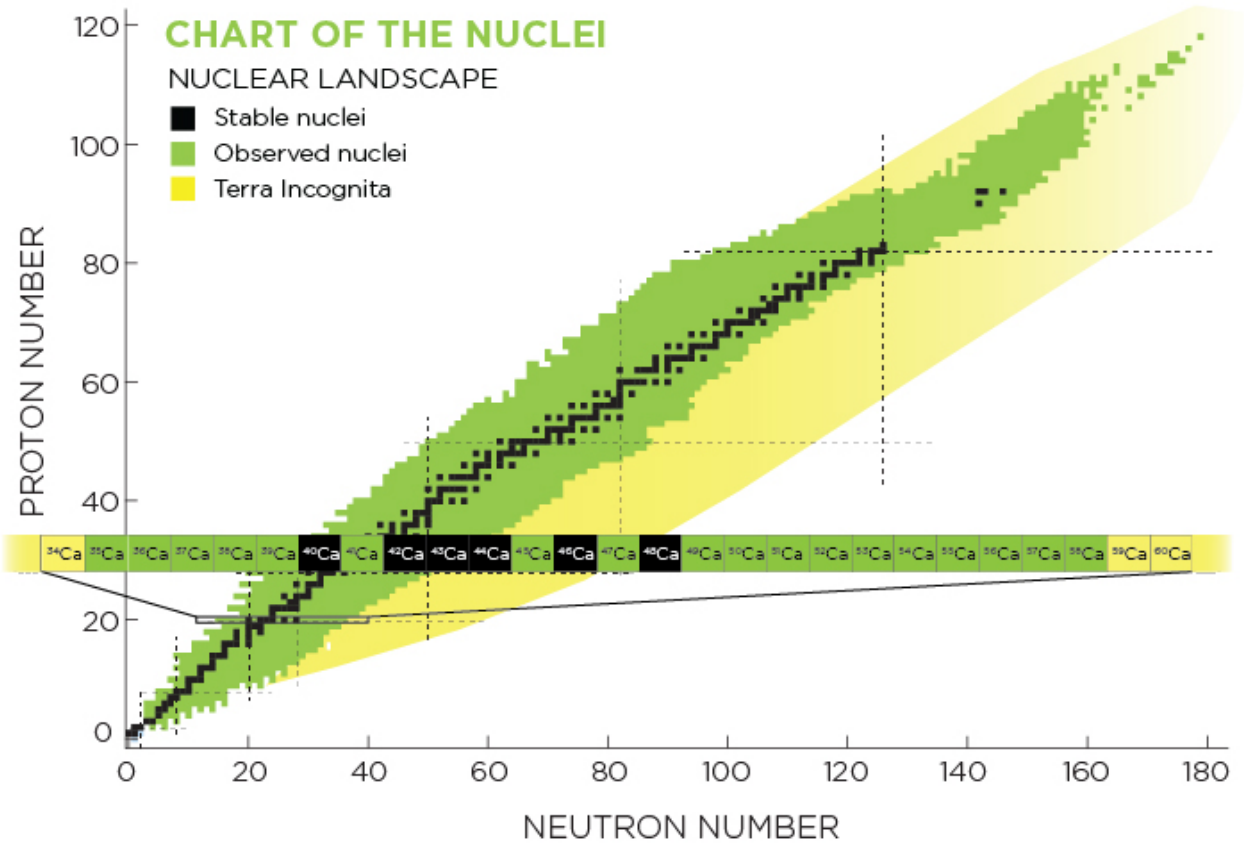

Figure 1.2: Chart of the nuclides, with neutron number on the x-axis and proton number on the y-axis. The chain of calcium isotopes is magnified, showing that calcium can vary from proton-rich to neutron-rich. Taken from [3].

The largest region of the chart (in yellow) remains unexplored.

The number of protons in a nucleus (given by Z) determines its element, and each element has a variety of *isotopes* determined by neutron number (given by N). An isotope is typically represented as ${}^{A}X$, where $A = N+Z$ is the *mass number* of the nucleus and X is the chemical symbol for its corresponding element. In Figure 1.2, the calcium isotopic chain ($Z = 20$) is enlarged to show the variety of isotopes possible for a single element. Some isotopes, like ^{35}Ca have a relatively low number of neutrons (proton-rich) and others, like ^{58}Ca have a relatively high number of neutrons (neutron-rich).

A central theme of modern nuclear physics research is understanding these exotic nuclei

on both the proton-rich and neutron-rich sides of the chart. Producing rare isotopes is challenging, so the American nuclear physics community has coordinated the construction of large accelerator facilities, like the National Superconducting Cyclotron Laboratory (NSCL) and the upcoming Facility for Rare Isotope Beams (FRIB), to create and study rare isotopes. Researchers from all over the world use these rare isotope factories to address important questions about nuclear physics. For instance, what are the properties of exotic nuclei away from the valley of stability? How do nuclei on one side of an isotopic chain (e.g. ^{35}Ca) behave differently from nuclei on the other side (e.g. ^{58}Ca)? And what is the best way to study these properties? This dissertation will focus on addressing such issues. First, we must formulate these questions more precisely via a basic introduction to *nuclear structure*, the study of how protons and neutrons arrange themselves in the nucleus.

1.2 Inside the Nucleus

Unlike macroscopic objects (like planets, cars, or human beings), nuclei are too small to be accurately described by Newton's Laws. Instead, nuclei obey the laws of quantum mechanics, in which objects have properties of both particles and waves, and quantities like energy and momentum are restricted to discrete values. A quantum system can exist in a superposition of these discrete states, and so the complexity of a nucleus with A nucleons rises very quickly with A. As a result, treating an arbitrary nucleus exactly as a quantum many-body problem is an extraordinarily challenging, and often impossible, task from both the analytical and the computational point of view.

Given the difficulty of solving this problem exactly, nuclear physicists employ different approximations in order to further theoretical understanding of the nucleus and to make

sense of experimental observations. An early example of such an approach is the Bethe-Weizsäcker formula, first published in the 1930s, based on the liquid drop model (LDM) of the nucleus [4, 5]. The LDM considers the nucleus as a drop of incompressible fluid made up of neutrons and protons, similar to a drop of water made up of H_2O molecules [6, 7]. The Bethe-Weizsäcker formula puts the LDM in quantitative form with only five terms to calculate the binding energy for a particular nucleus[1]; these terms relate to the volume, surface area, Coulomb repulsion of constituent protons, neutron-proton asymmetry, and nuclear pairing energy contributions [4, 5, 9]. Despite its simplicity, this formula successfully describes broad trends in nuclear binding energy, putting early mass measurements into useful theoretical context.

The LDM's intuitive appeal outweighs its predictive power. For instance, experimental evidence showed that nuclei with certain numbers of neutrons or protons (2, 8, 20, 28, 50, 82, and 126) have excess binding energy compared to values predicted by the Bethe-Weizsäcker formula [10, 11, 12, 13]. Eugene Wigner, intrigued by the discrepancy, referred to these points of extra stability as *magic numbers*, which is how they have subsequently been referred to since then [13].

In 1949, Marie Goeppert-Mayer and Hans Jensen left behind the LDM to develop the first *shell model* of the nucleus, shedding light on the mystery of these magic numbers [14, 15, 16]. The shell model had a transformative impact on nuclear physics, and to this day is the most successful and robust nuclear structure framework. Mayer and Jensen were awarded the Nobel Prize in 1963 for their work.

The simplest shell model is called the Independent Particle Model (IPM). The central idea

[1]The binding energy of a nucleus is the minimum energy required to dismantle that nucleus. By Einstein's principle of mass-energy equivalence, the binding energy can also be expressed as a mass with the relation $E = mc^2$ [8]. In the present discussion, binding energy and mass will be used interchangeably.

of the IPM is the assumption that each nucleon moves in a *mean-field* potential independently from all the other nucleons. This potential is meant to represent the average influence on one particular nucleon from all the others, and is typically defined in a harmonic oscillator or Woods-Saxon form [12, 16]. In the mean field, each nucleon occupies a single-particle eigenstate *orbital* characterized by its discrete energy and quantum numbers n, l, and j, where n is the number of nodes in the radial wave function, and l and j are the orbital and total angular momenta. Figure 1.3 shows these orbitals for different choices of the potential. Due to the Pauli exclusion principle no two nucleons can occupy the same quantum state, and the lowest energy configuration comes from filling in orbitals from the bottom up [17]. Protons and neutrons fill orbitals independently. Groups of orbitals with similar quantum numbers and energies are called *shells*.

In Figure 1.3 we see that the IPM predicts energy gaps between separate shells. Therefore exciting a nucleon to a higher energy orbital in a nucleus with a fully occupied, or closed, shell bears a large energy cost. This is exactly what results in extra stability for nuclei with a magic number of neutrons or protons (or both), and each magic number corresponds to a fully-occupied shell of single-particle orbitals. Using a simple mean-field potential with an added spin-orbit component (see the rightmost column in Fig. 1.3), the IPM can reproduce all the magic numbers listed above [12, 16].

The IPM essentially substitutes a very difficult A-body problem with A more tractable single-body problems. In fact, we typically solve far less than A single-body problems, as we also assume that only the highest energy (or *valence*) orbitals dictate nuclear structure properties due to the inert nature of the filled inner shells. Although these assumptions substantially reduce the number of degrees of freedom, the IPM performs quite well. In addition to reproducing the magic numbers, the IPM also provides the correct ordering of

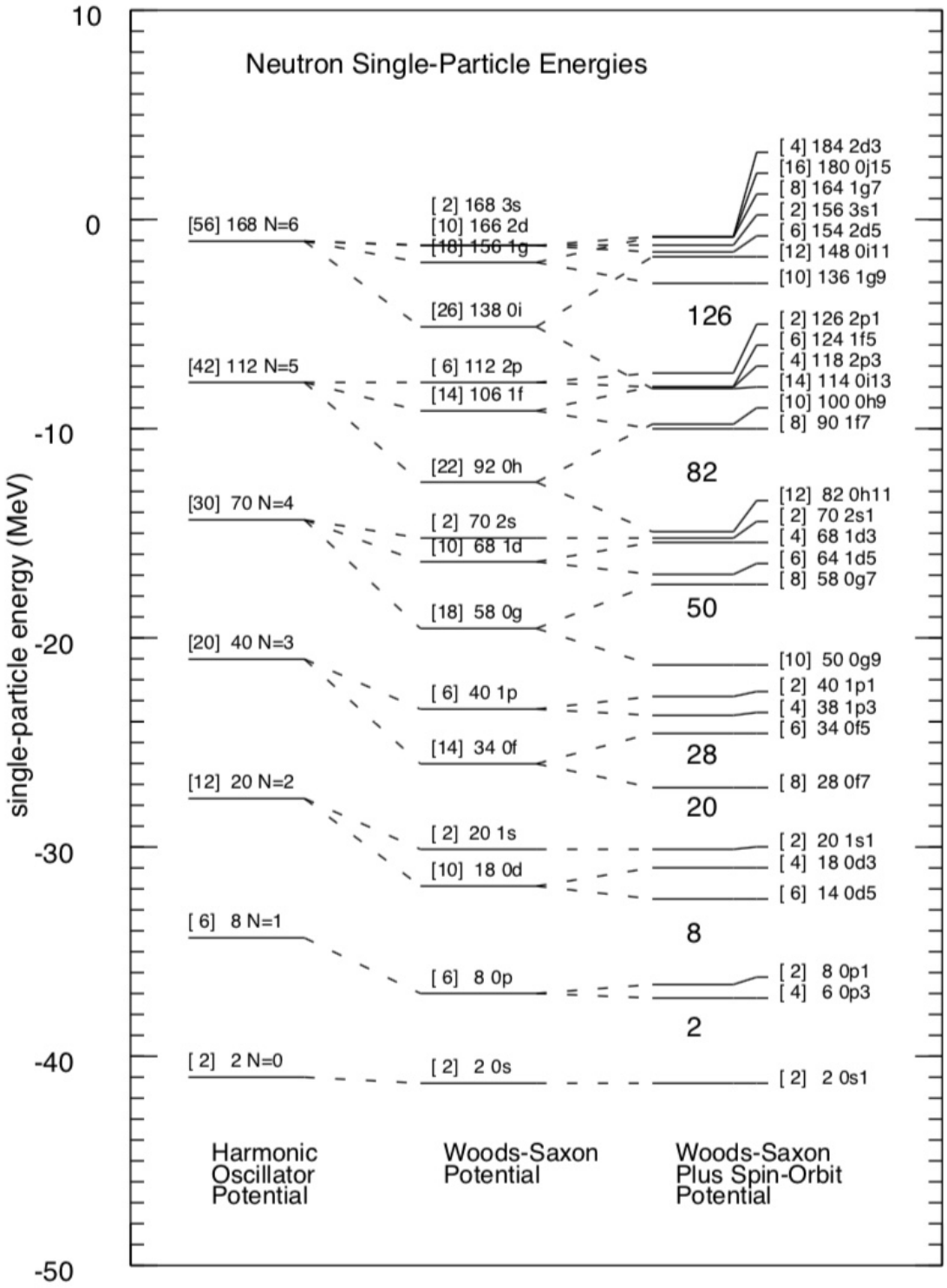

Figure 1.3: Single-particle orbitals generated by various mean-field potentials. Figure taken from [12].

single-particle states for the vast majority of stable nuclei, and a basic description of their static and dynamic properties [18].

This mean field approach provides a useful basic framework for nuclear structure, but the IPM does not generalize well beyond closed-shell nuclei. One reason is the influence of nucleon-nucleon correlations. Short-range correlations, due to strong repulsion between nucleons at very short distances, push nucleons to higher-momentum orbitals [19, 20]. Long-range correlations between valence nucleons result in collective behavior like deformation and giant resonances [21]. Both short and long range correlations disrupt the IPM mean field picture, reducing the occupancy of single-particle orbitals [22, 23]. More sophisticated models, like the large-basis shell model (LBSM), can account for some of these correlation effects (mostly of the long range variety) by expanding to a larger single-particle model space to describe configuration mixing in the valence states, or by using specialy designed effective interactions [22, 24]. Still, they are based on the foundation set by the mean-field theory of Mayer and Jensen.

We are interested in evaluating how well state-of-the-art shell models actually describe reality using experimental data. Which orbitals are occupied in a given nucleus, and to what extent? How does this orbital structure change away from the valley of stability? And for that matter, what type of data can we use to compare to theory? In the next section, we will discuss one potential point of contact between experimental data and nuclear structure theory.

1.3 Understanding Nuclear Structure

The occupancy of a single-particle orbital in a particular state of a given nucleus is quantified by its *spectroscopic factor* (SF) [25]. This quantity is defined as follows:

$$\mathrm{SF} = \int d\vec{p} \left| \left\langle \Psi^{A-1} \middle| a_{\vec{p}} \middle| \Psi^{A} \right\rangle \right|^2 \tag{1.1}$$

where $\vec{p}$ is the set of quantum numbers for a particular single-particle orbital and Ψ^X is a wave function for an X-nucleon system. The annihilation operator $a_{\vec{p}}$ acts on a wave function to remove a nucleon in that single-particle state. SFs can be calculated directly from shell model wave functions, and range from 0 (no overlap between Ψ^{A-1} and $a_{\vec{p}}\Psi^A$) to $2j+1$ (perfect overlap) where j is the total angular momentum of $\vec{p}$. Normalizing to a maximal value of 1, the SF can be interpreted as the probability that given an A-body wave function Ψ^A, removing a nucleon in state $\vec{p}$ will yield a particular $A-1$-body core configuration Ψ^{A-1}. In this work, we will normalize SFs to $2j+1$.

Figure 1.4 illustrates this concept with an example. For the ground state of ^{41}Ca, the spectroscopic factor of the $f_{7/2}$ orbital is approximately 1 [26]. This means that we can consider ^{41}Ca as consisting of a doubly-magic (Z=20, N=20) core with an extra single neutron fully occupying the $f_{7/2}$ orbital. In this instance, the single-particle orbital is fully occupied due to the stability of the inert core. For many other cases SFs will have sub-maximal values, indicating the presence of nucleon-nucleon correlations disrupting the simple picture of a single-particle in a mean field.

Spectroscopic factor calculation depends on details of the chosen Hamiltonian and basis states used to define the wave functions [27, 28]. Therefore, the SF is not a true observable and cannot be directly measured in the same way as an energy or cross section. Instead, the

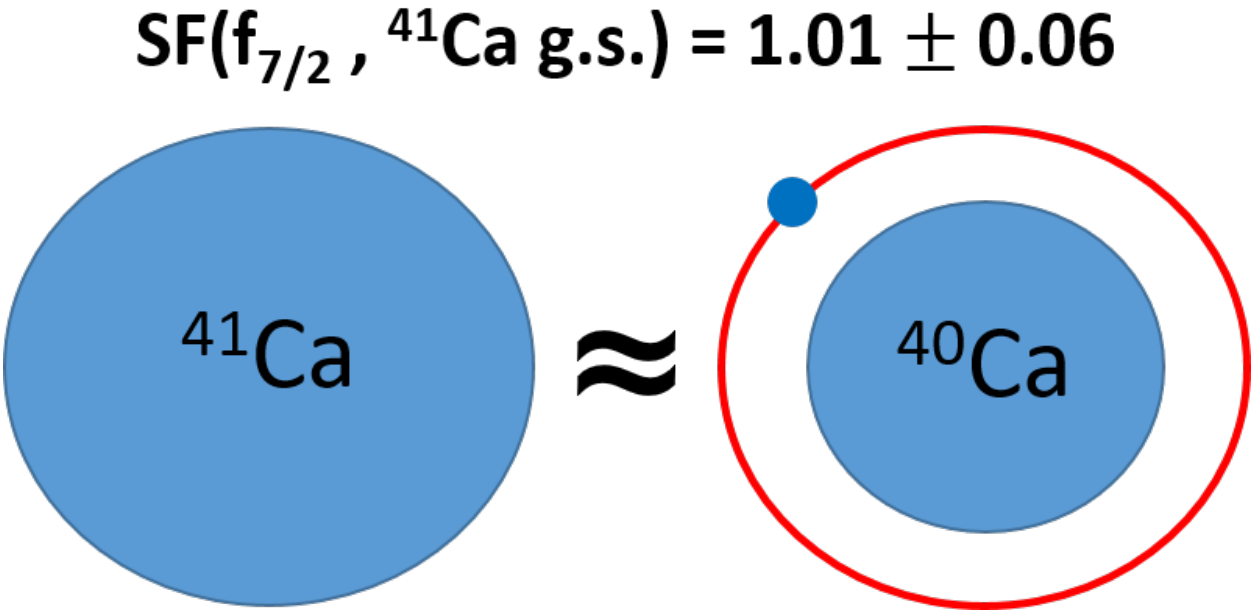

Figure 1.4: Structure of ^{41}Ca.

standard procedure is to first induce a nuclear reaction on the nucleus of interest and measure an observable quantity (e.g. reaction cross section). Experimental spectroscopic factors must then be *extracted* from data via comparison of this observable to nuclear reaction theory [27]. The specific extraction procedure depends on the chosen reaction probe, but the general idea is to use reaction theory to calculate the expected observable *assuming the orbital of interest is fully occupied*. Then the ratio of the experimental observable to the calculated observable gives a measure of the actual orbital occupancy. This will be discussed further in Chapter 2. The ratio of the resulting experimental SF to the SF from nuclear structure theory is called the *reduction factor* (typically denoted R or R_s), and quantifies how well the theory describes the actual nuclear structure.

In the literature, some discuss whether the non-observability of the SF prevents it from being a valid measure of nuclear structure [28, 29, 30]. Ultimately, many studies have shown that meaningful information can be gleaned from SFs within a systematic extraction

approach [23, 31, 32, 33, 34, 35], including the work of Tsang, Lee, and Lynch in which they re-analyzed transfer reaction data from 80 nuclei within a consistent theoretical framework to extract SFs [36, 37, 38]. A single SF in isolation suffers from high theoretical uncertainty, but comparing SFs from several nuclear states extracted in a similar way from similar data can yield real insight about the structure within. Consider the previous example of ^{41}Ca: the SF ranges from 0.75 to 1.06 depending on the optical potential used for the reaction model in the extraction. However, the SF *trend* across many calcium isotopes is consistent for different optical potentials as well as IPM calculations [39].

Several types of nuclear reactions can be used to access SFs. One possibility is the $(e, e'p)$ electron scattering reaction, in which a high-energy electron scatters off a stationary target nucleus and knocks loose a proton in the process. The major advantages of $(e, e'p)$ are that it penetrates the nuclear interior and that it occurs via the well-understood electromagnetic interaction. In principle, using an electromagnetic probe rather than a hadronic one reduces theoretical uncertainty related to our less developed understanding of the nuclear force compared to the electromagnetic force. The results from $(e, e'p)$ data show substantial reduction ($R \approx\ 0.6 - 0.7$) compared to the IPM for stable nuclei across a wide mass range [40]. This indicates significant influence from nucleon-nucleon correlations. When compared to other nuclear structure models, the reduction fluctuates [39].

Unfortunately, the $(e, e'p)$ technique does not easily apply to the study of rare isotopes. First of all, electron scattering cannot access particle states (for which nucleons must be added rather than removed from the nucleus) or hole states involving neutron removal. More importantly, most rare isotopes are too difficult to produce and too short-lived to serve as targets in an electron scattering experiment. Instead, we need reaction mechanisms that allow for the study of isotopes in an accelerated beam.

Transfer reactions, in which a nucleon is transferred from one nucleus to another, have been a popular choice for extracting SFs since the 1950s [41, 42, 43]. Transfer reactions experiments can study both hole and particle states, selectively, in either an accelerated beam or stationary target nucleus. With the advent of fast radioactive beams, transfer reactions have again come to prominence as an important tool for exploring the exotic regions of the nuclear chart [43, 44, 45]. Single-nucleon transfer reactions (like (p, d), (d, p), and $(d,{}^3\mathrm{He})$) are particularly useful for probing single-particle states, and have been called "the perfect tool for shell structure studies" [46]. The typical procedure is to measure the differential cross section for a specific transfer reaction, and then divide by the calculated differential cross section from reaction theory. The reaction theory (which we discuss in detail in Chapter 2) dictates that the shape of the differential cross section strongly depends on the angular momentum, so the shapes of the measured and calculated cross sections usually match [41]. The SF then comes from the ratio of the magnitude between experiment and theory in the differential cross section.

A more recently developed technique for extracting SFs is the single-nucleon *knockout* reaction, in which a nucleon is removed from an intermediate-energy beam nucleus [44, 47, 48, 49, 50]. Knockout experiments can run with low beam intensity, and therefore can reach further away from the valley of stability than other techniques [51, 44]. This reaction probe is particularly well suited for studying the structure of weakly bound states [47, 48]. In a knockout experiment, the isotope in the beam impinges on a light reaction target. When knockout occurs, the mass $A-1$ recoil is measured and identified in a spectrometer. Gamma ray detectors can then tag on individual final states in the recoil, while longitudinal momentum distributions allow for angular momentum determination [44, 52]. The ratio of the experimental total cross section to the theoretical value then gives the SF.

1.4 Motivation

It stands to reason that if the structure of a given nucleus is invariant, then using different reaction probes to study the same nucleus should yield consistent results. Surprisingly, different techniques do in fact disagree significantly on extracted spectroscopic factors for well-bound nucleons in asymmetric nuclei. Figure 1.5 illustrates this inconsistency by summarizing spectroscopic factor studies performed with several different reaction mechanisms. The y-axis is the reduction factor defined above (relative to LBSM calculations), and the x-axis is defined as $\Delta S = S_n - S_p$ (for neutron removal) or $\Delta S = S_p - S_n$ (for proton removal) where S_n is the neutron separation energy (i.e. the energy cost to remove a neutron from the nucleus) and S_p is the proton separation energy. For neutron-removal reactions, proton-rich nuclei have a very positive ΔS since the neutrons, as the deficient species, are more bound relative to the protons. Removing a neutron from a neutron-rich nucleus has a negative ΔS since the neutrons are relatively less bound. The opposite applies to proton-removal reactions. The plot shows reduction factors extracted via single-nucleon transfer (red), single-nucleon knockout (blue), and electron-induced proton knockout (black). The red, blue, and black points mostly agree for stable nuclei with ΔS close to 0. For removal of weakly bound nucleons, the transfer and knockout both show that reduction factors are at least as high as for stable nuclei (although the trend is more clear from the knockout results). However, in the case of tightly bound nucleon removal, the transfer and knockout show drastically different results. Although both data sets show decreased reduction factors (which indicate the increased influence of correlations), the knockout results show a much stronger decrease than the transfer results. The knockout also shows further reduction for very asymmetric nuclei not currently accessible by transfer reaction studies.

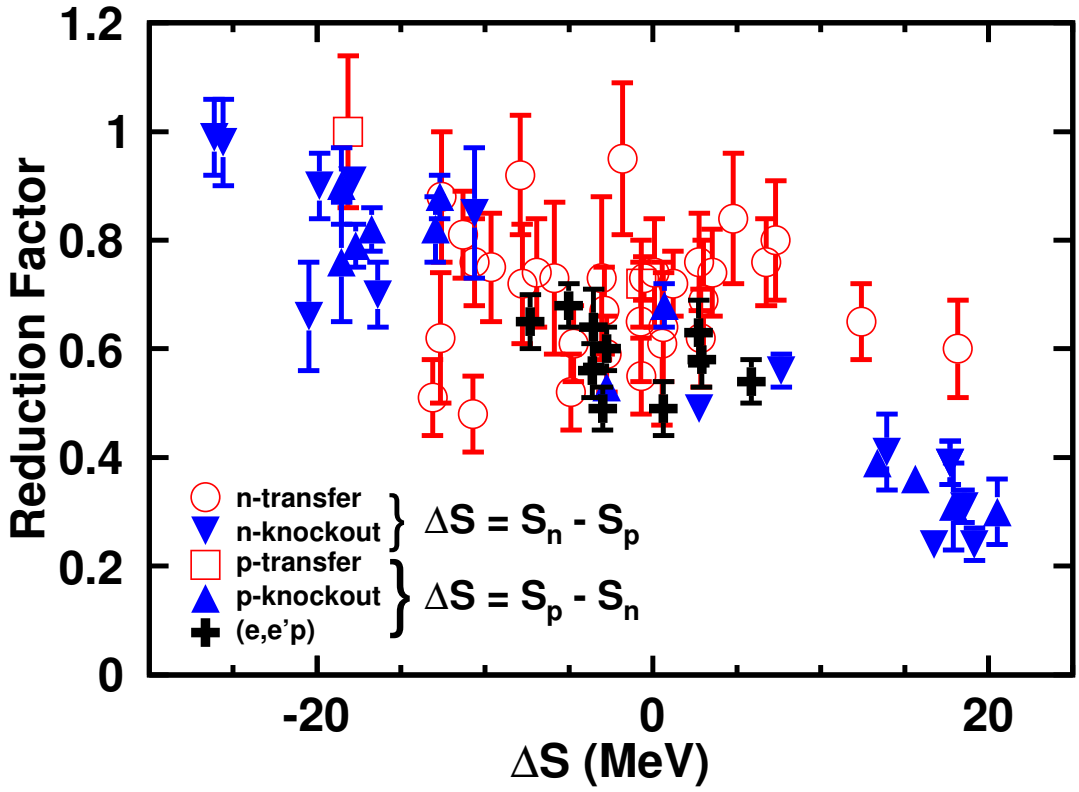

Figure 1.5: Spectroscopic factors extracted from transfer (red), knockout (blue), and electron scattering (black) data for a variety of different isotopes. Data compiled from [26], [52], [53], [54], and references therein.

To more carefully examine this strange phenomenon, we focus on a single isotopic chain. Figure 1.6 shows the transfer-knockout discrepancy clearly for neutron removal from argon isotopes [55, 56]. The reduction factors for single-neutron transfer in red come from [55, 56], and those extracted from single-neutron knockout in blue are from [57, 58, 59]. Again, the red and blue points agree in the case of neutron-rich ^{46}Ar, in which the neutrons being removed are loosely bound. For the proton-rich ^{34}Ar, in which neutrons are tightly bound, the knockout data show a much stronger decrease in reduction factor than the transfer results, and even further reduction for ^{32}Ar (which was not measured with transfer). Note that the ΔS value for ^{34}Ar differs between the transfer and knockout measurements. The transfer measurement was exclusive, so Fig. 1.6 shows the ΔS value calculated with the ground state of the final argon recoil. The knockout measurement, on the other hand, was inclusive, so its ΔS value was calculated with a weighted combination of final states in ^{33}Ar. The knockout reduction factor shown for ^{34}Ar therefore represents an upper limit on the ground state to ground state reduction factor measured by the transfer. This potentially widens the disagreement between transfer and knockout even further. We note that the transfer reactions were measured at a lower beam energy (33 MeV/u) than the knockout reactions (70 MeV/u).

In summary, transfer reactions and knockout reactions produce substantially different results regarding the *neutron-proton asymmetry dependence* of single-particle structure in argon isotopes. The transfer data tells us that the shell model calculations do a reasonably good job of calculating, for instance, the ^{34}Ar single-particle structure (compared to the ^{46}Ar case). On the other hand, the knockout data shows that the same shell model calculations are in fact woefully inadequate, and correlations are playing a stronger role than expected. This discrepancy has also been observed in asymmetric oxygen isotopes [53]. Tostevin and

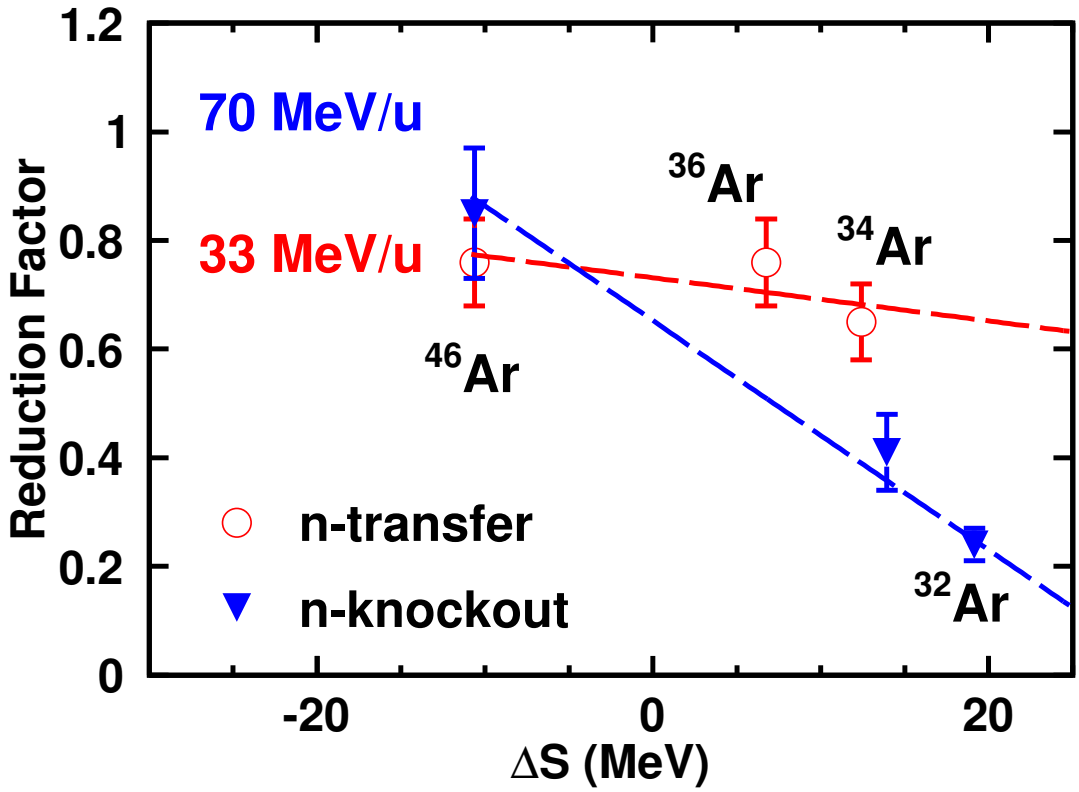

Figure 1.6: Spectroscopic factors extracted from transfer (red) and knockout (blue) data along the argon isotopic chain. Data taken from [55] and [52].

Gade present a summary of knockout results for many different systems that consistently show the same *quenching* of the reduction factor [52]. Some recent knockout studies use the systematic results from Tostevin and Gade to re-normalize SFs in order to compare them to shell model calculations in the sum-rule limit without worrying about suppression due to correlations [60, 61].

This disagreement between transfer and knockout has important consequences. Firstly, the single-particle structure of the neutrons in ^{34}Ar (and other such cases of the deficient species in asymmetric nuclei) is still unresolved. Furthermore, the transfer-knockout discrepancy reveals that at least one of the two reaction mechanisms is not completely understood. This situation is analogous to two astronomers, each with a different type of telescope (optical and x-ray, for instance), looking upon the same star: if they describe the star differently, then perhaps the telescopes themselves are not well understood.

The nuclear physics community has attempted to address this inconsistency between transfer and knockout probes. From a reaction theory perspective, Nunes, et al. suggested that Lee's analysis of the argon transfer measurements was not definitive, and that an alternative treatment of the reaction theory resolves the discrepancy in asymmetry dependence [62]. However other results have since provided further evidence of inconsistency between transfer and knockout SFs [53, 63, 64]. Timofeyuk and others controversially advocate that unresolved problems with nonlocality in the single-nucleon transfer reaction theory make it an unreliable probe for SFs [65, 66]. In general, the large spread in the transfer data (e.g. in Figure 1.5), as opposed to the more clearly defined knockout trend, hints at shortcomings in the reaction theory. There are also theoretical challenges regarding the knockout mechanism. Flavigny et al. have shown that for well-bound nucleons the approximations made in knockout reaction theory break down, resulting in altered cross sections [67]. However, the

tell-tale distorted momentum distributions of the non-sudden effects described by Flavigny are not seen by Gade [57, 58, 59]. Another possibility is that core excitations, typically neglected in knockout analysis, become important when knocking out a deeply bound nucleon [68, 69].

From a structure point of view, the idea that nucleon-nucleon correlations play a more important role for well-bound nucleons in asymmetric systems has some support. Calculations done with the dispersive optical model [70, 71], the self-consistent Green's functions method [72], the inhomogeneous equation [73], and the microscopic coupled-cluster method [74] all indicate an asymmetry-dependence in SF reduction, but (in most cases) weaker than the one observed in the knockout data.

There is also experimental evidence for the *slightly* higher influence of nucleon-nucleon correlations away from stability. For instance, some transfer reaction measurements already discussed ([55, 56]) could indicate a weak asymmetry dependence. In addition, recent results from $(p, 2p)$ quasi-elastic proton scattering experiments on oxygen isotopes show a similar asymmetry trend as the transfer reaction results [75, 76]. These results are plotted in Figure 1.7 in comparison with relevant transfer and knockout data. Quasi-elastic proton scattering is an entirely different reaction mechanism from single-nucleon transfer: the fact that these two probes agree with each other provides strong support for this weaker asymmetry dependence. Finally, electron scattering results in stable nuclei suggest that short-range correlations more strongly affect the deficient species in asymmetric nuclei, but how much this effect manifests in exotic nuclei is unclear [19]. To be clear, however, there is so far no experimental evidence for *strong* asymmetry dependence outside of the single-nucleon knockout results.

Despite productive steps forward in understanding this problem, it remains unresolved. Nuclear structure theorists are working to further understand the role correlations play in

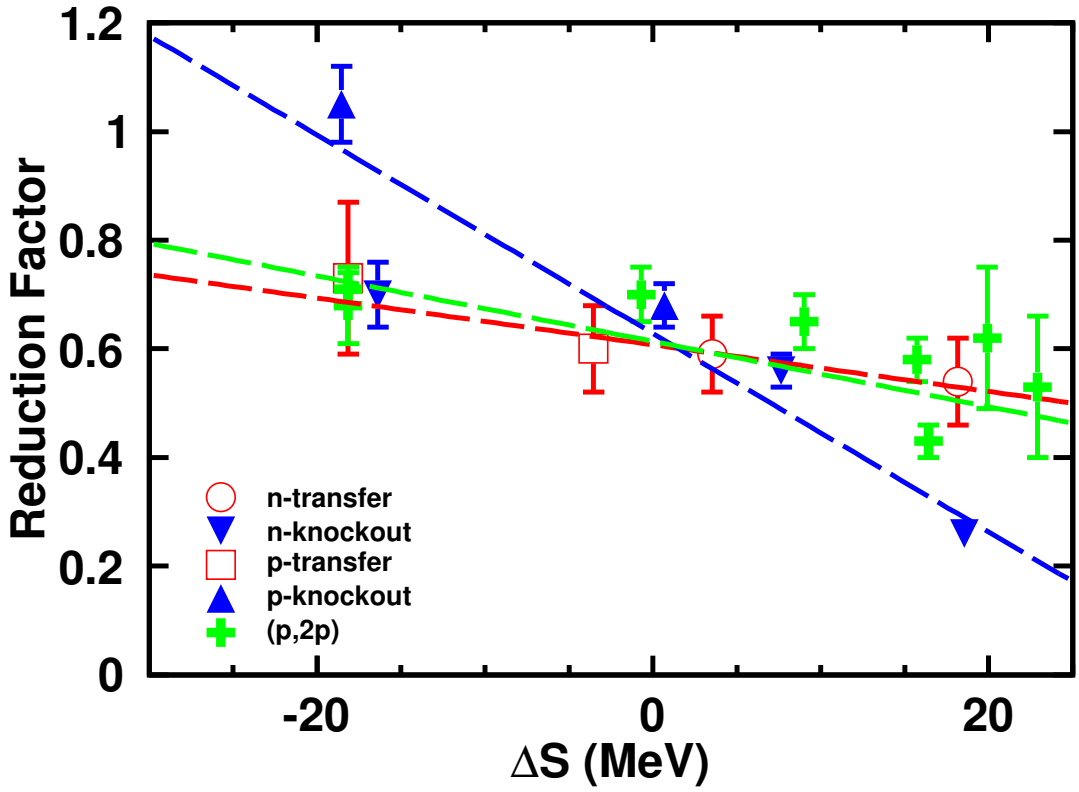

Figure 1.7: Spectroscopic factors extracted with transfer (red), knockout (blue) and quasi-elastic proton scattering (magenta) reactions for the oxygen isotopic chain, along with corresponding trend lines.

their models, while nuclear reaction theorists continue to study sources of uncertainty in SF extraction. On the experimental side, we must gather more data while varying asymmetry, mass number, and other variables to test the validity of both the transfer and knockout reaction mechanisms. One possible variable to explore is the beam energy.

Single-nucleon knockout measurements are performed with intermediate-to-high beam energy (70 MeV/u for the argon knockout data) to ensure the applicability of the eikonal approximation, whereas transfer reactions are usually measured at lower energy (33 MeV/u for the argon transfer data) where the cross sections are higher. Comparing these two mechanisms at the same energy could provide important evidence either for or against the validity of the transfer reaction probe. In this dissertation we present (p, d) transfer reaction measurements (on ^{46}Ar and ^{34}Ar) similar to those performed by Lee except with a beam energy of 70 MeV/u to match Gade's knockout measurement. If this higher energy transfer measurement agrees with Lee's results at low energy, then it bolsters confidence in the consistency of the transfer reaction method at high energies for well-bound nucleons. If the two transfer measurements disagree, then there could be a problem with the current understanding of the single-nucleon transfer mechanism.

1.5 Dissertation Outline

In this dissertation we present (p, d) transfer reaction measurements on two different argon isotopes, as well as the subsequent SF extraction. Chapter 2 introduces the relevant transfer reaction theory and the methodology for extracting SFs from measured differential cross sections. Chapter 3 details the experimental setup at the NSCL, with particular emphasis on the three main radiation detector systems: the High Resolution Array (HiRA), the S800

Spectrograph, and the Microchannel Plates (MCPs). In Chapter 4, we discuss calibration and analysis procedures for each individual detector system. Then, in Chapter 5, we combine data from these separate detectors, and further analyze them to produce differential cross sections for the transfer reactions of interest. We then present the SF extraction from the measured cross sections using transfer reaction calculations, in addition to the corresponding reduction factors and asymmetry trend. We summarize this work and provide concluding thoughts in Chapter 6.

Chapter 2

Reaction Theory

I do not like it and I'm sorry I had anything to do with it.

Erwin Schrödinger, on quantum mechanics

Spectroscopic factors are not observable, and therefore must be extracted from experimental data via comparison to reaction theory. This chapter motivates the basic mathematical framework for calculating transfer reaction differential cross sections, along with the relevant assumptions and commonly used potentials. The methodology used to extract SFs presented in [26] and [36] will be followed.

2.1 Theoretical Framework

In the initial system of a nuclear reaction, an incoming nucleus (referred to as the projectile, or the beam) moves towards a stationary target nucleus. Some sort of interaction between the beam and the target occurs, resulting in a new system of reaction products. In a *transfer reaction*, a nucleon or group of nucleons is transferred between the projectile and the target. The primary concern of this thesis is a type of transfer reaction called neutron-pickup, in which a neutron is transferred from the heavy target to the light proton beam[1]. For

[1]The distinction between beam and target is entirely dependent on reference frame. The reaction model is motivated here assuming a proton beam, but in the experimental setup the proton acted as the target (see Chapter 3).

a neutron-pickup reaction on an argon isotope with mass number A, the reaction can be expressed as

$$^{A}\mathrm{Ar} + p \;\rightarrow\; ^{A-1}\mathrm{Ar} + d$$

and can also be represented in the more convenient notation $^{A}\mathrm{Ar}(p,d)^{A-1}\mathrm{Ar}$.

The observable of interest is a *differential cross section*, given by $\frac{d\sigma}{d\Omega}(\theta,\phi)$, which quantifies the likelihood that a particle will be detected coming out of the reaction system at the solid angle element $d\Omega$ with angles θ and ϕ relative to the incoming beam axis. Due to azimuthal symmetry, only θ dependence is considered here. The general idea is to measure a differential cross section experimentally, calculate the differential cross section for the same transfer reaction using a theoretical reaction model, and compare the experimental and theoretical differential cross sections to extract the SF.

Calculating the differential cross section requires the appropriate mathematical infrastructure. We will first develop this framework in the context of two-body scattering: although this is a simpler problem than the transfer reaction of interest, understanding it will be useful in the subsequent description of transfer reaction formalism.

2.1.1 Scattering Theory

As previously mentioned, a fundamental principle of quantum mechanics is that particles have wave-like properties, and in particular that a physical system can be described using a *wave function*. This wave function is a complex-valued probability amplitude for properties of the system like position and momentum. The Schrödinger equation describes the behavior

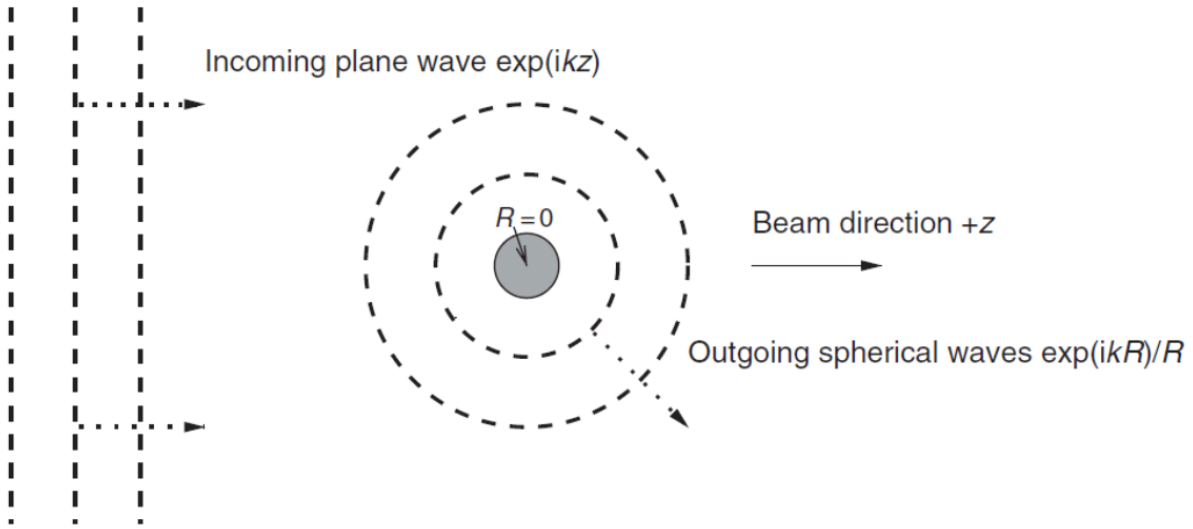

Figure 2.1: An incoming plane wave interacts with a potential to produce outgoing spherical waves. Figure from [77].

of a wave function:

$$\left[\hat{T} + V\right]\Psi = E\Psi$$
$$\hat{T} = -\frac{\hbar^2}{2\mu}\boldsymbol{\nabla}^2$$

where $\hat{T}$ is the kinetic energy operator, V is the potential energy, and Ψ is the wave function. In the definition of $\hat{T}$, $\hbar$ is the reduced Planck constant, μ is the reduced mass of the system, and the Laplacian operator is $\boldsymbol{\nabla}^2$. E is the discrete energy value corresponding to the state given by Ψ.

A schematic of the scattering problem is shown in Figure 2.1: the incoming projectile plane wave packet approaches the target along the z-axis, and after the interaction, an outgoing spherical wave emerges (along the radius R). Asymptotically, the wave function can be written as

$$\Psi^{\text{asym}}(R,\theta) = e^{ikz} + f(\theta)\frac{e^{ikR}}{R} \tag{2.1}$$

where k is the wavenumber and $f(\theta)$ is the *scattering amplitude*, which is the probability amplitude of the scattered wave at angle θ relative to the incident beam. Via consideration of the incoming and outgoing flux (e.g. in [78]), it can be shown that the differential cross section is the square of this amplitude, meaning that

$$\frac{d\sigma}{d\Omega}(\theta) = |f(\theta)|^2 \tag{2.2}$$

The boundary conditions of scattering are such that at infinite distance, the beam and the target do not interact ($V \approx 0$). So, the wave-function Ψ is given by the *free* wave function ϕ where $[E - \hat{T}]\phi = 0$. As the beam approaches the target, the wave function changes due to the influence of V. The naive solution to the Schrödinger equation that satisfies these boundary conditions is given by the *Lippmann-Schwinger equation*:

$$\Psi = \phi + \hat{G}_0^+ V \Psi \tag{2.3}$$

where $\hat{G}_0^+$ is the Green's function operator given by

$$\hat{G}_0^+ = \frac{1}{E - T + i\epsilon} \tag{2.4}$$

We use the fact that the free solution ϕ can be given by a plane wave (which we choose to be in the z direction), and then take the position representation of the Lippmann-Schwinger Equation to get

$$\begin{aligned} \Psi(\vec{R}) = \left\langle \vec{R} \middle| \Psi \right\rangle &= e^{ikz} + \left\langle \vec{R} \middle| \hat{G}_0^+ V \Psi \right\rangle \\ &= e^{ikz} + \int d\vec{R}' G_0^+(\vec{R}, \vec{R}') V(\vec{R}') \Psi(\vec{R}') \end{aligned} \tag{2.5}$$

Using contour integration (e.g. in [79]), we can find the following expression for the Green's function:

$$G_0^+(\vec{R},\vec{R}') = -\frac{\mu}{2\pi\hbar^2}\frac{e^{ik\left|\vec{R}-\vec{R}'\right|}}{\left|\vec{R}-\vec{R}'\right|} \tag{2.6}$$

Now we plug in Equation 2.6 into Equation 2.5 to get

$$\Psi(\vec{R}) = e^{ikz} - \frac{\mu}{2\pi\hbar^2}\int d\vec{R}'\frac{e^{ik\left|\vec{R}-\vec{R}'\right|}}{\left|\vec{R}-\vec{R}'\right|}V(\vec{R}')\Psi(\vec{R}') \tag{2.7}$$

We are concerned with the asymptotic behavior of this wave function, so we let $R = \left|\vec{R}\right|$ go to infinity to evaluate $\left|\vec{R}-\vec{R}'\right|$ by ignoring R'^2 terms and then applying the binomial approximation:

$$\begin{aligned}\lim_{R\to\infty}\left|\vec{R}-\vec{R}'\right| &= \sqrt{(\vec{R}-\vec{R}')^2} = \sqrt{R^2+R'^2-2\vec{R}\cdot\vec{R}'} = R\sqrt{1-\frac{(2\vec{R}-\vec{R}')}{R^2}} \\ &\approx R\sqrt{1-2\frac{\hat{R}\cdot\vec{R}'}{R}} \approx R\left(1-\frac{\hat{R}\cdot\vec{R}'}{R}\right) = R-\hat{R}\cdot\vec{R}'\end{aligned} \tag{2.8}$$

Similarly, we can also neglect $\vec{R}'$ in the denominator of the Green's function expression. Plugging into Equation 2.7 yields

$$\lim_{R\to\infty}\Psi(\vec{R}) = e^{ikz} - \frac{\mu}{2\pi\hbar^2}\frac{e^{ikR}}{R}\int d\vec{R}'e^{-ik\hat{R}\cdot\vec{R}'}V(\vec{R}')\Psi(\vec{R}') \tag{2.9}$$

By comparing Equation 2.9 to Equation 2.1, we can see that the scattering amplitude $f(\theta)$ can be related to the potential V via

$$f(\theta) \propto \int d\vec{R}'e^{-ik\hat{R}\cdot\vec{R}'}V(\vec{R}')\Psi(\vec{R}') = \langle\phi^*|V|\Psi\rangle \tag{2.10}$$

For convenience, we can define the quantity on the right of Equation 2.10 as the *transition matrix (T-matrix)*

$$\mathbf{T} = -\frac{2\mu}{\hbar^2 k} \langle \phi^* | V | \Psi \rangle \tag{2.11}$$

where ϕ^* denotes the complex conjugate of the plane wave ϕ. Using the T-matrix and scattering amplitude, we now have a way to directly calculate the differential cross-section for a given potential V.

2.1.2 The Distorted Wave Born Approximation

Let V be given by two separate components so that $V = U_1 + U_2$, where U_1 is larger. Then consider separately the *full* case with $V = U_1 + U_2$, the free field case with no potential at all, and the *distorted* case with the potential given by only U_1. The associated Schrödinger equations and wave functions are given by

$$\begin{aligned} [E - \hat{T}]\phi &= 0 \\ [E - \hat{T} - U_1]\chi &= 0 \\ [E - \hat{T} - U_1 - U_2]\Psi &= 0 \end{aligned}$$

As discussed above, with no potential the wave function is simply given by ϕ. The Lippmann-Schwinger equations for the distorted and full case, respectively, are

$$\begin{aligned} \chi &= \phi + \hat{G}_0^+ U_1 \chi \\ \Psi &= \phi + \hat{G}_0^+ (U_1 + U_2)\Psi \end{aligned} \tag{2.12}$$

We would like to derive a T-matrix expression to understand the difference between U_1 scattering and $U_1 + U_2$ scattering. Plugging in $U_1 + U_2$ to Equation 2.11 gives $\mathbf{T}^{(1+2)} =$

$-\frac{2\mu}{\hbar^2 k}\int[\phi(U_1+U_2)\Psi]dR$, from which follows

$$\begin{aligned}
-\frac{\hbar^2 k}{2\mu}\mathbf{T}^{(1+2)} &= \int\Big[\chi(U_1+U_2)\Psi - (\hat{G}_0^+ U_1\chi)(U_1+U_2)\Psi\Big]dR \\
&= \int\Big[\phi U_1\chi + \chi U_2\Psi\Big]dR \\
&= \langle\phi^*|U_1|\chi\rangle + \langle\chi^*|U_2|\Psi\rangle
\end{aligned} \tag{2.13}$$

which we can equivalently write as the two-potential formula:

$$\mathbf{T}^{(1+2)} = \mathbf{T}^{(1)} + \mathbf{T}^{2(1)} \tag{2.14}$$

where $\mathbf{T}^{2(1)} = -\frac{2\mu}{\hbar^2 k}\langle\chi^*|U_2|\Psi\rangle$ refers to the T-matrix contribution from U_2 coupling with U_1. Equation 2.14 shows that to calculate scattering due to U_1+U_2, one can calculate the effect of the dominant potential U_1 and then the effect of U_2 on top of U_1 (which shows up via the distorted wave-function χ in $\mathbf{T}^{2(1)}$). We can rewrite the Lippmann-Schwinger equation for the full U_1+U_2 case to reflect this:

$$\Psi = \chi + \hat{G}_1^+ U_2\Psi \tag{2.15}$$

where $\hat{G}_1^+ = [E - T - U_1 + i\epsilon]^{-1}$.

Since Ψ is on both sides of Equation 2.15, we can iterate this implicit equation to yield a *Born series* that converges for a weak enough U_2:

$$\Psi = \chi + \hat{G}_1^+ U_2[\chi + \hat{G}_1^+ U_2[\chi + \hat{G}_1^+ U_2[\ldots]]] \tag{2.16}$$

Now, we can plug Eq. 2.16 into Eq. 2.14 and truncate after the first term, resulting in the

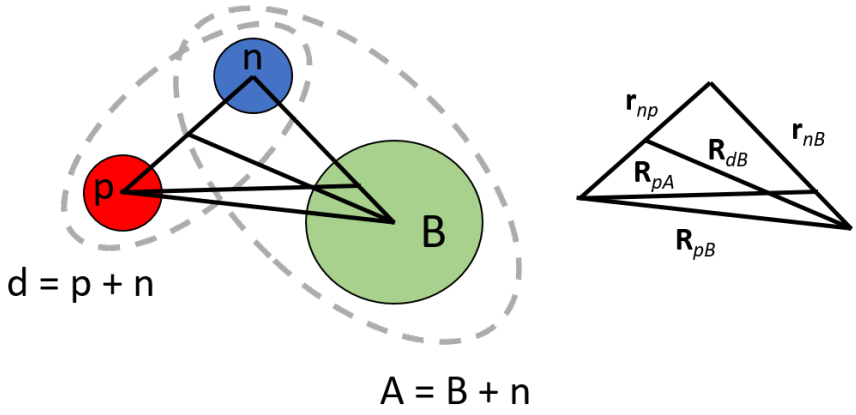

Figure 2.2: Coordinates for a single-neutron transfer reaction. Based on Figure 4.3 in [77].

distorted-wave Born approximation (DWBA) given by

$$\mathbf{T}^{\mathrm{DWBA}} = \mathbf{T}^{(1)} - \frac{2\mu}{\hbar^2 k} \langle \chi^* | U_2 | \chi \rangle \tag{2.17}$$

The DWBA treats U_2 as a perturbation on U_1. In the case of elastic scattering, U_1 is the long-range Coulomb interaction and U_2 is a short-range nuclear interaction. Equation 2.17 is linear in U_2, which can be interpreted as corresponding to a single reaction "step," and is therefore called the *first-order* DWBA. Some reactions call for two or more steps, in which case more terms from Equation 2.16 are included in the truncation.

The above considerations on elastic scattering can be generalized to the three-body transfer reaction system. Figure 2.2 shows the three-body system of interest for the reaction $A(p,d)B$: a proton (p), a neutron (n), and a nucleus B, treated as a structure-less core. A consists of the neutron in a bound state with B. We can write the Hamiltonian using coordinates (defined in Fig. 2.2) chosen to represent the three-body system either before

(the prior form) or after (post) the transfer occurs:

$$\begin{aligned} H = H_{\text{prior}} &= T_{\mathbf{R}_{pA}} + U_i(\mathbf{R}_{pA}) + H_A(\mathbf{r}_{nB}) + \mathcal{V}_i \\ &= H_{\text{post}} = T_{\mathbf{R}_{dB}} + U_f(\mathbf{R}_{dB}) + H_d(\mathbf{r}_{np}) + \mathcal{V}_f \end{aligned} \tag{2.18}$$

where $T_{\mathbf{R}_{pA},\mathbf{R}_{dB}}$ are kinetic energies, $U_{i,f}$ are the entrance and exit channel potentials, $H_{A,d}$ are the internal Hamiltonians of A and the deuteron, and $\mathcal{V}_{i,f}$ are the interaction terms given by

$$\begin{aligned} \mathcal{V}_i &= V_{np}(\mathbf{r}_{np}) + U_{pB}(\mathbf{R}_{pB}) - U_i(\mathbf{R}_{pA}) \\ \mathcal{V}_f &= V_A(\mathbf{r}_{nB}) + U_{pB}(\mathbf{R}_{pB}) - U_f(\mathbf{R}_{dB}) \end{aligned} \tag{2.19}$$

The post and prior forms provide equivalent descriptions of the three-body system, so for convenience we choose to work in the prior form. This has the advantage that in the interaction term $\mathcal{V}_i$, the optical potential between p and A is most likely very similar to the optical potential between p and B, and therefore $U_{pB}(\mathbf{R}_{pB}) - U_i(\mathbf{R}_{pA}) \approx 0$ (for all but light targets). Therefore the interaction term is simply given by the relatively well-known neutron-proton interaction term $V_{np}(\mathbf{r}_{np})$.

Equation 2.17 can apply to transfer reactions with a few minor modifications. First, the distorting potential U_1 is typically chosen to be a spherical potential that describes the elastic scattering between projectile and target. Since no angular momentum is exchanged, this potential cannot induce a nucleon transfer. This means that the T-matrix contribution due to U_1 ($\mathbf{T}^{(1)}$ in Equation 2.17) is 0, simplifying the DWBA expression. Secondly, the outgoing reaction products of a transfer reaction are by definition different from the incoming reactants. The entrance and exit channels are characterized by particular combinations of

mass and quantum numbers. We express the T-matrix from an entrance channel α to an exit channel β by

$$\mathbf{T}_{\alpha\beta}^{\mathrm{DWBA}} = -\frac{2\mu}{\hbar^2 k} \left\langle \chi_\alpha^* \phi_p \phi_A \middle| V_{np} \middle| \phi_d \phi_B \chi_\beta \right\rangle \tag{2.20}$$

where ϕ are the internal wave functions of the incoming and outgoing particles for the $A(p,d)B$ reaction.

2.1.3 The Adiabatic Distorted Wave Approximation

The DWBA framework as described above assumes that the outgoing deuteron from a (p,d) reaction remains intact as it travels away from the target. In reality, the breakup energy of the deuteron is quite low (2.224 MeV), so it will break apart easily in the field of the target nucleus. This clearly has a substantial effect on the measured reaction cross-section. Johnson and Soper modified the DWBA in order to take deuteron breakup into account [80] by making the *Adiabatic Distorted Wave Approximation (ADWA)*: the internal motion of the neutron and proton in the deuteron is slow compared to the motion of the deuteron center of mass. Therefore, the full three-body wavefunction for the $n + p +$ target system is only needed within the small range of the neutron-proton interaction V_{np}. In the limit of a zero-range potential, the interaction between the deuteron and the target can be simply modeled as a combination of target-nucleon interactions, where the nucleons equally share the deuteron energy between them. The deuteron adiabatic potential is defined by

$$U_d(\vec{R}) = \frac{1}{D_0} \int \left\{ U_n(\vec{R} + \frac{1}{2}\vec{r}) + U_p(\vec{R} - \frac{1}{2}\vec{r}) \right\} V_{np}(\vec{r}) \phi_d(\vec{r}) d\vec{r} \tag{2.21}$$

where U_n and U_p are the neutron and proton optical potentials at half the deuteron energy [81], V_{np} is the neutron-proton interaction potential, ϕ_d is the deuteron wave function, $\vec{R}$ is the coordinate of the deuteron center of mass, and $\vec{r}$ is the relative coordinate between the neutron and the proton [80]. D_0 is the strength of the neutron-proton interaction. In addition to the explicit treatment of deuteron breakup, another advantage to ADWA is that it uses nucleon optical potentials, which are typically better constrained experimentally than deuteron optical potentials (see Section 2.1.6 for further discussion of optical potentials).

This approximation is valid as long as the deuteron energy is much larger than the binding energy of the deuteron. The finite-range ADWA has been benchmarked against the exact (and more difficult to solve) three-body Faddeev calculations for simple systems, and is within 10% agreement [82].

2.1.4 Local Energy Approximation

We have assumed, so far, that the neutron-proton interaction is zero-range. Given that the real neutron-proton interaction has a finite range, using the zero-range potential risks overestimating the transfer contribution from the interior of the nucleus. For a small finite-range, we can apply a first-order correction to the zero-range strength called the *local energy approximation* (LEA) [83]. The LEA instructs us to simply replace the zero-range strength D_0 with an effective zero-range strength $D = (1 + k_b^2\beta^2)D_0$, where k_b is the deuteron wave number and β is a parameter that defines the finite-range effective radius.

2.1.5 Nonlocality

All potentials discussed so far have depended only on the distance in between the two interacting particles. Reality is far messier. A potential is considered *nonlocal* if it depends on the value of the potential and scattering wave function at all points in space. Nonlocality can play a significant role in transfer reactions, due to momentum dependence and reaction channels coupling to other degrees of freedom. Exact three-body calculations for light systems show that nonlocality sometimes (but not always) significantly affects the differential cross section [84].

There are two angles by which to approach the problem of nonlocality. One can either explicitly calculate the nonlocal potential (which is difficult), or adjust a local potential in order to effectively approximate the behavior of the fully nonlocal one (which is much easier). Historically, the latter approach has been more common.

For example, Perey and Buck [85] modeled nonlocality with a simple Gaussian adjustment to the local potential, where the Gaussian parameters are fit to experimental data. Since the Perey-Buck approach is easy to implement, it is a common method of including nonlocality in transfer calculations. Of particular importance to this work is that Lee et al. used Perey-Buck in calculating ADWA (p, d) cross sections on argon isotopes at 33 MeV/u [26, 55, 56]. More recent ADWA studies by the University of Surrey group suggest calculating the local nucleon potentials with large and positive energy shifts (around 40 MeV) from the standard prescription of using half the deuteron energy [65, 66]. This shift is meant to take into account the large relative kinetic energy between the neutron and proton induced by their short-range interaction in the deuteron while still using well-known local potentials. A follow-up study suggested also including the deuteron D-wave, increasing the average energy

shift to 70 MeV [86, 87].

In light of the popularity of these simplified methods for treating nonlocality, some have taken a more rigorous approach to identify potential problems. Several studies have pointed out that cross sections calculated with Perey-Buck can differ substantially from those calculated with more explicitly nonlocal theoretical models by 20% or more [88, 89, 90, 91, 92]. Another recent paper shows that Perey-Buck requires nontrivial energy dependence to accurately describe elastic scattering across a wide energy range [93]. The more contemporary energy shift method of Timofeyuk and Johnson has also faced criticism. When compared to the explicit nonlocal formalism, the energy shift method does not reliably improve (quantitatively or qualitatively) the pure local calculation [90].

This is a fascinating and active area of research. Since in reality these many-body systems are inherently nonlocal, much of the theoretical work thus far has justifiably focused on probing the details of the underlying physics rather than developing a widely-applicable experimental tool. At this point, there is no settled upon solution for how to include nonlocal effects into single-nucleon transfer reactions, and the importance of nonlocality (as well as how to properly account for it) varies from system to system. Deeper investigation into the effects of nonlocality on the specific argon isotopes that we focus on here is beyond the scope of this thesis. So, for the purpose of comparison to the low-energy transfer work of [55, 56], we will use the standard Perey-Buck nonlocality.

2.1.6 Optical Potentials

Above, we outlined how to calculate the differential cross-section using quantities that depend primarily on the potentials. As such, the choice for which potentials to use can have a significant impact on the calculated cross section. The real, many-body potentials are ex-

tremely complicated and beyond the reach of current theoretical tools: the nucleon-nucleus *optical potential* reduces this difficulty to scattering of a single particle on a complex one-body potential. Optical potentials use effective imaginary components to remove flux due to reactions not included in the model, analogous to the imaginary potentials used to account for absorption as light passes through a cloudy medium.

Ideally, an optical potential for a given nucleus-nucleus interaction can be fit directly to elastic scattering data for that particular system and beam energy. Unfortunately such data does not typically exist for rare isotope beams. Below, we describe global optical models and microscopic optical models, the two most common approaches in the face of this obstacle.

2.1.6.1 Global Optical Potentials

A *global* optical model is a parameterized, simultaneous fit across many angular distributions for a wide range of target nuclei with a given projectile. This global model can then be used to interpolate (or even extrapolate) to the case of interest. The nucleon-nucleus global optical potential is given by

$$\begin{aligned} U(r) = -V_r f_{\rm ws}(r, R_V, a_V) - iW_r f_{\rm ws}(r, R_W, a_W) + 4iW_s a_w \frac{d}{dr} f_{\rm ws}(r, R_W, a_W) \\ +2(V_{so} + iW_{so})\left(\frac{1}{r}\frac{d}{dr} f_{\rm ws}(r, R_{so}, a_{so}) L \cdot \sigma\right) + V_C \end{aligned} \tag{2.22}$$

where $f_{\rm ws}$ is the Woods-Saxon potential given by $f_{\rm ws}(r, R, a) = \left[1 + e^{\frac{r-R}{a}}\right]^{-1}$. V and W refer to real and imaginary potentials, respectively. Potentials due to the interior volume (given by subscript r) as well as the exterior surface (s) are both included, as well as a spin-orbit potential (so) and a Coulomb term (c) that treats the nucleus as a homogenous sphere of charge. R is the nuclear radius parameter and a indicates the diffuseness of the

nuclear surface. L is the orbital angular momentum of the projectile relative to the target, and σ is the spin operator.

The global potential used in this work is the Chapel-Hill 89 (CH89) potential developed by Varner, et al. [94]. CH89 is fit to nearly 300 proton and neutron differential cross sections with $A = 40 - 209$ and $E = 10 - 65$ MeV, and has been shown to describe single-nucleon transfer data better than other global models on the market [95, 26].

2.1.6.2 Microscopic Optical Potentials

In a *microscopic* optical model, nucleon density distributions (known from electron scattering experiments or nuclear structure calculations) are folded together via a convolution integral to generate the optical potential. As opposed to the global optical model approach in which data from a wide range of nuclei is fit, a microscopic optical model leverages nuclear structure theory to generate a potential specific to a single nucleus given a particular nucleon-nucleon interaction. Suppose a structureless projectile (e.g. a proton) is approaching a target with many nucleons. If we know the interaction potential between the projectile and individual nucleons in the target, we can estimate the overall potential via the following convolution integral:

$$U(\mathbf{r}) = \int d\mathbf{r_t} V_{pN}(\mathbf{r} - \mathbf{r_t}) \rho_t(\mathbf{r_t}) \tag{2.23}$$

where $\mathbf{r}$ is the position of the projectile relative to the target, $\mathbf{r_t}$ is the internal position coordinate over the target, V_{pN} is the potential between the projectile and each nucleon of the target, and ρ_t is the target density.

The microscopic potential used in this work was developed by Jeukenne, Lejeune, and Mahaux (JLM) [96, 97]. The JLM model uses Reid's hard core nucleon-nucleon interaction

[98] in the many-body framework of the Brueckner-Hartree-Fock approximation. Reasonable agreement between theoretical and empirical cross-sections [97, 99, 100, 101, 102] shows that the JLM is valid for $A = 12 - 208$ and energies up to 160 MeV.

As shown in Equation 2.23, nucleon densities are required as input to calculate the JLM potential. In this case, these densities are taken from Hartree-Fock calculations with the SkX parameter set [103] that accounts for a wide range of experimental observables [104, 105, 106]. When using the JLM potential, we adjust the radius parameter r_0 to reproduce the mean squared radius of the transferred neutron orbital obtained via Hartree-Fock calculation [39].

2.1.6.3 Optical Potential Uncertainty

Earlier in this chapter, the theoretical differential cross section was connected directly to the interactions in the three-body system. Different potentials, therefore, yield different cross sections. This is problematic given that in most cases the relevant potentials are not directly constrained to data from the system of interest, and are instead obtained from a phenomenological fit (CH89) or from a microscopic calculation using nuclear densities (JLM). In other words, there is ample room for theoretical error. As an example, Figure 2.3 shows the differential cross section for a transfer reaction calculated with CH89 (black) and JLM (red). Although the shapes of the calculations match, the magnitude of the JLM cross section is slightly higher due to larger neutron bound-state wave functions [26, 95, 39]. More recent work on uncertainty quantification suggests that theoretical uncertainties due to the optical potential are often underestimated [107]. The validity of the ADWA for transfer reactions at high energies has even been called into question in the past [108, 109]. How can meaningful physics information be extracted using transfer reactions with so much

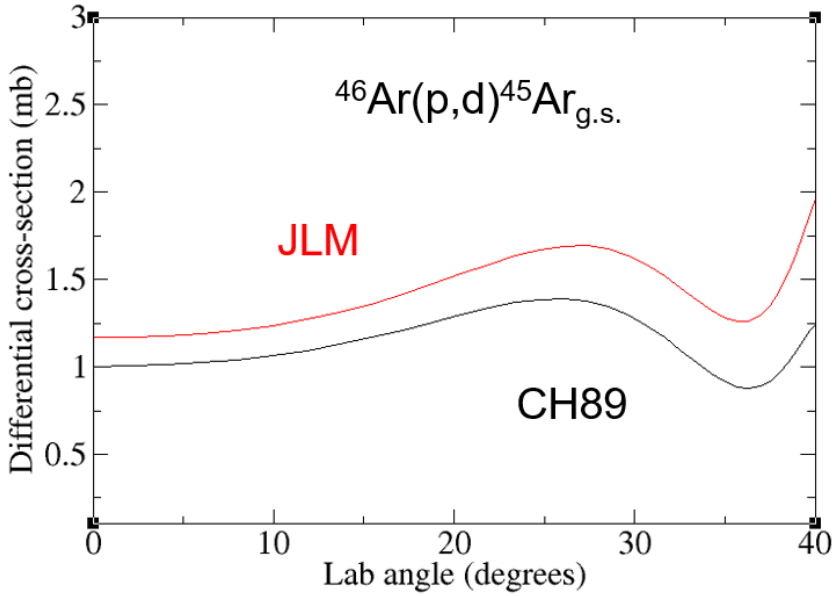

Figure 2.3: Differential cross section calculations for $^{46}\mathrm{Ar}(p,d)^{45}\mathrm{Ar}_{\mathrm{g.s.}}$ with CH89 (black) and JLM (red) optical potentials.

theoretical ambiguity?

Lee, Tsang, and Lynch directly addressed this problem by studying a wide range of differential cross sections and extracting spectroscopic factors using a single systematic approach [36, 26, 38, 39]. For a given individual cross section or spectroscopic factor, one can expect the theoretical error to be quite large. However, within a consistent framework, the relative *trends* across a range of isotopes can provide insight that is often independent of the choice in optical potential. This point is exemplified in Figure 2.4, which shows (in red) the reduction factors of the previous argon transfer study calculated with both the CH89 and JLM potentials. The reduction factors differ in magnitude, but the trend shown by the CH89 reduction factors is the same as for the JLM: both choices of optical potential show substantial disagreement with the knockout reaction results (in blue), and so in this sense the large error bars for a specific SF are not of crucial importance.

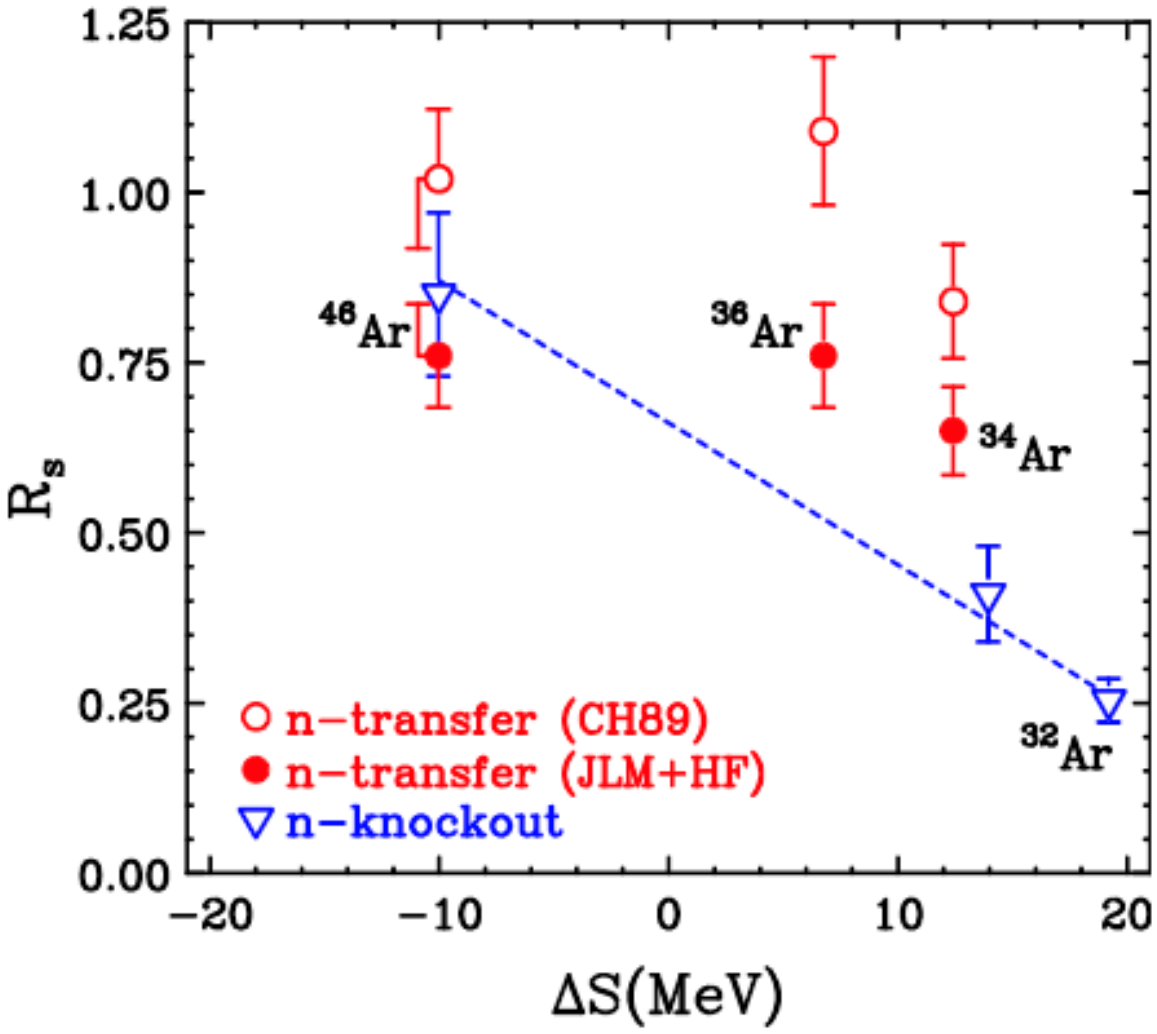

Figure 2.4: Spectroscopic factors extracted from transfer (red) and knockout (blue) data along the argon isotopic chain. SFs extracted with two different optical models are shown: the JLM (solid) and the CH89 (open). Data taken from [55] and [52].

2.2 Methodology

To extract spectroscopic factors, we will measure the differential cross section of (p, d) transfer reactions in inverse kinematics, and then compare this experimental data with the theoretically calculated cross section. The ratio of the experimental cross section to the theoretical cross section gives the spectroscopic factor.

The T-matrix amplitude expressed in Equation 2.20 can be expressed in terms of spectroscopic factors. First, the matrix element $\left\langle \phi_\alpha \middle| V_{np} \middle| \phi_\beta \right\rangle$ can be expanded using the nuclear overlap integral that defines the SF:

$$\langle \phi_A | \phi_B \rangle = \sum_{nljm} \langle J_A j M_A m | J_B M_B \rangle \sqrt{S_{nlj}} \Phi_{nljm} \tag{2.24}$$

where $\langle J_A j M_A m | J_B M_B \rangle$ is a Clebsch-Gordan coefficient, S_{nlj} is the spectroscopic factor (SF), and Φ_{nljm} is the single-particle bound-state wave function for the $A = B + n$ system. Rearranging the integration variables and plugging Equation 2.24 into Equation 2.20 yields

$$\mathbf{T}_{\alpha\beta}^{\mathrm{DWBA}} \propto \sum_{nljm} \sqrt{S_{nlj}} \left\langle \chi_\alpha^* \Phi_{nljm} \middle| \left\langle \phi_p \middle| V_{np} \middle| \phi_n \right\rangle \middle| \phi_\beta \chi_\beta \right\rangle \tag{2.25}$$

Since the square of transition amplitude given by the T-matrix is proportional to the differential cross section (as shown in Equations 2.10 and 2.11), Equation 2.25 gives us a direct connection between SF and differential cross section. For a theoretical cross section, the SF is typically assigned to its maximum value (1 or $2j + 1$ depending on normalization). Therefore, the ratio of the experimentally measured cross section to the theoretical cross section will equal the ratio of the experimental SF to the maximal SF. The shape of the cross section is dominated by the angular momentum exchanged (which is known), so we

can have confidence that the shape of the theoretical cross section will match the shape of the data.

2.2.1 The TWOFNR Reaction Code

Our approach follows the one prescribed by Lee, which is described in detail in [26]. The (p, d) reaction calculations in this work were performed with the University of Surrey version of TWOFNR, a direct reaction code for calculating DWBA with finite-range [110].

All calculations were performed using the finite-range ADWA described by Johnson and Soper [80] using as input experimentally determined angular momenta and reaction Q-values. Calculations were carried out over 30 fm integration ranges with 0.1 fm steps and 70 partial waves. The bound-state wave function potential was a Woods-Saxon shape, in which the depths of the central potential wells were adjusted to reproduce experimentally determined Q-values. For the CH89 calculations, we used typical values for the radius (1.25 fm) and diffuseness (0.65 fm) parameters. For the JLM calculations, we followed the procedure described in [39] to tune the radius parameter in order to reproduce the mean-squared radius of the neutron orbital. In every case, we use the local energy approximation (with $\beta = 0.7457$ fm) to account for finite-range effects in the neutron-proton interaction. The Reid soft-core ${}^3S_1 - {}^3D_1$ neutron-proton interaction was chosen with the zero-range strength $D_0^2 = 15006.25$ MeV^2 fm^3 and the range $\beta = 0.7457$ fm. Nonlocality corrections for both the proton and deuteron channels were included, with ranges of 0.85 fm and 0.54 fm, respectively.

In this chapter we developed the theoretical machinery needed to extract spectroscopic factors from transfer reaction data. Next, we will discuss the transfer reaction experiment itself.

Chapter 3

Experimental Methods

One must imagine Sisyphus happy.

Albert Camus

Measurements of the transfer reactions ^{46}Ar$(p,d)^{45}$Ar and ^{34}Ar$(p,d)^{33}$Ar were performed with a beam energy of 70 MeV/u at the National Superconducting Cyclotron Laboratory (NSCL) at Michigan State University. This chapter discusses the experimental methods used in this measurement. Section 3.1 describes the method of measurement and motivation for the experimental design. Section 3.2 discusses the production of the rare isotope beams used for this experiment. Sections 3.3, 3.4, and 3.5 include descriptions of the High Resolution Array (HiRA), the S800 Spectrograph, and the Micro-Channel Plate Detectors (MCPs), respectively. In Section 3.6, we discuss the precise position characterization of the setup.

3.1 Experimental Design

Transfer reactions have been a crucial tool to study nuclear structure for many decades. In the 1950s, a typical transfer measurement consisted of an accelerated beam of light particles (usually an isotope of hydrogen) impinging upon a fixed "target" composed of stable, heavy isotopes [42]. These normal kinematic measurements require that the target isotope have a relatively long half-life and that it can be easily produced in large quantities. Exotic isotopes satisfy neither of these two criteria, and so we cannot study them using normal kinematics.

Therefore, contemporary transfer reaction measurements are done in *inverse kinematics* in which the roles are reversed: an accelerated beam of heavy (usually radioactive) nuclei impinges upon a much lighter target. In the center-of-mass frame of the system, inverse kinematics is equivalent to the traditional normal kinematics. Inverse kinematics not only opens up large swaths of the nuclear chart for study with transfer reactions, but also ensures that all fragments originating from the incoming beam escape the target, due to their high momenta.

Since the argon isotopes of interest in this work are unstable, we measured the transfer reactions $^{46}\mathrm{Ar}(p,d)^{45}\mathrm{Ar}$ and $^{34}\mathrm{Ar}(p,d)^{33}\mathrm{Ar}$ in inverse kinematics. The radioactive, 70 MeV/u argon beams were produced at the Coupled Cyclotron Facility (CCF) at the NSCL as described in Section 3.2. This beam energy was chosen to match that of the corresponding knockout measurement (see [59] and Chapter 1). For each reaction, a $(\mathrm{CH_2})_n$ polyethylene target provided the proton. Although this plastic target is not purely composed of protons, the background from reactions on carbon is low and in fact can be measured (and then subtracted) using a pure carbon target. Furthermore, polyethylene can be obtained easily at a wide range of thicknesses and with good uniformity, in stark contrast to the considerable technical challenges involved in using a liquid or gaseous pure hydrogen target.

Figure 3.1 shows a schematic of the experimental setup. The observable of interest in this experiment is the differential cross section of the transfer reaction from which a spectroscopic factor can be extracted, as discussed in Chapter 2. Measuring a cross section corresponding to a particular reaction requires knowledge of both the outgoing flux from that reaction (i.e. the number of times that reaction occurs) as well as the incoming flux into the target (i.e. the number of incoming beam particles). The former quantity we measure using the High Resolution Array (HiRA) for detecting the outgoing deuterons and the S800 Spectrograph for

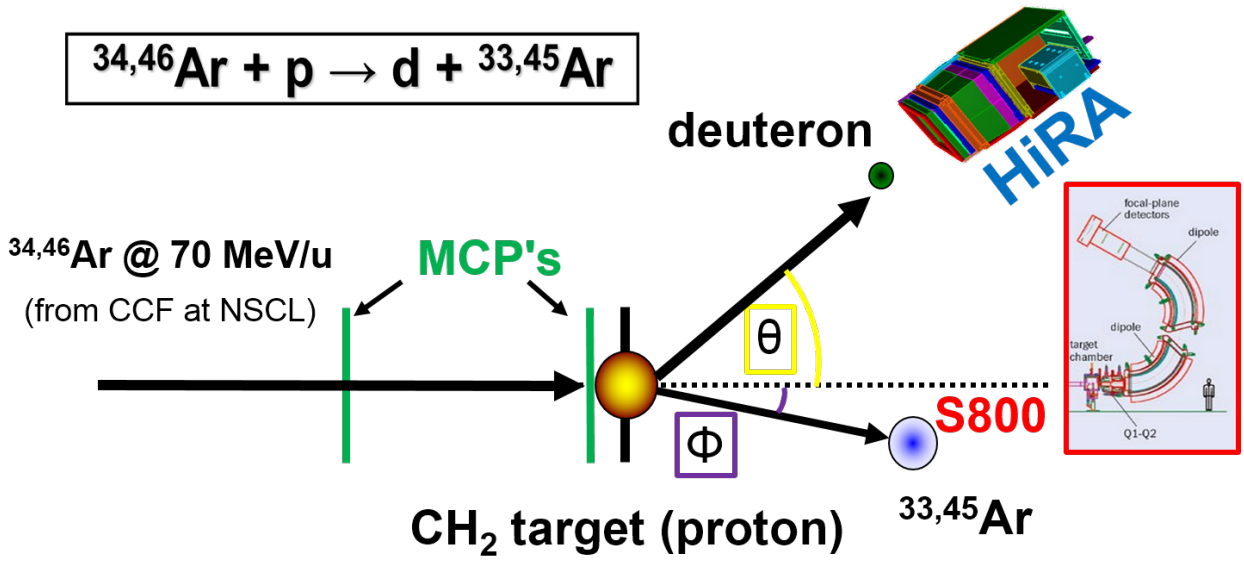

Figure 3.1: Cartoon of the experimental setup. The incoming beam (either ^{34}Ar or ^{46}Ar) was produced with the Coupled Cyclotron Facility (CCF) at the NSCL. A polyethylene target was inserted into the beamline to measure (p, d) reactions on the incoming beam. Upstream of the target, two Microchannel Plates (MCPs) were placed to normalize the cross-section and also track the beam position on target. The outgoing heavy recoil from the transfer reaction (either ^{33}Ar or ^{45}Ar) was detected and identified in the S800 Spectrograph. The outgoing deuteron was detected and identified with the High Resolution Array (HiRA).

detecting the outgoing heavy argon recoils in coincidence. The latter quantity we determine using Micro-Channel Plate detectors (MCPs), which measure the incoming beam particles before they impinge upon the target. The MCPs also enable event-by-event beam tracking, which provides a valuable boost to the angular resolution of the emitted particles detected in HiRA. The MCPs and HiRA sat with the reaction target in a vacuum chamber at the entrance of the S800. A gap was left in HiRA at very forward angles to allow the heavy recoil and unreacted beam to pass through the array into the S800. Since both the deuteron as well as the appropriate heavy recoil must be detected to reconstruct the transfer reaction of interest, the key trigger condition of the data acquisition was a coincidence between HiRA and the S800.

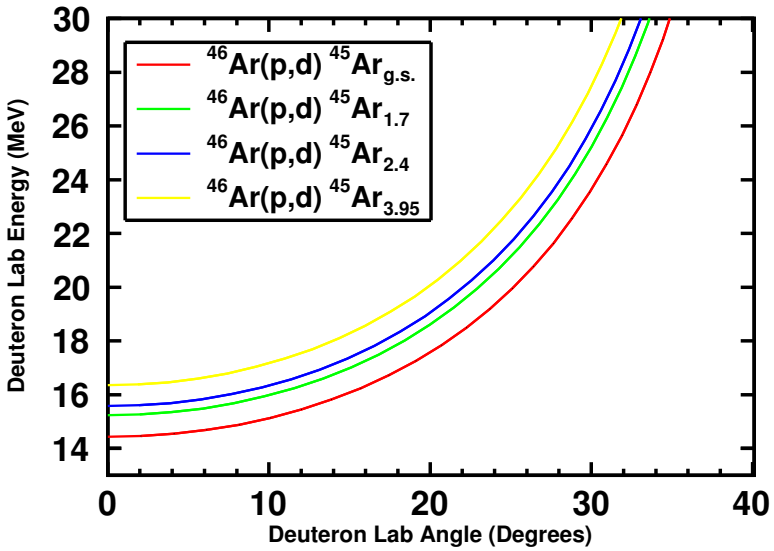

Figure 3.2: Kinematic curves for $^{46}\mathrm{Ar}(p,d)^{45}\mathrm{Ar}$ for different excitation energies of the outgoing recoil ^{45}Ar. This energy-angle relationship of the emitted deuteron can be measured with HiRA.

Due to the straightforward two-body kinematics of the outgoing transfer reaction products, the energy and angle of the deuteron uniquely determine the final state in the ^{45}Ar recoil. For example, Figure 3.2 shows the calculated relationship between deuteron energy and angle for $^{46}\mathrm{Ar}(p,d)$ transfer into different states of ^{45}Ar. Clearly, different final states of the heavy recoil can be distinguished by measuring the emitted deuteron. By transforming the deuteron energy from the laboratory frame to the center-of-mass frame, we can calculate the excitation energy spectrum for the Ar recoil. We then use the number of counts in each peak for a given angular range to calculate a differential cross section for a transfer reaction into the corresponding state in the argon recoil.

Nuclear physics experiments like this one often feature multiple detectors and a high quantity of data being generated from each of those detectors every second. Therefore, a well-designed *data acquisition system* (DAQ) is critical in order to properly coordinate and record the data. The vast majority of this data is uninteresting, so ideally the DAQ will

recognize in real-time what data is important, and what data is not worth recording. The *trigger condition* determines when the DAQ does or does not record data. In this experiment, the most crucial ingredient of the trigger was a coincidence between HiRA and the S800, as discussed above, while the MCPs ran as slaves (i.e. signals from the MCPs would be recorded when the trigger condition was satisfied). An electronic pulser was included in the trigger to properly track the dead time of the silicon detectors in HiRA (more details are provided in Chapter 5). The DAQ also recorded downscaled counts from the HiRA and MCPs. A CAEN V830 scaler continuously counted logic signals for a variety of electronics circuits. Each of the detector electronics systems fed into the DAQ (written with the NSCLDAQ software suite [111]) that managed and merged the data flows. NSCLDAQ employs a ring buffer structure that allows for fast and flexible data transfer. The SpecTcl C++ framework interfaced with the DAQ allowed for online monitoring of the data in real-time [112].

As described in Chapter 1, the vital information this work seeks to study is the *comparison* between two transfer reactions: ^{46}Ar(p,d) and ^{34}Ar(p,d). Maximizing the validity of this comparison requires making systematic uncertainties for these measurements as similar as possible. Therefore, the most important principle of the experiment design is that it allows each of these two reactions to be studied, one immediately after the other, with an identical setup. The experimental systems detailed below have the necessary flexibility to achieve this goal.

3.2 Beam Production

The NSCL's Coupled Cyclotron Facility (CCF) consists of two superconducting cyclotrons that can accelerate a wide range of stable *primary beams* [113, 114, 115] to semi-relativistic

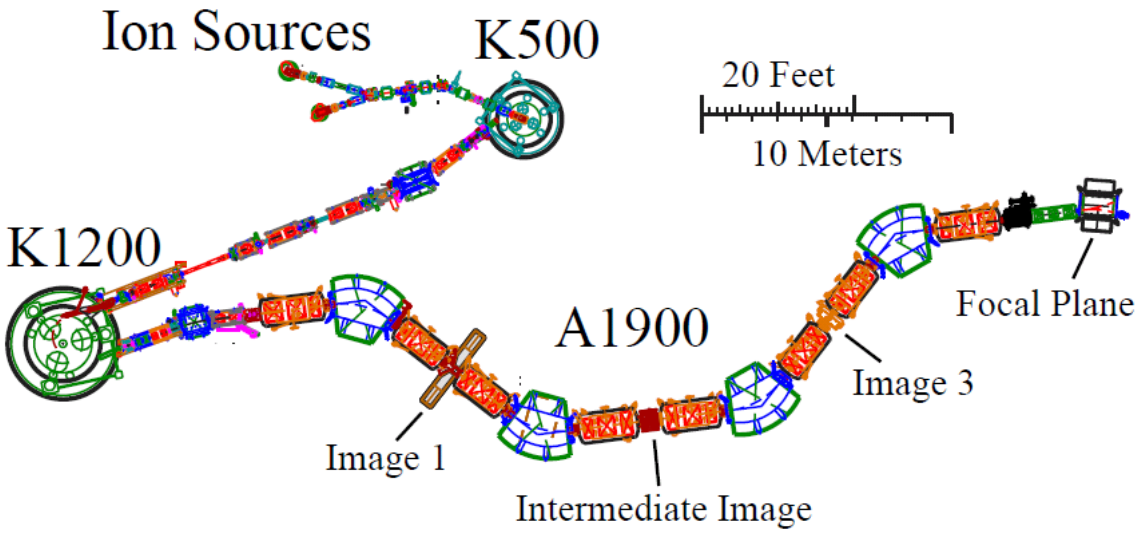

Figure 3.3: Schematic of the Coupled Cyclotron Facility, showing ion sources, the K500 cyclotron, the K1200 cyclotron, and the A1900 fragment separator [117].

speeds up to $0.5c$. The accelerated primary beam then impinges on a beryllium target to produce a variety of stable and unstable isotopes via *fragmentation*. These isotopes then proceed to the A1900 Fragment Separator, where they can be filtered by mass and charge [116]. The resulting *secondary beam* is then delivered to one of many experimental areas for further study. A schematic of the CCF is shown in Figure 3.3.

3.2.1 Primary Beams

Every beam accelerated at the NSCL begins in an *ion source* that removes electrons from stable atoms to provide charged stable ions to the cyclotrons. Ion production relies on the *electron cyclotron resonance (ECR)* phenomenon, in which electrons rotating at cyclotron frequency in a stable magnetic field are heated by co-circulating electric fields. The electrons heat into a plasma, and then collide with atoms to knock out other electrons from their atomic orbitals. Eventually, cycles of collisions produce highly charged ions. These ions can

then be extracted electrostatically. The NSCL has two ion sources: the ARTEMIS ECR source and the SUSI ECR source.

A *cyclotron* uses an oscillating electric field and a static magnetic field to accelerate charged particles. As the name suggests, the CCF features two cyclotrons: the K500 and the K1200. The number in the name of each accelerator simply refers to the theoretical maximum proton energy (in MeV) that each cyclotron can achieve. Particles are first accelerated in the lower-energy K500 cyclotron and then further accelerated in the K1200.

The ions extracted from the ion source are injected into the K500 cyclotron at the center, and begin moving in a circular trajectory due to the magnetic field. A negative electric potential is alternated on the three metal electrodes (referred to as "dees") to increase the kinetic energy of the particles. As the energy increases, the radius of the circular path traced out by the ion increases. Eventually, the accelerated ion reaches the edge of the cyclotron and exits. The ions, now accelerated to an intermediate energy, then pass through a thin carbon foil to strip off more electrons and become more highly charged. To achieve optimum acceleration, the charge-to-mass ratio of the ion must be maximized, and therefore high charge states (full ionization if possible) are ideal. After going through the foil, the ions enter the K1200 cyclotron where they are further accelerated. The K1200 is more powerful than the K500 but operates via the same principles that are described above.

The ions, now referred to collectively as the primary beam, then impinge on a beryllium production target. Although many ions in the beam pass through the target, some collide with beryllium nuclei and undergo fragmentation. A wide range of isotopes are created in this fragmentation process. Most of the isotopes produced then proceed to the A1900 fragment separator for purification.

In this experiment, we used two primary beams. For the first beam, ^{36}Ar ions (with a

7+ charge state) were extracted from the SUSI ion source and then accelerated in the K500 to 13.06 MeV per nucleon. The ions were then stripped fully (to an 18+ charge state) and injected into the K1200 where they were accelerated to 150 MeV per nucleon. For the second beam, ^{48}Ca ions (with an 8+ charge state) were extracted from the ARTEMIS ion source and then accelerated in the K500 to 12.28 MeV per nucleon. As in the case of the first beam, the ions were stripped fully (this time to a 20+ charge state). Then, they were accelerated to 140 MeV per nucleon in the K1200.

3.2.2 Secondary Beams

The fragmentation process produces many different isotopes. However, most experiments require a secondary beam made up of a single isotope. The role of the A1900 fragment separator is to filter away the unreacted primary beam and any unwanted fragments, leaving behind only the nuclei of interest. This isotope selection process is quite powerful, and serves as a vital component to virtually every single experiment at the CCF.

The A1900 (shown in Fig. 3.3) consists of four 45° superconducting dipole magnets and 24 superconducting quadrupole magnets in eight cryostats. Filtration occurs in two stages: in the initial stage, the first two dipole magnets after the production target select particles by dispersing them according to their magnetic rigidity $B\rho$:

$$B\rho = \frac{p}{q} \propto \frac{A}{Z}v \tag{3.1}$$

where p refers to the relativistic momentum of the particle, v is the velocity, q is the charge, B is the magnitude of the magnetic field, and ρ is the bending radius of the dipole. A and Z refer to the mass and atomic numbers of the particle, respectively. Only particles within a

given range of magnetic rigidity (i.e. within a given range of $\frac{A}{Z}$) pass through both dipoles. In the second stage, an aluminum wedge is placed at the Intermediate Image position (see Figure 3.3). The amount of energy loss in a medium by a given particle depends strongly on its charge, so the wedge induces a velocity shift that depends on the Z of the fragment. Following the wedge are another two dipole magnets that again disperse the beam according to $B\rho$. At various points along the separator, slits are used to block out fragments that do not match the set rigidity. The resulting isotope beam (known as the secondary beam) is then transported to an experimental hall.

We used two secondary beams in this experiment. First, the ^{36}Ar primary beam generated a 70 MeV/u ^{34}Ar secondary beam (94% pure). Immediately afterwards, the ^{48}Ca primary beam generated a 70 MeV/u ^{46}Ar secondary beam (more than 99% pure). In both cases, the beam was transported to the reaction target and detector setup in the S3 vault at the NSCL.

3.3 HiRA

The High Resolution Array (HiRA) is a modular array of charged particle detectors developed at Michigan State University in collaboration with Washington University, Indiana University, Southern Illinois University Edwardsville, and the Istituto Nazionale di Fisica Nucleare [118]. HiRA is composed of individual "telescopes," each containing a 65-um, single-sided, 32-strip silicon detector (referred to as the "DE" detector), a 1500-um, double-sided, 32-strip silicon detector (referred to as the "E" detector), and an array of four 3.9-cm-thick CsI scintillator crystals, with each crystal spanning roughly a quadrant of the preceding silicon detectors. Figure 3.4 shows a cartoon with each of these detectors. A thin Mylar foil in front

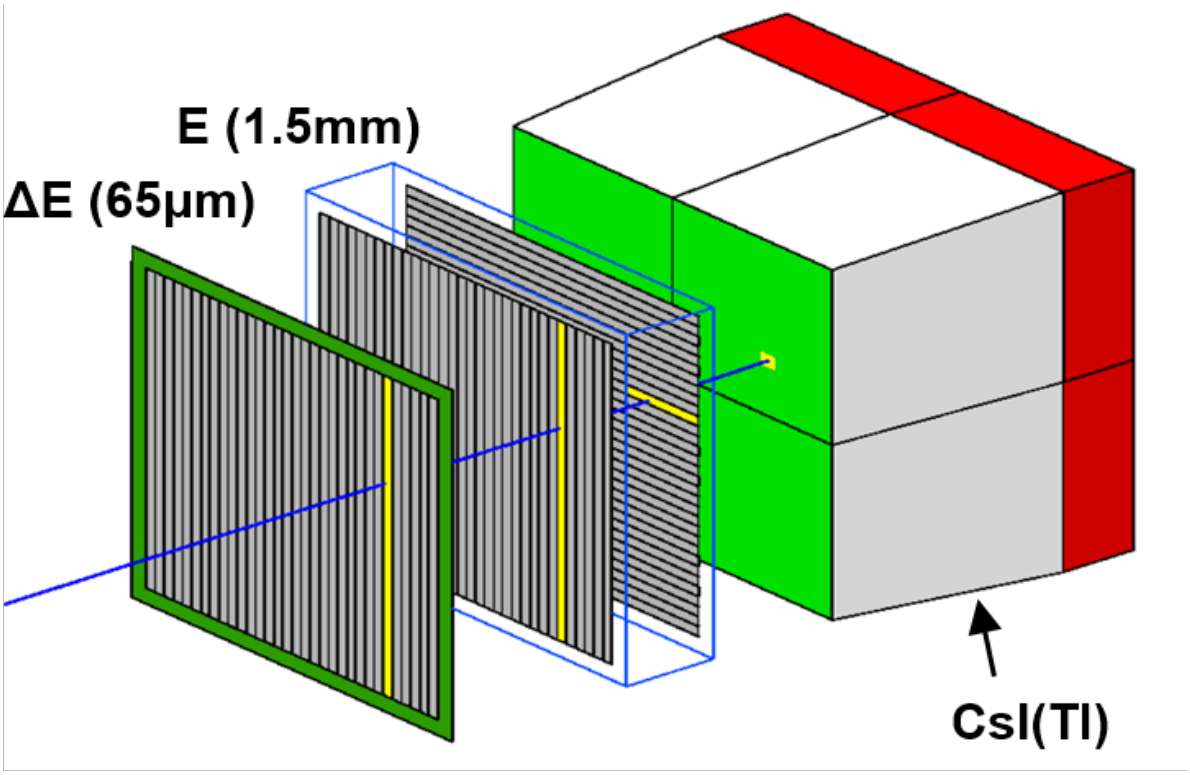

Figure 3.4: Cartoon showing the radiation detectors inside of each HiRA telescope.

of the DE on each telescope completes a Faraday cage around the detectors within, helping to reduce noise. Depending on the needs of a given measurement, HiRA can be arranged in different geometrical configurations. This flexibility enables HiRA to address a wide variety of topics within the realm of nuclear physics, including direct reactions for nuclear structure, nuclear astrophysics, exotic two-proton decay, and the nuclear symmetry energy [119, 120, 121, 122].

HiRA has two key characteristics crucial for measuring the differential cross sections of interest in this experiment: excellent position resolution and unambiguous particle identification.

An accurate and precise measurement of the angle of the emitted deuteron is crucial for properly probing the energy-angle kinematic relationship discussed in Section 3.1. To

achieve the necessary precision, HiRA features the double-sided silicon detector referred to as the E detector. The 32 strips on the front of the E ("EF") and the 32 strips on the back ("EB") are perpendicular to each other. The coincidence between one strip on the EF and one strip on the EB corresponds to a particle going through a 1.95 mm by 1.95 mm "pixel" at the intersection of the two strips. Each pixel corresponds to an angular resolution of ± 0.16 degrees at 35 cm from the target.

To study (p, d) transfer, we need to unambiguously identify light charged-particles. HiRA's crucially important particle identification (PID) feature emerges from the comparison of energies measured in different detectors within a telescope. To show why, we consider the Bethe-Bloch equation which relates the energy deposited by a particle with atomic number Z and mass number A in a given medium to the total energy of the particle E:

$$-\frac{dE}{dx} \propto \frac{Z^2 A}{E} \tag{3.2}$$

Therefore, the ratio of the energy that a charged particle deposits in a "thin" detector to the energy measured in a corresponding "thick" detector (where the charged particle deposits the rest of its energy) allows for unique determination of both Z and A. HiRA provides two separate stages of PID. In one case the DE acts as the "thin" detector which is compared to the "thick" E detector. In the other case, when a particle is energetic enough to pass through the E, the E acts as the "thin" detector with one of the CsI crystals as the corresponding "thick" detector. These two PID stages allow for a relatively large dynamic range of particle identification. For instance, HiRA can properly identify deuterons with energies from ~3 MeV to ~150 MeV.

While some HiRA experiments only require one stage of PID, this transfer reaction

measurement needs both. For the reactions of interest, the kinematic relationship between deuteron energy and emitted angle can be calculated unambiguously via straightforward application of conservation laws. Figure 3.5 shows this relationship for both $^{46}\mathrm{Ar}(p,d)^{45}\mathrm{Ar}_{\mathrm{g.s.}}$ and $^{34}\mathrm{Ar}(p,d)^{33}\mathrm{Ar}_{\mathrm{g.s.}}$ at 70 MeV/u, as well as the punch-through energy[1] for a deuteron in the E detector. Below the green line, deuterons will stop in the E detector and therefore we identify them via the E-DE PID stage, whereas above the green line we use the CsI-E stage. In order to probe a reasonably large angular range for both reactions of interest with the same experimental setup (as discussed in Section 3.1), the kinematic curves show that both stages of PID are necessary.

3.3.1 Silicon Detectors

Each HiRA telescope holds two separate semiconductor detectors made of silicon. The silicon detectors were manufactured by Micron Semiconductor using the design BB7. The active surface area is 6.4 cm $\times$ 6.4 cm, and the thickness is either 1500 μm (E) or 65 μm (DE). The DE detector is subdivided into 32 vertical strips, while the E detector has 32 vertical strips on its front side (EF), and 32 horizontal strips on its back (EB). The pitch of each strip is 1.95 mm for all detectors, with an inter-strip gap of 25 μm for the EF and the DE, and 40 μm for the EB. Figure 3.6 shows an example of an E detector sitting in a partially assembled HiRA telescope. Each telescope features a slot between the DE and the E detectors to allow for insertion of a pin source, a small radioactive metal pin used to calibrate the E detector without having to remove the DE (see Chapter 4 for more detail).

The periodic lattice of a crystalline material generates energy bands along which electrons

[1]The *punch-through energy* of a given detector for a given particle refers to the minimum amount of energy needed for that particle to pass completely through the detector.

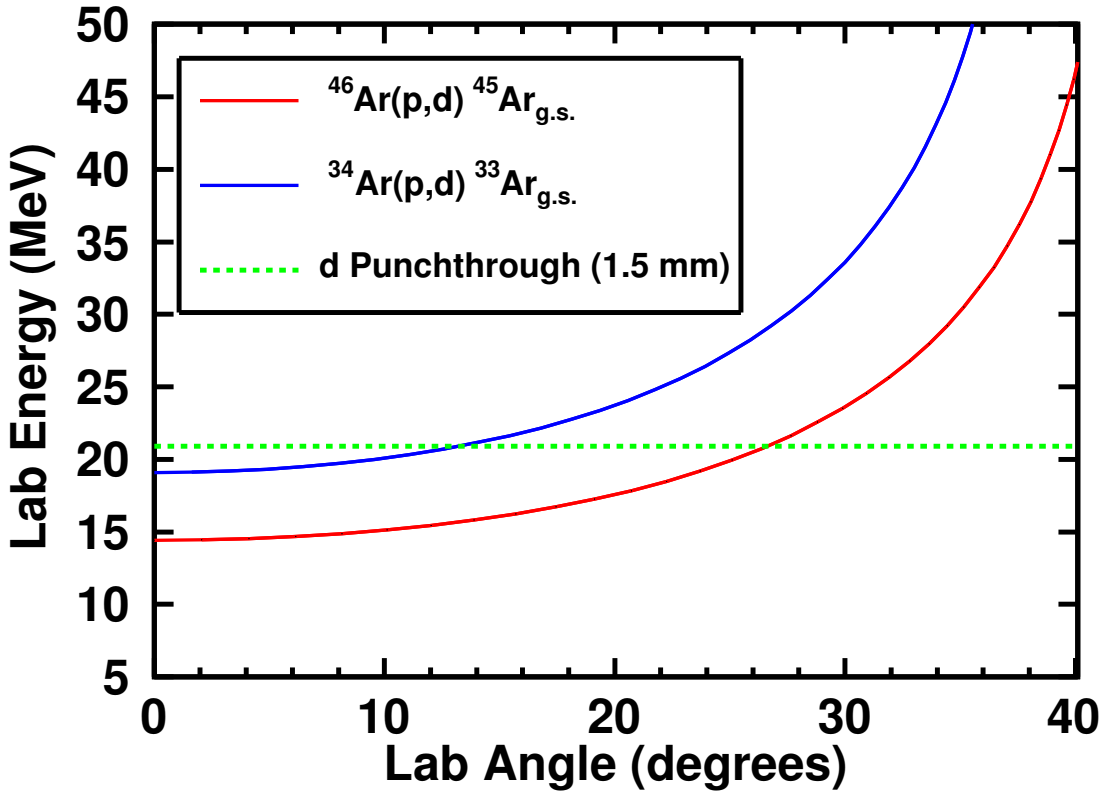

Figure 3.5: Kinematic curves for $^{46}\mathrm{Ar}(p,d)^{45}\mathrm{Ar}_{\mathrm{g.s.}}$ (in red) and $^{34}\mathrm{Ar}(p,d)^{33}\mathrm{Ar}_{\mathrm{g.s.}}$ (in blue) at 70 MeV/u. The green dotted line corresponds to the punch-through energy for a deuteron through the E detector.

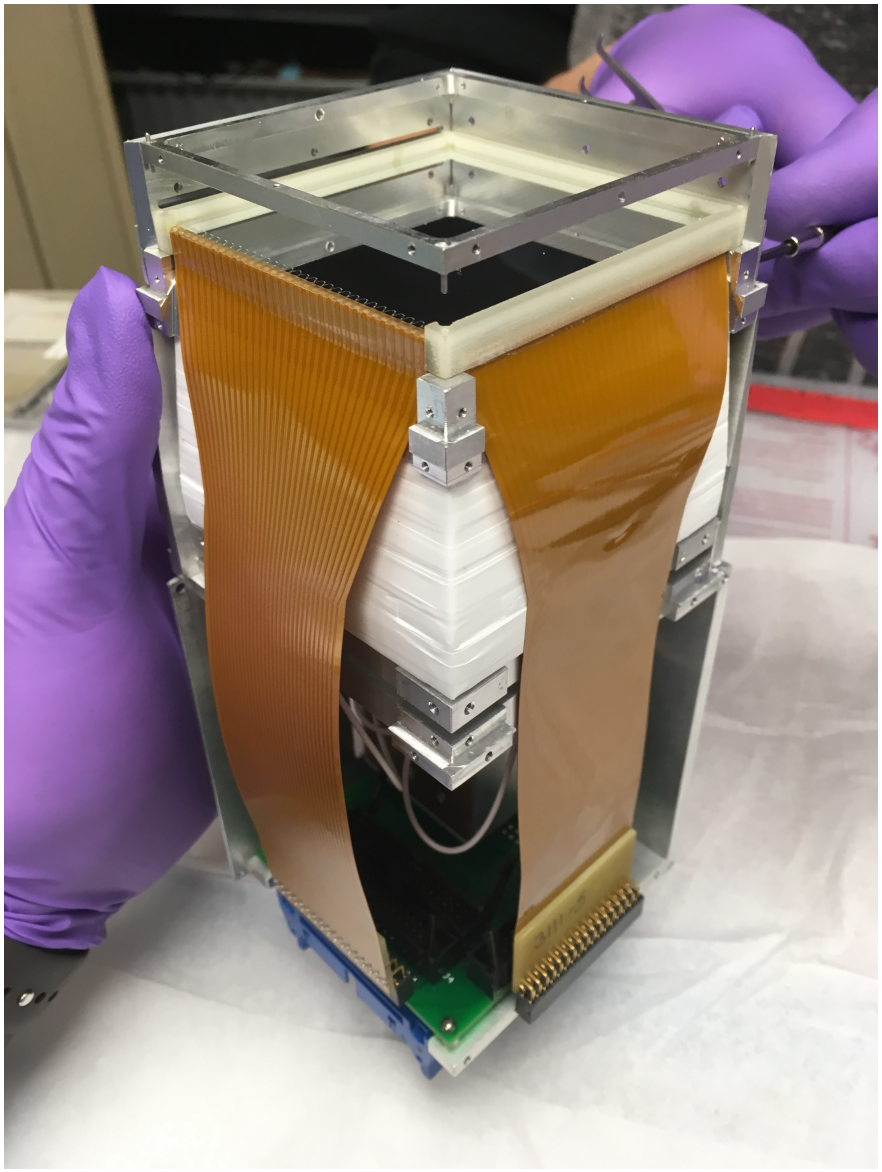

Figure 3.6: Photo of a partially assembled HiRA telescope with an E silicon detector. The front surface of the E detector (EF) is visible at the top of the figure. Wire bonds connect each individual EF strip to the orange cable running down the left side of the telescope. The corresponding cable for the back surface (EB) can be seen on the right. The E detector is held by a G10 fiberglass frame, and this frame is attached with screws to the metal sides of the telescope. A bundle of four CsI scintillators can be seen underneath the silicon detector. The DE detector (not shown) is placed above the E and secured in place by screwing its G10 frame to the telescope.

in the material can travel. The valence band corresponds to outer-shell electrons in the lattice atoms, and the higher energy conduction band corresponds to electrons that can travel freely throughout the lattice. The energy separating these two bands is called the *band gap*: electrical insulators typically have band gaps upwards of 5 eV, while electrical conductors often have no band gap at all (the valence band and conduction band overlap). A *semiconductor*, which has electrical conductivity between that of an insulator and that of a conductor, usually has a band gap of ~1 eV. Using a simple linear relation, the band gap is related to the ionization energy, or the amount of energy needed to generate a single electron-hole pair [123]. In the case of silicon at room temperature the band gap is 1.12 eV and the ionization energy is 3.62 eV [124]. So, if a particle deposits 1 MeV of energy into the detector, then $(1 \times 10^6$ eV/3.62 eV per pair$) \approx 2.8 \times 10^5$ pairs are generated. By applying an electric field across the detector, these pairs can be collected to measure the deposited energy.

The conductivity of a semiconductor can be modified via the introduction of impurities, or *doping*. Doping silicon with impurities from group V of the periodic table results in an *n-type* material that has an excess of electrons. On the other hand, doping with impurities from group III results in a *p-type* material with an excess of holes. Silicon radiation detectors like the ones used in HiRA typically consist of a *p*-*n* junction in which an *n*-type silicon and a *p*-type silicon are grown face-to-face. At this junction, free electrons drift from the *n*-type side to the *p*-type side, creating a region of space charge where charge carriers are depleted. This depletion region can be expanded by applying bias voltage across the junction. When a charged particle deposits energy in a fully depleted *p*-*n* junction, the generated electron-hole pairs are immediately swept towards the surfaces of the detector and collected on metal contacts. Since the number of collected pairs is linear with deposited energy, the detected

current provides a measure of the energy.

In HiRA, the electrical signals from the silicon detectors are processed using the HINP16C application-specific integrated circuit (ASIC) electronics designed at Washington University and Southern Illinois University Edwardsville [125]. Each HINP16C channel, which corresponds to a single strip of silicon, contains charge-sensitive amplifiers, a pseudo constant fraction discriminator, a shaping amplifier, a time-to-voltage converter, and associated digital logic. A single ASIC chip contains 16 individual channels, so one 32-channel detector (EF, EB, or DE) requires two ASIC chips (usually placed together on a single chipboard). These chipboards are then placed onto motherboards (each of which can fit at most 16 chipboards) that communicate with the data acquisition system.

In this experiment, we used 14 telescopes, each with three 32-channel silicon detectors. We placed three motherboards inside the chamber behind the towers of the HiRA array for the EF and EB silicon. Signals from the DEs were pre-amplified externally before being sent to the HINP16C electronics due to high noise associated with the low capacitance of the thin silicon detector. The DE pre-amplifiers sat on top of the vacuum chamber along with another HINP16C motherboard.

3.3.2 CsI Detectors

Each HiRA telescope contains an array of four cesium iodide (CsI) thalium-doped scintillators to detect particles that have enough energy to punch through both layers of silicon. These 3.9-cm-thick CsI crystals can detect deuterons up to 150 MeV in energy. Each crystal has been cut into a trapezoidal shape, with the front surface being 3.5 cm by 3.5 cm and the back 3.9 cm by 3.9 cm [118]. In order to assemble a full array of four packed crystals, the two inner edges of each crystal are cut straight while the two outer edges are cut with a

5.3-degree taper. Each crystal is wrapped in cellulose nitrate membrane filter paper and aluminized Mylar, and also is optically coupled (using BC600 optical cement) to a 1.3-cm light guide. The light guide is painted with BC600 reflective paint. A 1.8-cm-by-1.8-cm photodiode sensitive to the wavelength of light produced in the crystal is attached to the back of each light guide using RTV615 silicon rubber. Figure 3.7 shows drawings of a CsI bundle.

CsI is a scintillator material, meaning that it emits scintillation light when excited by ionizing radiation. When a charged particle hits a CsI crystal, electron-hole pairs are created. The return of an electron to the valence band results in emission of a photon [124]. However, this process is inefficient for the pure CsI crystal, and the photon is too high in energy to fall in the visible range. Impurities (also known as activators) like thalium are added to the lattice to modify the band structure of the crystal by adding in new energy states by which electrons can de-excite sequentially to the valence band. This recombination has higher efficiency than for the pure crystal, and yields visible photons [124]. These photons then impinge on the photodiode, where they induce electron-hole pairs that are measured as current. About 6.5×10^4 photons are created per MeV of deposited energy, which is much less than the number of electron-hole pairs created per MeV in silicon. Having fewer information carriers corresponds to a higher statistical uncertainty for the CsI compared to the silicon, and therefore a worse energy resolution.

Signals from the CsI crystals are amplified via a charge sensitive preamplifier board located at the back of each HiRA telescope. From there, the signals exit the vacuum chamber and are input into CAMAC shaper/discriminator modules (made by Pico Systems). Output from these modules is fed into a CAEN V785 ADC and a CAEN 1190 TDC.

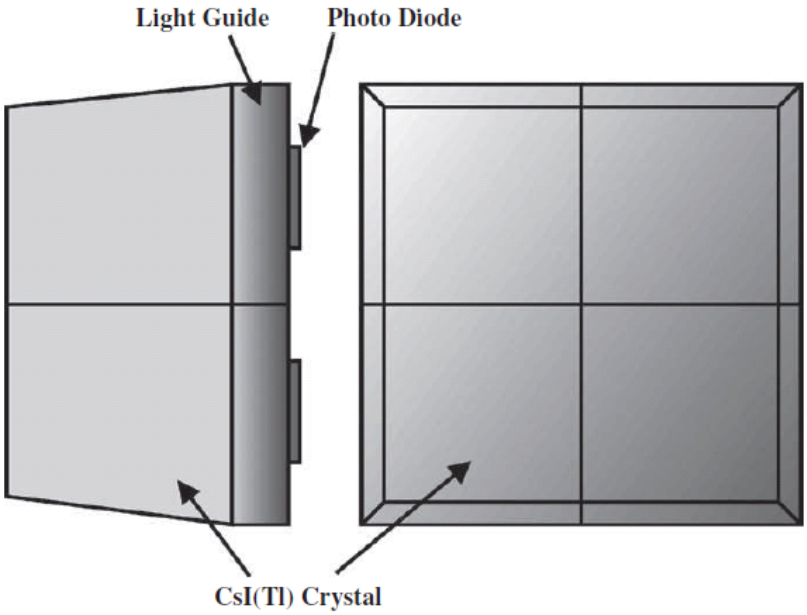

Figure 3.7: Side-view and front-view drawings of a four-crystal CsI scintillator bundle.

3.3.3 Geometry

The geometry for this experiment was based on the one used in experiment 05133. Figure 3.8 shows a picture of HiRA as it was setup for this experiment. Calculations with TWOFNR indicate that detecting deuterons at relatively forward angles, roughly in the range of 8 degrees to 40 degrees in the laboratory frame, is sufficient to properly identify states in the outgoing recoil nucleus. At very forward angles, there is no coverage in order to allow the recoil nucleus ample space to pass through gap between HiRA telescopes to then proceed into the S800.

Understanding the geometrical coverage of HiRA is a critical ingredient in extracting the angular-dependence of the cross-section. In other words, we must know the probability that a deuteron emitted at a given angle will be detected in HiRA. The geometric efficiency of HiRA can be studied using Monte Carlo simulations in order to quantify exactly the fraction of particles emitted at a given angle that hit HiRA.

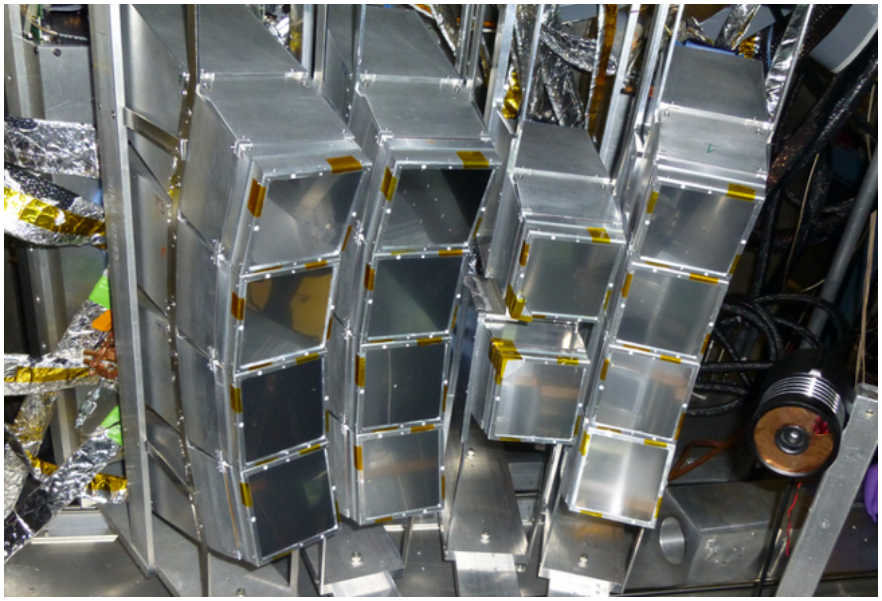

Figure 3.8: Photo of HiRA in the setup for experiment 09084.

We used the program NPTool to calculate the geometric efficiency of the HiRA array. NPTool is a framework that combines the Geant4 simulation code with the ROOT analysis package to simulate arbitrary experimental geometries with a wide array of different detector types [126]. The precise locations of the HiRA telescopes (see Section 3.6 for a description of the measurement) were input into the NPTool calculation, as well as a flat cross section for the (p, d) reactions in the center-of-mass frame in order to focus purely on the experimental geometry. Figure 3.9 shows the calculated geometrical efficiency as it depends on the emitted deuteron angle assuming that all detectors in the array work optimally. However, this assumption is unrealistic. The calculation in Figure 3.9 is shown here to provide the reader with a rough approximation of the angular coverage of HiRA. Chapter 5 will detail a more careful treatment of the efficiency and its dependence on angle.

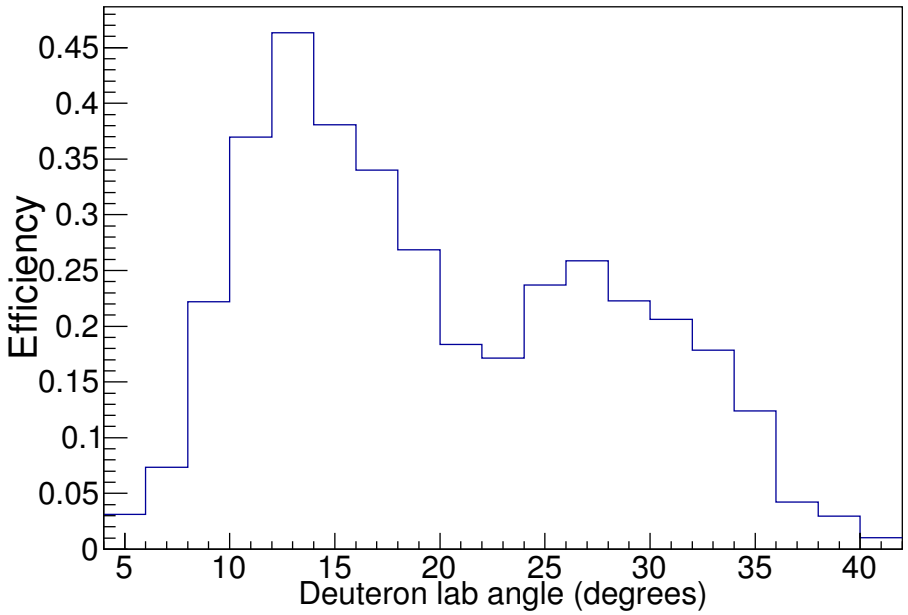

Figure 3.9: Geometrical efficiency versus emitted deuteron angle for HiRA. This efficiency was calculated assuming that all detectors work perfectly. This assumption will be revisited in detail in Chapter 5.

3.4 The S800 Spectrograph

The S800 Spectrograph (or simply, the S800) is a magnetic spectrograph with large acceptance in both solid angle and momentum [127]. In this experiment, we used the S800 to detect and identify heavy recoils from transfer reactions. The S800 (shown in Figure 3.10) consists of a large bore magnetic quadrupole doublet followed by two dipole magnets, which are set at a certain magnetic rigidity to select particles of interest from reactions at the target. Downstream from the dipoles is the focal plane[2] detection system used to measure position, energy loss, and timing information (see Fig. 3.11) [128]. The S800 is preceded by an analysis line composed of four superconducting dipole magnets (outlined in blue in Fig. 3.10) and 5 superconducting magnetic quadrupole triplets (outlined in green). Immediately

[2]The *focal plane* is the plane perpendicular to the S800 optical axis that passes through the focal point of the S800. The focal point is the point of convergence for particles with ideal rigidity that enter the S800 parallel to the optical axis.

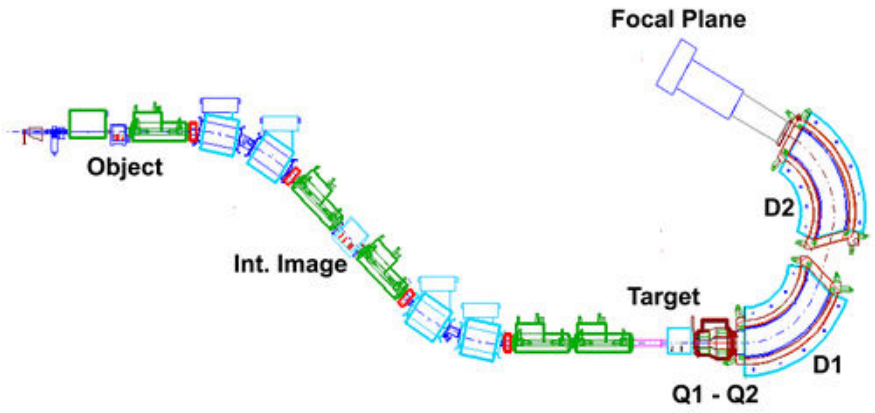

Figure 3.10: The S800 Spectrograph and its associated analysis line.

upstream of the analysis line is a scintillator (known as the object scintillator) that can be used as a start signal in time-of-flight (TOF) measurements.

The S800 can be tuned in either of two possible optical modes. In focused mode the secondary beam is focused on the target position and then dispersed in momentum at the focal plane. In dispersion-matched mode, the S800 and analysis line are tuned to an achromatical focus at the focal plane so that the beam is dispersed in momentum at the target. Focused mode allows for larger momentum acceptance ($\pm 2\%$) but worse energy resolution (1 part in 1000) than dispersion-matched mode ($\pm 0.5\%$ and 1 part in 2000, respectively). For this experiment, we ran the S800 in focused mode in order to maximize momentum acceptance, which allows for a higher momentum spread in the beam and therefore a higher beam intensity. Furthermore, the primary purpose of the S800 was to identify reaction products, and this does not require the excellent momentum resolution of dispersion-matched mode.

Beam-like fragments enter the S800 from the reaction target and are dispersed by the magnetic dipoles. The dipoles are tuned to a particular magnetic rigidity in order to maximize acceptance for a particular isotope (in this case, usually either ^{45}Ar or ^{33}Ar). After passing through the dipoles, the fragments enter the focal plane detector box as shown

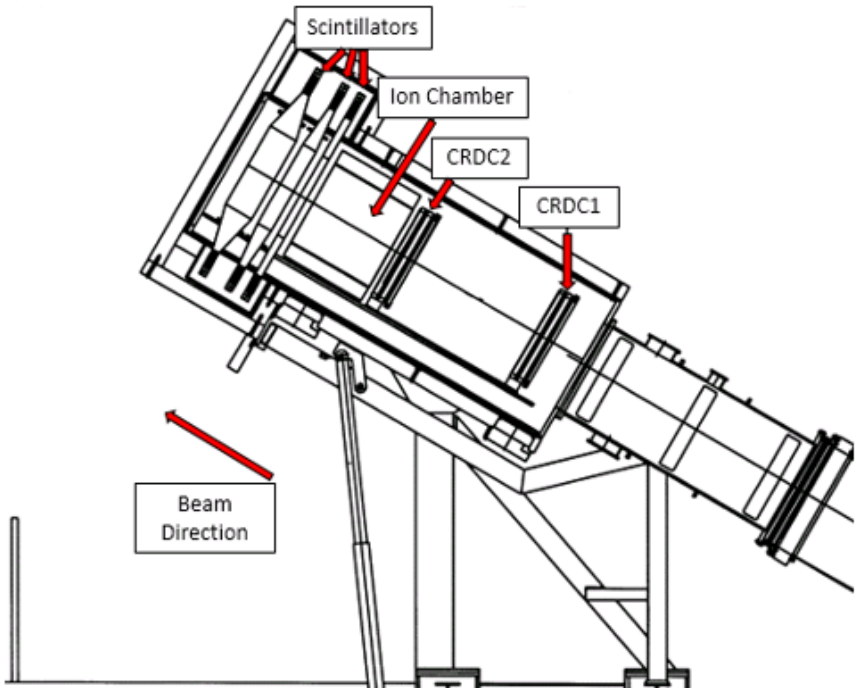

Figure 3.11: The S800 focal plane detector box. Figure adapted from [128].

in Figure 3.11. The detectors in this box include two Cathode Readout Drift Chambers (CRDCs) which track the trajectory of the fragment, one Ionization Chamber (IC) which measures energy loss (ΔE), and a plastic scintillator (known as the E1) used to measure the time-of-flight (TOF) and also to trigger the S800 data acquisition. Scintillators located upstream from the S800 provide timing information to identiy the beam-like fragment before and after a reaction occurs. These scintillators are included in the S800 data acquisition out of convenience. Comparison of TOF and ΔE yields particle identification, provided that the data is sufficiently corrected using focal plane coordinate information from the CRDCs. See Chapter 4 for details of these corrections.

3.4.1 Cathode Readout Drift Chambers (CRDCs)

The CRDCs are two identical gas-filled, single-wire drift detectors, separated by approximately 1 m, that provide position information of the fragment's trajectory as it travels

through the spectrograph towards the focal plane. Each CRDC has an active area of 30 cm $\times$ 59 cm (with a thickness of 1.5 cm) and is filled with a mixture of 80% CF_4 and 20% C_4H_{10} gas. There is a constant electric field in the vertical (non-dispersive) direction across the CRDC, so as a fragment passes through the CRDC and ionizes the gas within, the ionized electrons drift to the anode wire for detection. The drift time of these electrons provides the non-dispersive position of the fragment in the CRDC. The dispersive position comes from 224 cathode pads, each with a pitch of 2.54 mm, that collect image charge induced by the anode current. Position measurements in both of the CRDCs allow for the calculation of angles relative to the central trajectory in both the dispersive and non-dispersive directions.

3.4.2 Ionization Chamber (IC)

The IC measures the energy deposited by a fragment as it travels through the S800 to the focal plane. Located downstream from the CRDCs, the IC is filled with P-10 gas (90% argon and 10% methane) and segmented into 16 1-inch sections. As the fragment passes through the IC, it deposits energy in the gas by producing ion-electron pairs, and the number of such pairs created is proportional to the energy deposited. Therefore, detection of these pairs allows for a direct measure of the energy lost by the fragment.

3.4.3 Plastic Scintillators

Thin plastic scintillators measure the time-of-flight (TOF) of the fragment, which is critical for particle identification. When a particle hits the plastic, scintillation light is emitted and then collected in photomultiplier tubes at either ends of the scintillators. Although the S800 focal plane has several plastic scintillators, the only one used in this analysis is the most

upstream one (known as the E1 scintillator). This 5-mm thick scintillator doubles as the exit window of the IC to minimize energy straggling, and it stops essentially all particles of interest. The E1 scintillator also serves as the trigger signal for the S800 data acquisition.

We also use another plastic scintillator called the object (OBJ) scintillator. Located at the object position of the S800 analysis line upstream of the reaction target, the OBJ scintillator is included in the S800 data acquisition. The time difference between the OBJ and E1 scintillators provides a measure of the TOF of the recoil particle emerging from the transfer reaction of interest, and the time difference between the OBJ and RF signal from the K1200 cyclotron identifies the incoming beam.

3.5 MCPs

Micro-channel plates (MCPs) are compact arrays of single-channel electron multipliers that can be used in a wide range of scientific applications [129, 130]. Each MCP used in this work is a 0.5-mm thick array of tiny glass tubes (approximately 10 μm in diameter and 12 μm apart, center to center) painted with a conductive surface that allows for a uniform bias voltage to be applied across the MCP and therefore across each tube [130]. Each MCP has a circular active area with a diameter of 40 mm. When an electron strikes the interior surface of a tube, it starts a cascade of electrons that are accelerated further down the tube and subsequently produce more electrons upon each collision with the interior surface. The resulting avalanche of electrons then exits on the other side. Figure 3.12 illustrates this amplification process for two MCPs in the "chevron" stack configuration that was used for this experiment. The change in direction of the glass tubes reduces positive ion feedback by preventing ions generated at the outgoing surface to re-enter the tubes and generate false

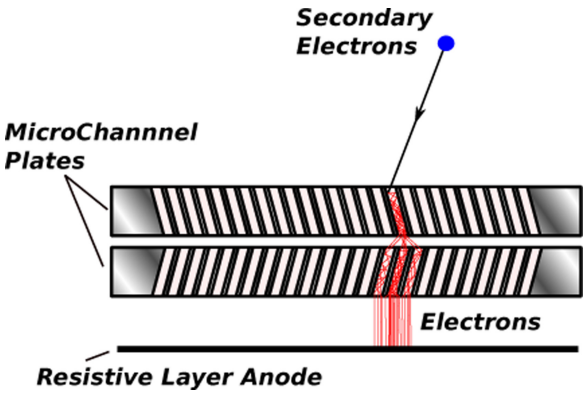

Figure 3.12: Diagram showing the operation of MCPs in the chevron configuration. Electrons strike the conductive surface on a glass tube in the MCP, resulting in a cascade of electrons and amplification of the signal. After two stages of amplification, the resulting electrons are detected on a resistive anode. Figure taken from [130].

signals. For convenience of nomenclature, in general the term "MCP" will be used to refer to a *stack* of MCPs (like the one shown in Figure 3.12), rather than a single wafer.

In this experiment, two MCPs tracked the secondary beam upstream from the target position. The upstream MCP (referred to as MCP0) sat 1 m upstream from the downstream MCP (referred to as MCP1), which was located about 10 cm upstream from the target. Each MCP was set up as shown in Figure 3.13 with a bias voltage of approximately 2000 V. In this figure the beam, traveling left to right, passes through a layer of aluminized Mylar foil. The beam striking the foil excites electrons, and those electrons excite more electrons. These secondary electrons are accelerated towards the MCP by a 1000 volt potential difference between the foil and the surface of the MCP. A permanent magnet (manufactured by Magnet Sales & Manufacturing Inc with a surface magnetic field of 14 kG) confines the electrons within a tight helical orbit as they travel towards the MCP. After amplification, the electrons emitted from the MCP are collected on a square resistive anode. We measure the signal amplitude at each of the four corners of the anode, and we can use this information to reconstruct the position of the electrons on the anode (and subsequently the position of

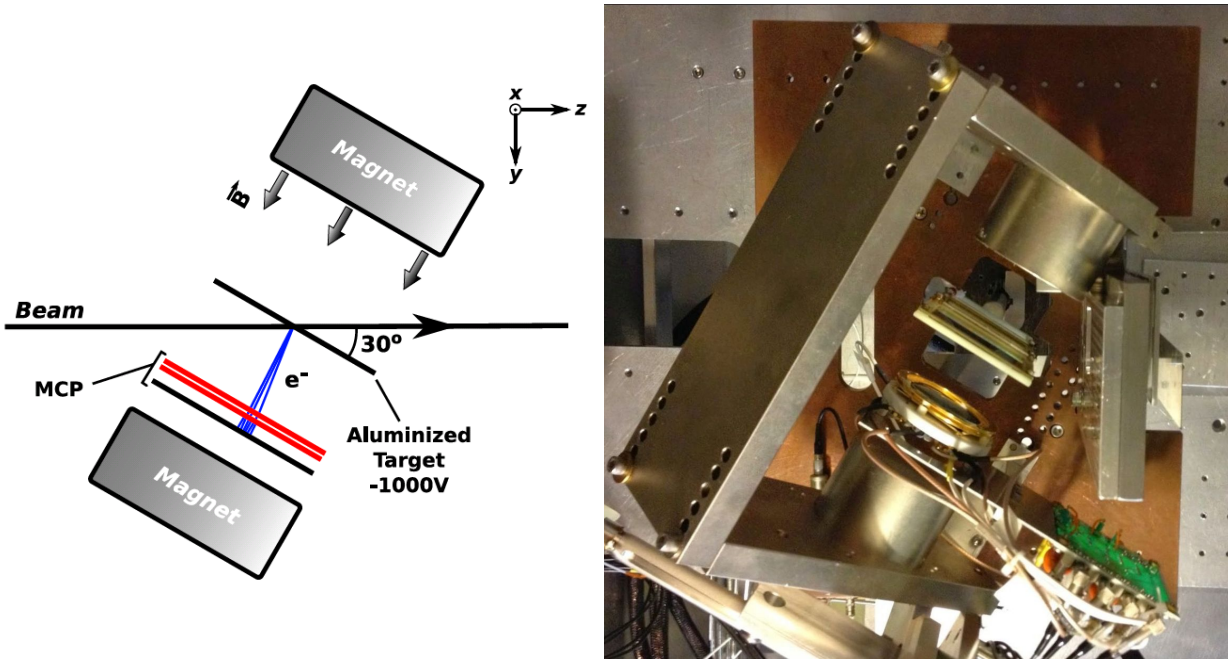

Figure 3.13: On the left is a schematic of an MCP setup, and on the right is an overhead picture of the MCP1 setup in the beamline. Two such setups were used in this experiment. Detailed description can be found in the text. Modified from [131].

the beam hitting the Mylar foil). This entire tracking-detector setup is rotated to allow for the beam to continue downstream. We installed a magnetic shield between the downstream MCP and the target position in order to keep the magnetic field from influencing the reaction products.

We implemented two gain stages for each MCP corner signal in order to extend the dynamic range. From the MCP, each corner signal goes to a fast amplifier, after which it is split. One signal proceeds directly to a CAEN V792 QDC for digitization (referred to as the low-gain channel), while the other passes through an additional stage of amplification first (the high-gain channel) before proceeding to the QDC. The timing signal from each MCP is amplified, sent to a constant-fraction discriminator, and digitized with a CAEN V1190A TDC.

3.6 Position Measurements

Measuring a differential cross-section requires precise and accurate knowledge of the trajectories of particles going into and out of the reaction target. And knowledge of these trajectories requires precisely knowing the positions of all experimental equipment in the reaction chamber. These positions were determined with a portable coordinate measuring machine (CMM) arm after the conclusion of the experiment. This commercially available CMM arm, called the ROMER Arm Infinite 5024, is capable of measuring exact positions in three dimensions within 100 μm. Furthermore, by tracking the ROMER Arm probe along a surface, higher dimensional features (like planes) can be measured. The ROMER Arm was used to determine points and planes on each of the two MCP setups, the target ladder, each HiRA telescope, and several calibration pucks glued to the walls of the chamber. We then measured these pucks with a laser tracker system in order to relate the local ROMER Arm coordinate system to the global laboratory coordinate system. Figure 3.14 shows the ROMER Arm being used during the position measurements.

The ROMER Arm requires physical contact between the probe and the point or surface of interest. Clearly, this means that we could not measure the delicate silicon detectors directly. Instead, we measured the aluminum frame that holds the Mylar foil on each telescope, and extrapolated the positions of each silicon pixel using the HiRA design drawings. We then transformed these values from the ROMER Arm coordinate system to the global coordinate system of the laboratory frame. Figure 3.15 shows the determined laboratory angles of each pixel of HiRA.

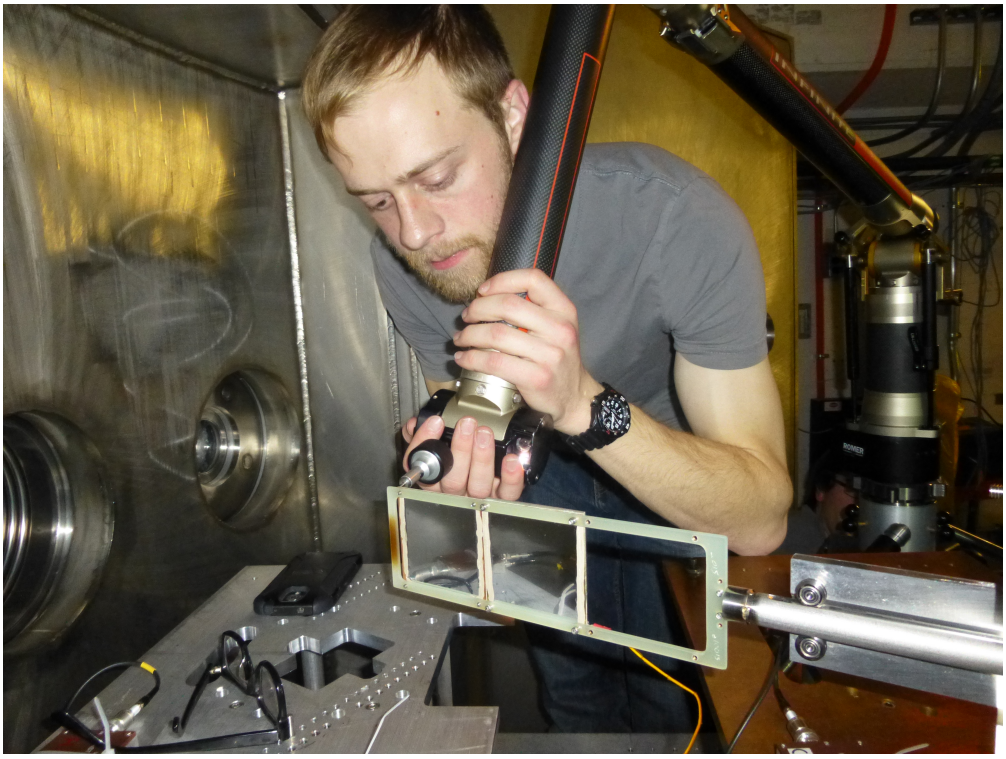

Figure 3.14: A graduate student (Jonathan Barney) measures positions on the target ladder that held the MCP0 Mylar foil and MCP0 calibration mask.

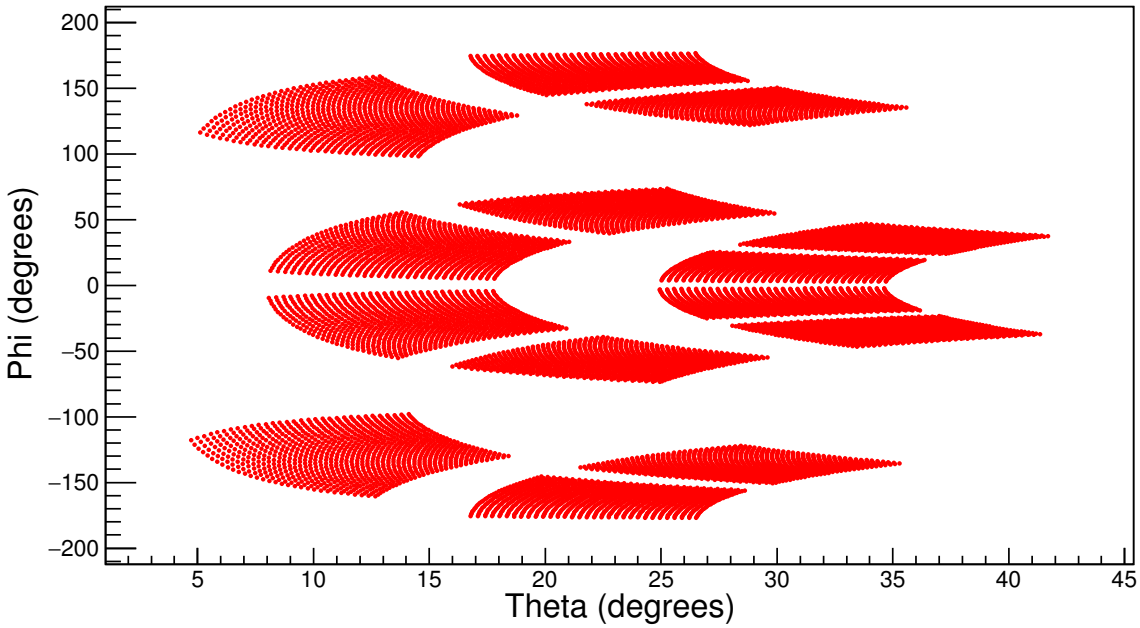

Figure 3.15: Angles of each pixel in all 14 HiRA telescopes calculated from ROMER arm measurements.

Chapter 4

Data Analysis I: Calibrations and Corrections

> Although the information was not perfect, it had the merit of existing.
>
> Thomas Piketty

Data gathered by the experimental systems described in Chapter 3 does not immediately provide scientific insight. We must *analyze* the data to turn the raw values encoded by the electronics into physically meaningful quantities for interpretation. This chapter describes in detail the analysis procedures applied to the raw data from the HiRA, S800, and MCP experimental systems.

We performed the analysis using the ROOT object-oriented analysis framework written in C++ [132]. For each detector system, a C++ object defined characteristics of the detector in a hierarchical structure known as a ROOT Tree. Consider as an example our ROOT HiRA data structure: each HiRA telescope object contains three 32-strip silicon detector objects (one each for the DE, EF, and EB) and one four-crystal CsI array object. Each object has associated data members and methods specifically designed to store and analyze data from the particular detector element that the object represents. These objects are stored in a ROOT file format for each event. This organization makes it easy to loop over all events when doing analysis tasks like making histograms or applying cuts. ROOT enables

both advanced, large-scale processing as well as simple, exploratory analysis via the ROOT interpreter.

Figures 4.1 and 4.2 show flow charts describing the overall data analysis scheme. During the experiment, the data acquisition system recorded the data into a binary file format. The first step in the analysis pipeline is to unpack this raw binary file into the ROOT file format, in which the electronics signals in the binary file are mapped to the appropriate detector objects. Then, detector-specific processing methods calibrate and correct each individual detector system. The resulting calibrated detector files correspond to real, physical quantities (like energy or time). Next, we combine the calibrated detector files so that the separate detector systems can be associated with each other on an event-by-event basis. Here we can gate on transfer reactions and calculate more observables like excitation energy spectra and angular distributions. After the final steps of background subtraction and normalization, we have in hand the desired absolute differential cross sections.

This chapter will discuss the calibrations and corrections for each individual detector system. In other words, we describe here all steps in Figure 4.1 above the gray dotted line, including the entirety of Figure 4.2. The event generation stage and all the analysis downstream will be presented in Chapter 5.

4.1 HiRA

We measured outgoing deuterons from the (p, d) transfer reactions with the High Resolution Array (HiRA). As described in Chapter 3, each HiRA telescope contains silicon strip detectors (the single-sided, 65-μm, DE detector and the double-sided, 1500-μm E detector) as well as four CsI scintillator crystals. The intersection of front and back strips in the E pro-

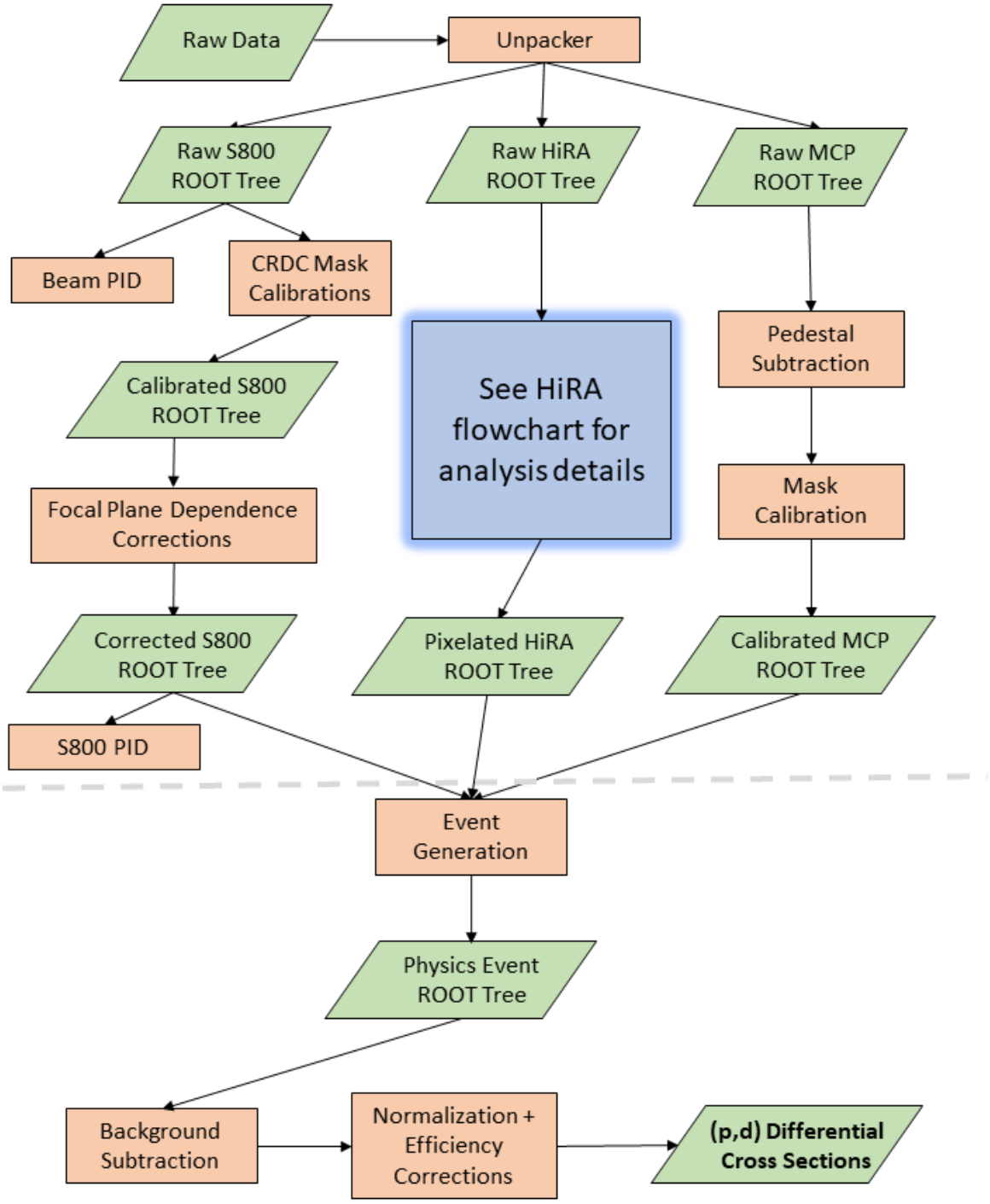

Figure 4.1: Data analysis flowchart from raw data to the final differential cross section observables. Chapter 4 describes the analysis above the gray dotted line, and Chapter 5 describes the analysis below the gray dotted line.

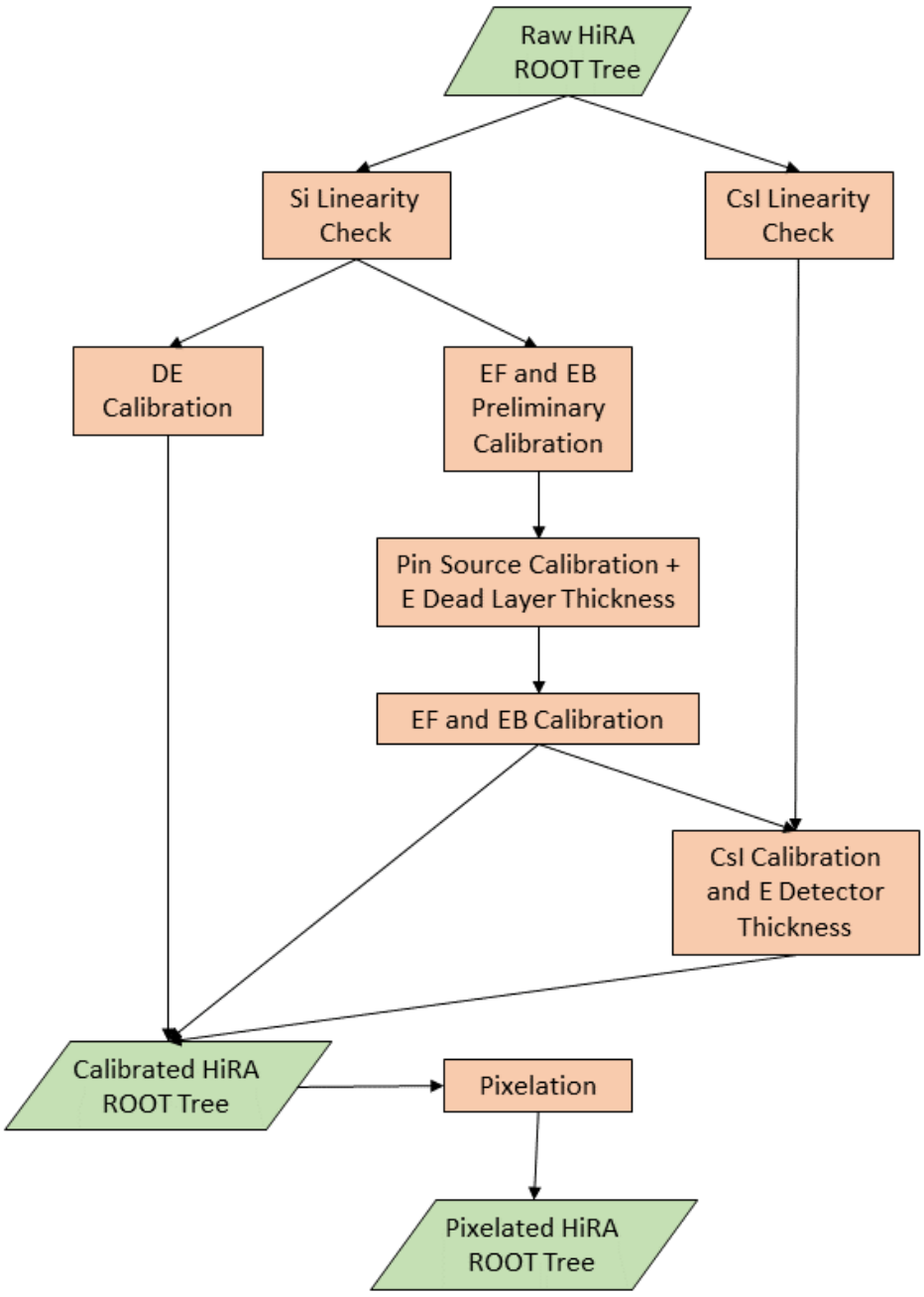

Figure 4.2: Flowchart for the HiRA data analysis from the raw ROOT Tree to the pixelated ROOT Tree.

vide excellent position resolution. We can identify charged particles by comparing detected energies in different detector layers.

For each run, the unpacker creates a ROOT file filled with raw data (e.g. energy units of ADC channels) that needs analysis in order to become physically meaningful (e.g. energy units of MeV). HiRA provides the energy and angle information for reconstructing the excitation energy spectra (and therefore the differential cross sections), so calibrating HiRA carefully is a worthwhile investment of effort. This section describes the stages of analysis of the HiRA data, including pulser linearity checks, energy calibrations, detector characterizations, particle identification, and pixelation. Some of this analysis was recently published [133], and portions of that article are included below in accordance with the Elsevier permission guidelines.

4.1.1 Linearity

An increase in the input signal going into an electronics circuit should cause a corresponding increase in the output signal. When this relationship can be fit well with a first-order polynomial, the electronics response is called *linear*. We checked the linearity of the detector electronics for both the silicon and the CsI using a BNC PB-5 pulser. The pulser introduced a known amount of charge into the electronics circuit in order to simulate the detector signal. By "ramping" the pulser across a range of voltages, the output of the electronics circuit can be compared to the incoming pulser signal in order to determine if the electronics output scales linearly with the pulser voltage. If so, then we can be confident that the detector electronics will respond linearly to the charge coming from the real detector, and therefore to the energy of the detected particle.

This linearity check can be performed directly on the raw HiRA pulser data. Figures

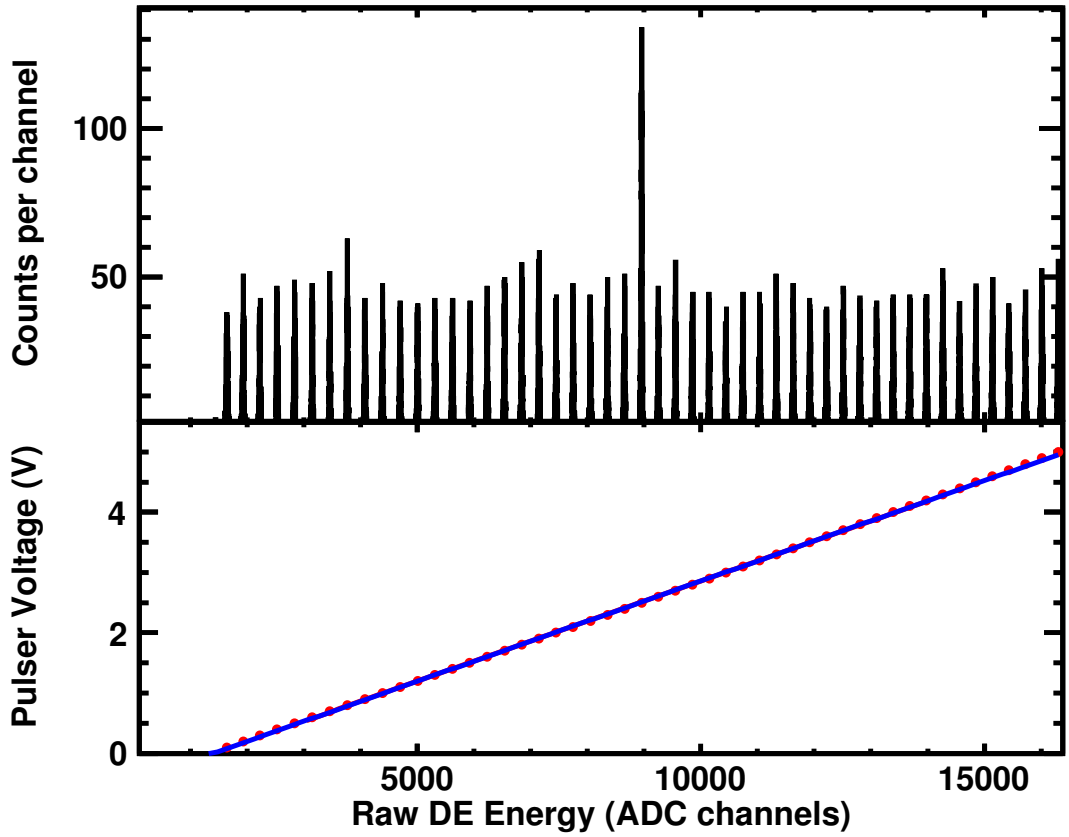

Figure 4.3: Pulser ramp for an example DE silicon strip. The top panel is a histogram showing the electronics output (in ADC channels) for many clearly resolved pulser peaks. The bottom panel displays the relationship between ADC channels and pulser voltage. Each peak in the top panel corresponds to a red dot in the bottom panel. The blue line is a linear fit to the red dots in the central $\approx 80\%$ of the full dynamic range.

4.3, 4.4, and 4.5 show example pulser linearity checks for an example strip from each silicon detector and an example CsI crystal, respectively. The silicon strip electronics is linear in the central $\approx 80\%$ of its dynamic range and the CsI crystal electronics is linear up to $\approx 50\%$. Both of these electronics systems provide enough dynamic range to measure the deuterons of interest.

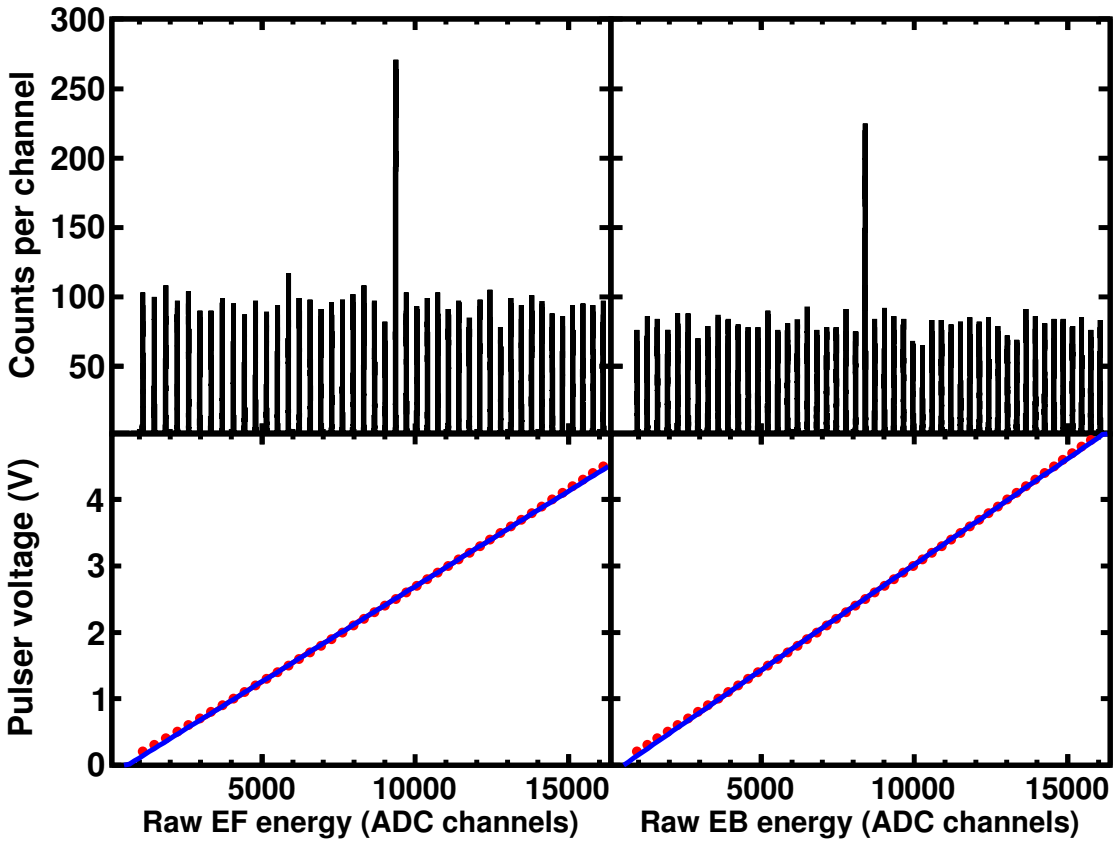

Figure 4.4: Pulser ramps for example EF (left column) and EB (right column) silicon strips. Both columns are set up similarly to Figure 4.3. The blue line is a linear fit to the red dots in the central $\approx 80\%$ of the full dynamic range.

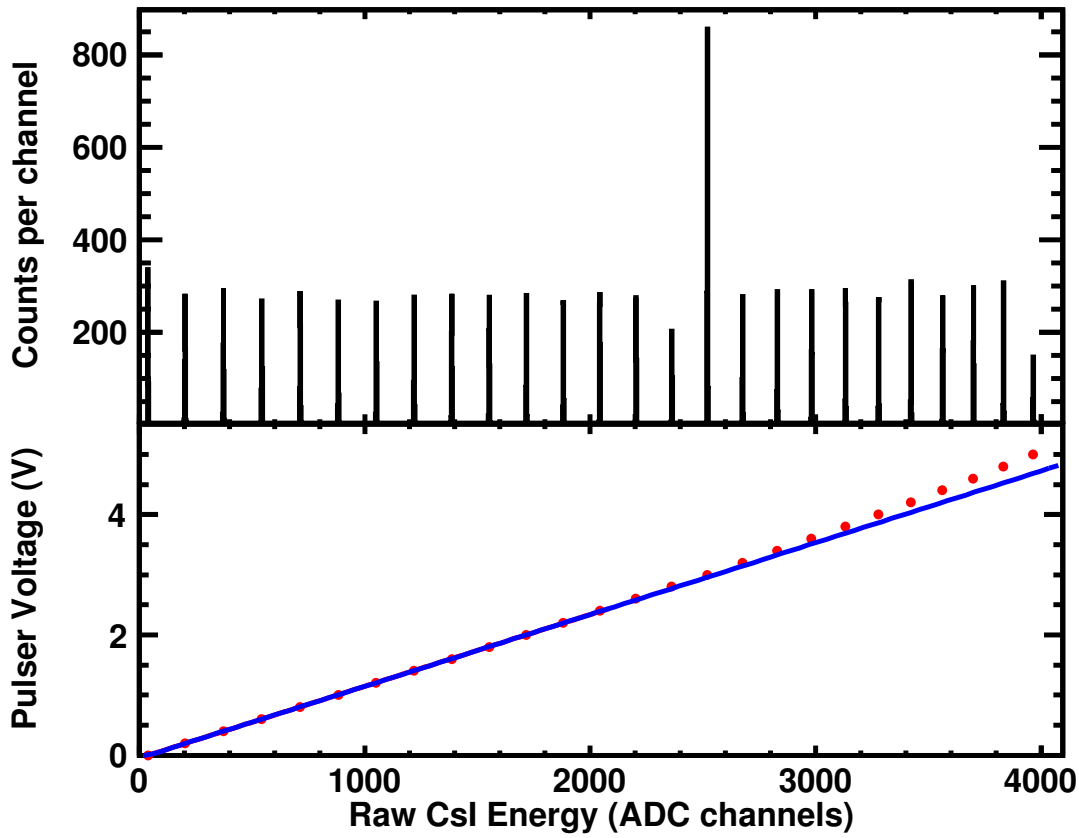

Figure 4.5: Pulser ramp for an example CsI crystal set up similarly to Figure 4.3. The blue line is a linear fit to the red dots up to $\approx 50\%$ of the full dynamic range.

4.1.2 Silicon Energy Calibration

We now associate the raw silicon electronics output (in ADC channels) to detected particle energy (in MeV). To do this mapping, we placed a radioactive source with well-known decay energies in front of the silicon detectors. Each strip of each silicon detector (1344 in total) requires a unique calibration. Since we have already checked that the electronics response is linear in the previous section, the energy calibration can be a simple linear function of the raw channels.

A ^{228}Th alpha source is commonly used to calibrate silicon detectors and is the calibration source of choice for the HiRA E and DE detectors. Using a ^{228}Th source has three key advantages. First, there are six clearly separated peaks with energies from about 5 MeV to about 9 MeV. Second, ^{228}Th sources of various strengths are commercially available. Lastly, ^{228}Th has a relatively long half-life (1.9 years). The source used in the current work was electroplated onto a platinum surface, and then fixed in an aluminum holder (12.7 millimeters in diameter and 6.35 millimeters tall) with a 100 μg/cm^2 gold window. Figure 4.6 shows the decay radiation of ^{228}Th and its daughters [134], and Figure 4.7 shows an example E energy[1] spectrum in which the peaks from these decays can be clearly seen. In HiRA calibrations, typically the five largest peaks are used.

Because the DE detector blocks alpha particles from passing through to the E, calibrating the E with a ^{228}Th source requires removing the DEs from all telescopes. This can only be done by disassembling the entire array, removing the DE detectors, and then reassembling the array. Since energy calibrations can be sensitive to minor changes in electronics and cable configurations, we must confirm that the performance of the E detector after reassembling

[1]This phrase can be somewhat ambiguous since the E detector detects each particle twice: in the front (EF) and the back (EB). In this work, "E energy" always refers to the energy from the EF due to its higher resolution and the EB having a higher probability of charge splitting (discussed in Section 4.1.6).

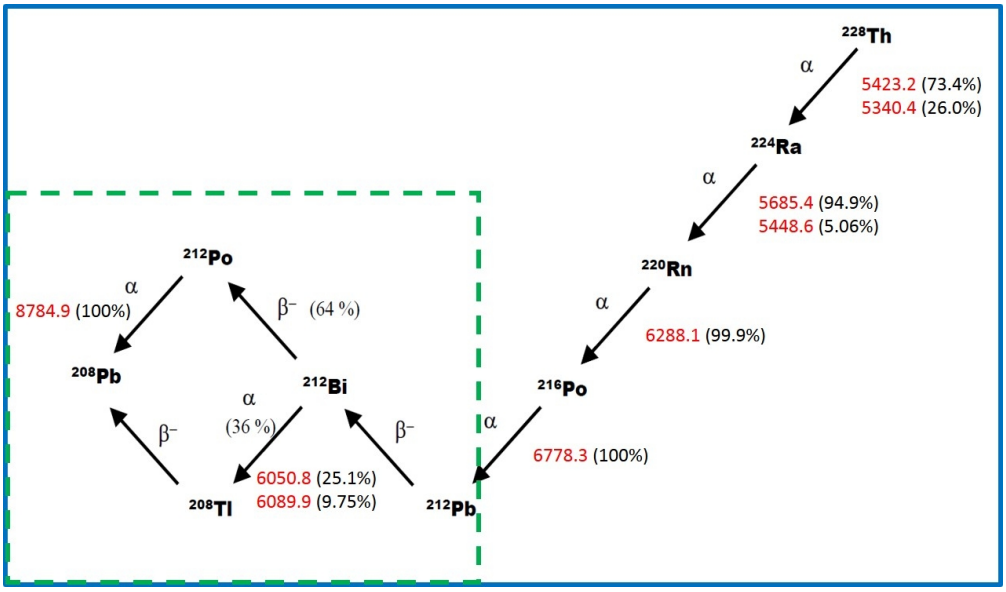

Figure 4.6: Decay scheme for ^{228}Th. The green dashed box includes all decay radiation from ^{212}Pb, the isotope that is primarily deposited onto each pin source. Energies for all alpha decays with branching greater than 1% are shown in red, along with the corresponding branching rates [134, 133].

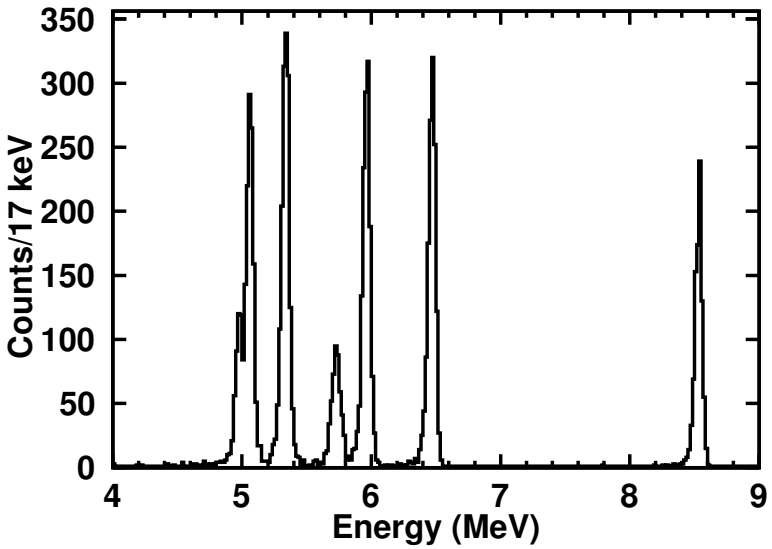

Figure 4.7: ^{228}Th calibrated alpha spectrum for an example HiRA EF detector. The DE and EB spectra look similar. Energy losses in the gold window, the Mylar foil in the front of the HiRA telescope, and an approximate E dead layer are taken into account. Typically, a HiRA silicon calibration will use the 5 most prominent peaks seen in the spectrum. The resolution in this detector is 65 keV (FWHM) [133].

the array is consistent with the performance of the E prior to disassembly. Ideally, if an alpha source can be inserted between the DE and E detectors, the E detector can be calibrated without disassembling the HiRA telescope.

To resolve this issue, each HiRA telescope can features a slot between the DE and the E detectors for insertion of a pin source, which is made from a small metal pin [133]. One end of the pin is covered with isotopes from the decay chain of ^{228}Th (primarily ^{212}Pb). To make these pin sources, we applied a negative bias to a bundle of pins placed in front of a 13 μCi ^{228}Th powder source. When ^{228}Th decays to ^{220}Rn, which has a relatively long half-life (56 seconds), some of the gaseuos ^{220}Rn ions drift to the negatively-charged pin electrodes. The ^{220}Rn then decays into the short-lived ^{216}Po and the much longer-lived ^{212}Pb (0.1 seconds and 10.6 hours, respectively), which are metals and generally stick to the head of the pin. After about 24 hours of irradiation, we mounted each of the pins on a frame and then inserted each frame into the aligned slot between the DE and E detectors (as seen in Figure 4.8) so that alpha particles are emitted directly onto the E detector without having to disassemble the array. The HiRA telescope was designed so that the pin mounted in the frame sits 3.2 mm above the surface of the E detector when the frame is inserted into the slot. Since the ^{212}Pb on the pin source is far down the decay chain of ^{228}Th, only two peaks feature prominently in the observed energy spectrum (as shown in the green box in Figure 4.6) [134]. The collected data can then be used as a standalone calibration or to validate the ^{228}Th calibrations at the end of an experiment. The latter option is in general preferable since the ^{228}Th data have more peaks to use as calibration points.

The relevant decays for the pin source inserted into HiRA are shown in the green dashed box in Figure 4.6. An example spectrum in Figure 4.9 illustrates that there are only two peaks in the pin source data: one that corresponds to an 8.785 MeV decay and a lower

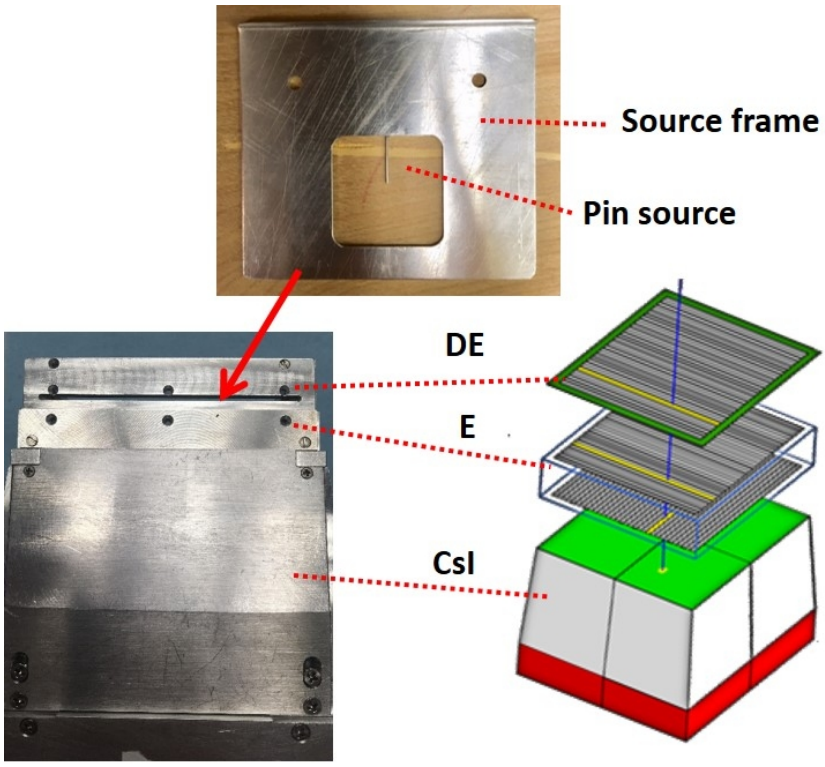

Figure 4.8: HiRA telescope assembly. On the bottom left is a side-view photograph of a HiRA telescope. On the bottom right is a cartoon of the detectors contained within the telescope. Dotted red lines connect the detectors in the cartoon to their approximate positions in the telescope. On the top of the figure is the pin source frame with the pin source installed. The pin source slot is located between the DE and the E detector as indicated by the thick red arrow [133].

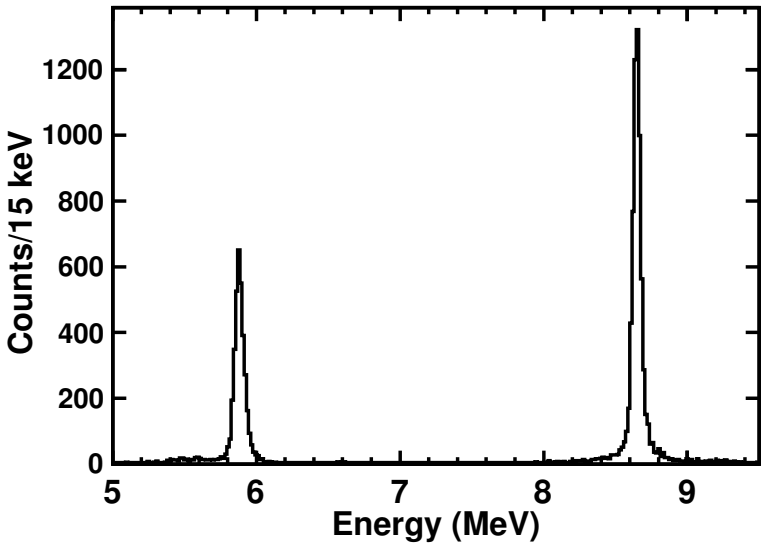

Figure 4.9: Example pin source alpha spectrum for one pixel in one E detector [133].

energy peak that actually consists of two unresolved alpha decay peaks (one at 6.051 MeV and another at 6.090 MeV). The relative probabilities of these two unresolved decays are well known, so these two energies can be combined via a weighted sum to yield a single peak energy of 6.062 MeV. These are not the peak energies that are seen in the detector: alpha particles will lose energy in the dead layer so the measured energies will be below the decay values. Fortunately, these deviations allow for measurement of the dead layer thickness (as shown in the next section).

When the preliminary ^{228}Th calibration is applied, the pin source peaks look reasonably close to the expected energies. This validates that the detector performance after the experiment is consistent with that of the experiment itself. Now, the calibration can be further improved by measuring the thickness of the dead layer on the E detector.

4.1.3 Silicon Dead Layer Thickness

The pin source also provides another ingredient to a proper E energy calibration: determination of the thickness of the dead layer. During fabrication of a silicon detector, a "dead layer" is typically formed on the surface to protect the active silicon wafer of the detector [124]. Energy deposited by charged particles in this dead layer is not detected. Therefore the dead layer affects the accuracy of charged-particle energy measurements. Silicon-detector dead layers have previously been measured using low energy electrons [135] and proton bremsstrahlung [136].

The pin source is nestled between the DE and the E, so alpha particles from the pin do not need to pass through a gold window or Mylar foil to reach the detector (as is the case with alpha particles from the thorium source). Therefore the dead layer is the only potential cause of energy loss between the source and the active detector volume, as shown in the cartoon in Figure 4.10. We perform this calibration under vacuum, and the thickness of the ^{212}Pb deposition can be neglected. Furthermore, the pin itself is only 3.2 millimeters above the detector surface, so alpha particles will travel through the dead layer at a wide range of incident angles. Although the dead layer can contain a variety of materials, we assume an effective dead layer of pure silicon since our only concern is the resulting effect on charged particles. Assuming a uniform dead layer and a constant value for the energy loss, simple geometrical considerations (illustrated in Figure 4.10) dictate that the energy of the alpha particles detected at different pixels can be used to extract the dead layer thickness via the following relation:

$$E = E_0 - \frac{dE}{dx} * \frac{T}{\cos\theta} \tag{4.1}$$

where E is the detected energy, E_0 is the initial energy of the alpha particle, θ is the emission

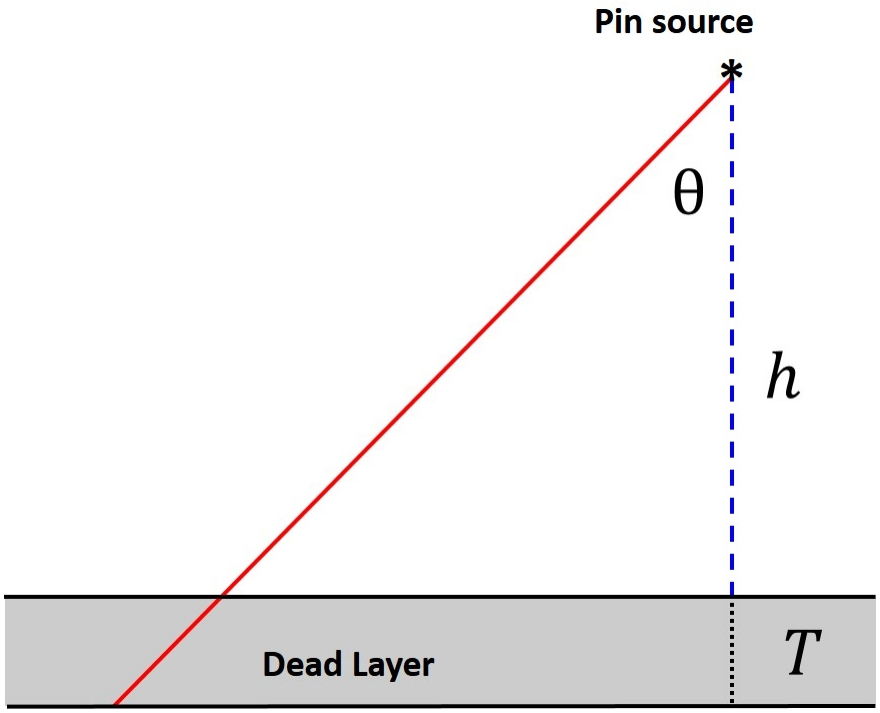

Figure 4.10: Cartoon of pin source and dead layer. The distance h between the pin source and the detector surface is 3.2 mm. The angle θ of the alpha particle from the pin source determines how much of the dead layer the particle passes through. The dead layer thickness (T) can be extracted by studying the relationship between detected energy and angle [133].

angle, $\frac{dE}{dx}$ is the stopping power of an alpha particle in silicon at energy E_0 (since the dead layer is so thin, the stopping power is assumed to be constant), and T is the dead layer thickness [133]. Since the amount of dead layer that the alpha particle traverses depends on the incident angle of the particle, the final energy of that alpha particle will also depend on the incident angle. By measuring the relationship between incident angle and detected energy, we can extract T.

The first step of measuring the dead layer has already been described in the previous section: an initial calibration using the thorium source data with a reasonable guess for the dead layer thickness (on the order of 1.0 μm based on previous studies). Since the dead layer thickness is not yet precisely known, this calibration is inexact. In the fits described below, the initial energy of the alpha particle is a free parameter in order to account for this

potential imperfection.

The next step in determining the dead layer thickness is to find the central pixel, which is the pixel that the pin source is closest to. In principle the pin source should be exactly at the center of the detector (which falls in between pixels), but in practice the pin source could be slightly misaligned and is slightly closer to one pixel than the rest. The central pixel provides a good first approximation to the precise location of the pin source. Because of its relatively large solid angle coverage, the central pixel should have more counts than any other pixel. Figure 4.11 shows a two-dimensional hit map in which the back strip axis is along the y-direction and the front strip axis is along the x-direction. The central pixel (which by definition is at the intersection of the central front strip and the central back strip) has the most counts, and the counts decrease as distance from the central pixel increases. The hit map is not perfectly concentric due to asymmetries in the deposition on the pin head, but this is a negligible effect.

Next, we performed fits for each peak of each pixel across the central front strip to determine precisely the measured energies for each pixel made by the intersection of the central front strip with a back strip. According to Equation 4.1, the central pixel should measure the highest detected energy, since the incident angle of the alpha particle is closer to 0 than for any other pixel. Figure 4.12 shows the energies for several pixels across the central front strip for an example detector, as well as a fit performed using a modified version of Equation 4.1:

$$E(s_b) = E_0 - \frac{dE}{dx} * T * \sqrt{1 + \left(\frac{d_0}{h}\right)^2 * (s_{b0} - s_b)^2} \tag{4.2}$$

where d_0 is the width of each strip (fixed to 1.95 mm), h is the distance from pin source to detector surface (fixed to 3.2 mm), and s is the back strip number for each pixel. The

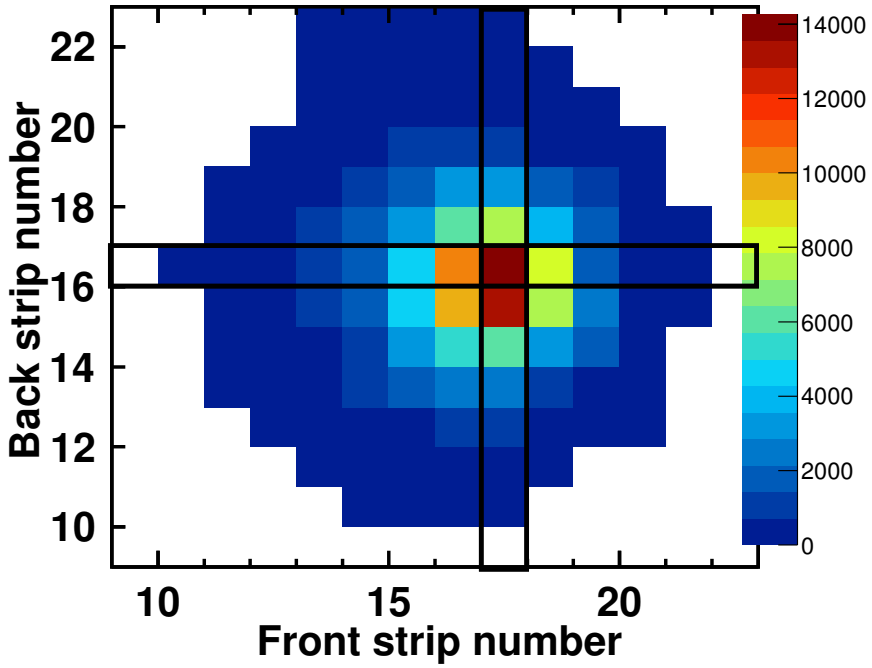

Figure 4.11: A two-dimensional hit map for the number of detected pin source counts for one E detector. The central pixel is shown at the intersection of the black rectangles (which correspond to the front and back strips with the most counts) [133].

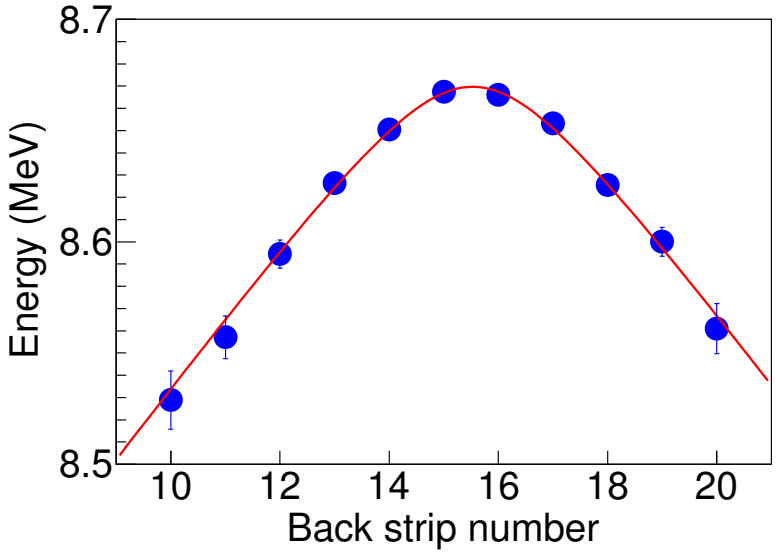

Figure 4.12: Example energy distribution with statistical error bars of the 8.785 MeV peak for different pixels across the central front strip. The corresponding fit (using Equation 4.2) is shown in red [133].

back pin source position s_{b0} refers to the exact coordinate of the pin source along the back strip axis. This position can take fractional values, e.g. $s_{b0} = 15.5$ would indicate that the pin source is located above the space in between back strips 15 and 16. The free parameters are T, s_{b0}, and E_0: E_0 is treated as a free parameter since the dead layer thickness is not known in the initial ^{228}Th calibration, so E_0 may be slightly off. A similar fit can be performed across the central back strip in order to find the front pin source position s_{f0}, defined similarly to s_{b0}.

We can extend Equation 4.2 straightforwardly to two dimensions resulting in Equation 4.3, in which case the number of data points increases since the fit is no longer limited to a single central strip:

$$E(s_f, s_b) = E_0 - \frac{dE}{dx} * T * \sqrt{1 + \left(\frac{d_0}{h}\right)^2 * [(s_{f0} - s_f)^2 + (s_{b0} - s_b)^2]} \tag{4.3}$$

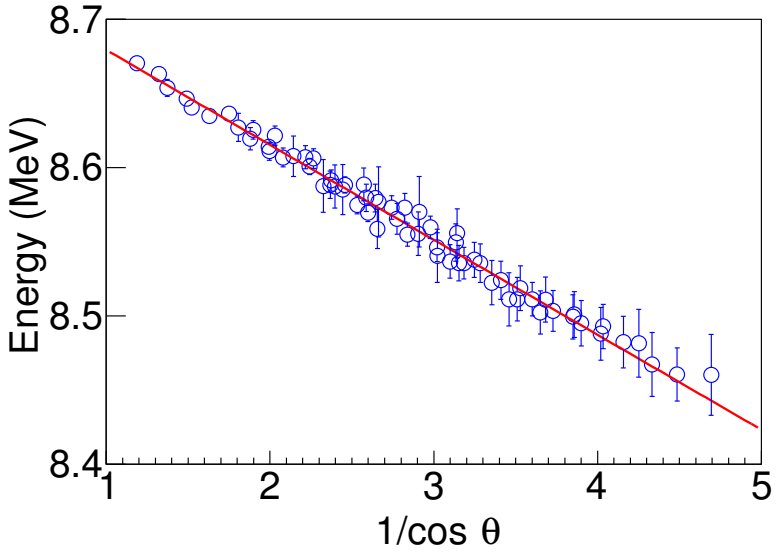

Figure 4.13: Example energy distribution with statistical error bars for the 8.785 MeV peak across all pixels in a single telescope according to different values of $1/\cos\theta$, as well as the corresponding fit [133].

where s_f and s_b are the front and back strip numbers of the pixel, and s_{f0} and s_{b0} come from the one-dimensional fits described above. The free parameters in this fit are only T and E_0. Results of an example fit are shown in Figure 4.13. The quality of the fit shows that our assumption of dead layer uniformity is valid, at least for the central area of the detector defined by the central 10 to 12 front strips and the central 10 to 12 back strips. We show the extracted dead layer thicknesses for 14 telescopes in Figure 4.14, with results for both the 8.785 MeV peak (blue square symbols) as well as the 6.062 MeV peak (red open circles). The error bars are statistical uncertainties that mainly depend on the intensity of the pin source for a given telescope. Since many pins were bundled together during the source irradiation, the ^{212}Pb isotopes were distributed unevenly across the pins. The mean dead layer value across all telescopes of 0.61 $\pm$ 0.07 μm is indicated by the dotted line [133]. Within error, this average matches the value provided by the manufacturer of 0.5 μm [137].

We can then incorporate this more accurate dead layer thickness into the thorium cali-

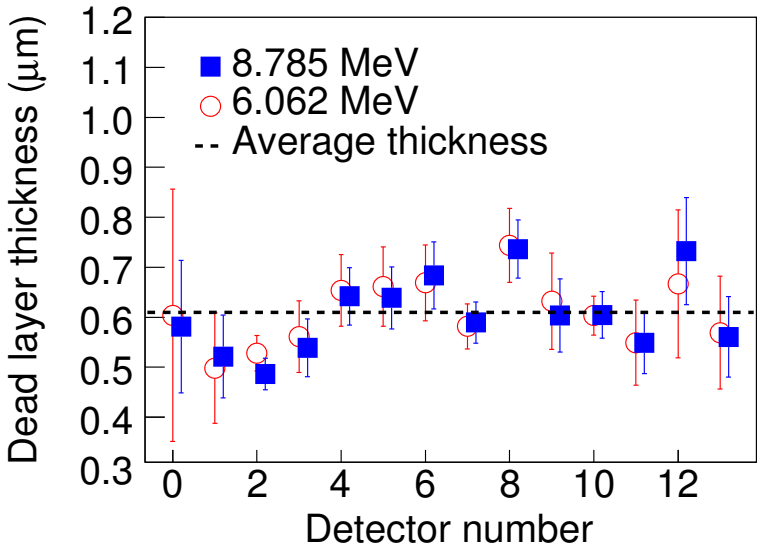

Figure 4.14: Dead layer thicknesses extracted for each E detector from both the low (red open points) and high (blue solid points) energy peaks from ^{212}Pb decay. All error bars are statistical, and the wide range of errors is due to different intensities of the pin sources. The average dead layer thickness (0.61 μm) is given by the dotted black line. Values extracted with the higher energy peak and the lower energy peak are consistent with each other [133].

bration for both the EF and the EB.

4.1.4 Particle Identification

We now have a good calibration for both the E and the DE detectors. As discussed in Section 3.3, we can use HiRA for particle identification (PID) by comparing energies in different detectors within a telescope.

Once all strips in a given detector have been calibrated, their energy signals are matched to the same energy scale and can be combined. Figure 4.15 shows an example DE-E PID plot for a single telescope in which proton, deuteron, and triton lines are clearly separated. Since this plot is only meant to identify particles that stop in the E detector, Figure 4.15 is gated on thresholds for the CsI crystals behind the E. In other words, to generate the DE-E PID, we only consider events where there are counts in the E and DE and no above-threshold

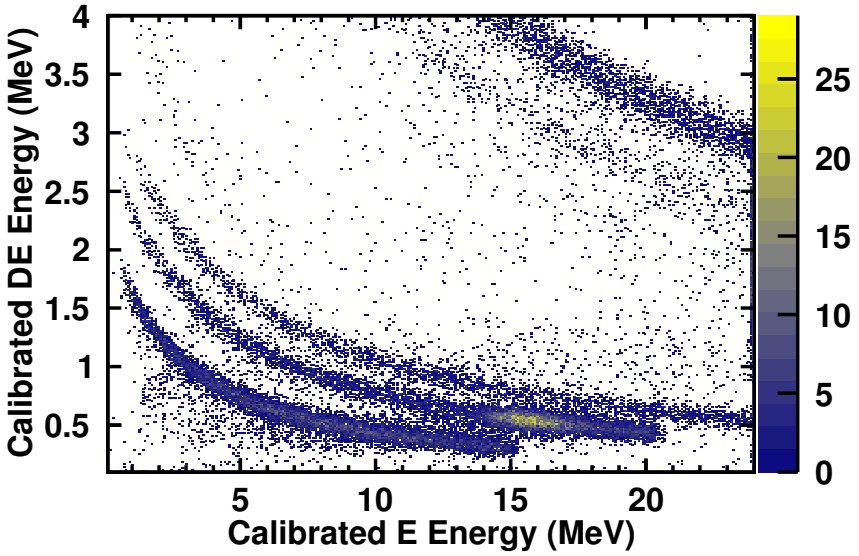

Figure 4.15: DE-E PID plot for an example telescope, with CsI thresholds applied.

counts in any of the four CsI scintillators.

For particles energetic enough to punch through the E detector, we use the E-CsI PID stage. Figure 4.16 shows an example for a single CsI crystal. Because each CsI crystal is only a single detector element (as opposed to the silicon detectors, which are made up of many strips that require many individual calibrations), we can get PID without a CsI calibration. This is rather fortuitous since CsI detector response depends strongly on Z and therefore PID is required to do a proper CsI calibration (as discussed in Section 4.1.5).

4.1.5 CsI Energy Calibration and Silicon Detector Thickness

Calibrating the CsI is not as straightforward as calibrating the silicon since the CsI is hidden behind two layers of silicon, has a relatively high dynamic range, and responds differently to particles with different Z. Below we present our CsI calibration method. An important part of this method consists of determining the thickness of each E detector, which influences the energetics of particles that punch through the E to the CsI.

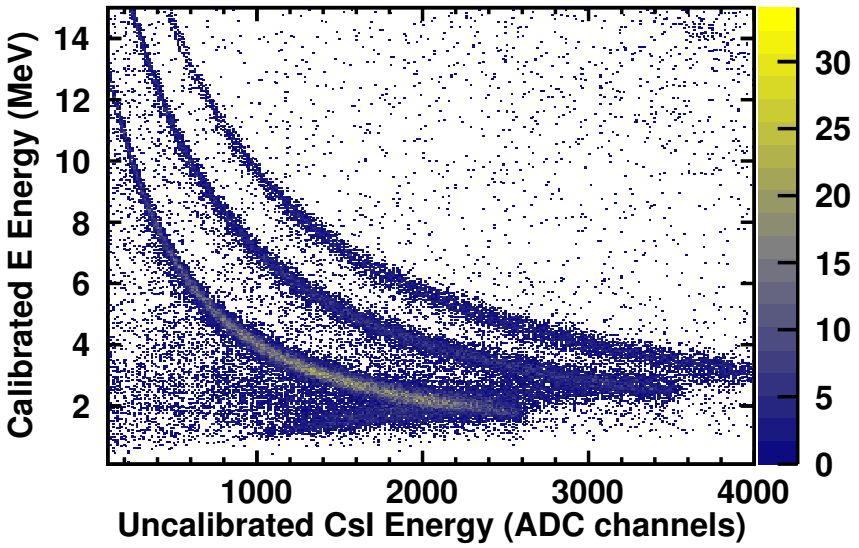

Figure 4.16: E-CsI PID plot using raw CsI energy.

One way to calibrate a CsI crystal is to accelerate and elastically scatter light-charged-particles at known energies into the crystal. For this work, we used a beam of hydrogen isotopes with a magnetic rigidity of 1.10 Tm (corresponding to a proton energy of 56 MeV). Only protons were considered in this analysis due to low intensities for the deuteron and triton beams. A CH_2 reaction target (75 μm thick) scattered the incoming light charged particles. For the most part, these particles scatter off the carbon in the target. From two-body kinematics, the energies of the elastically scattered particles at a given angle are known, and range from approximately 54 to 56 MeV. These energies are high enough to punch through both the DE and the E detectors easily (the proton punch-through energies for the DE and E detectors are 2.45 MeV and 15.6 MeV, respectively), while also stopping within the CsI, which has a proton punch-through energy upwards of 110 MeV. Since the kinematic relationship between scattering angle and energy is relatively flat (in other words, the energy is only weakly dependent on scattering angle), this results in one elastically scattered proton calibration point per crystal, as shown in Fig. 4.17. ^{12}C has an excited state at 4.439

MeV, so there is an inelastically scattered proton calibration point as well. Together, these elastically and inelastically scattered protons constrain the calibration at high energy for a given crystal. There is some scattering off the hydrogen in the plastic target, but due to the low statistics and a steep kinematic relationship (compared to proton-carbon scattering) we did not use this data.

The scattering data constrain the calibration only at high energy. The calibration of the CsI at low energies utilizes the Bethe-Bloch formula by comparing the energy lost by a charged particle punching through the E detector to the energy deposited in the CsI where the particle stops [138]. If we know the E detector thickness and have a reliable E energy calibration, we can calculate the energy deposited by a proton in the E detector (E_{Si}) for a range of incoming-proton energies (E_p) using energy-loss tables [139]. The energy deposited in the CsI crystal is therefore $E_{\mathrm{CsI}} = E_p - E_{\mathrm{Si}}$. We then use E_{CsI} to calibrate the raw CsI ADC channels corresponding to the calibrated E energy as seen in Fig. 4.17.

This procedure (which will be referred to as the energy loss method) allows for a calibration that extends well into the low-end of the dynamic range of the CsI. However, proper implementation requires precise knowledge of the thickness of the E detector since it is a critical ingredient in determining the incoming-proton energy that corresponds to the energy deposited in the E (and therefore the calculated CsI energy used to perform the calibration). Although the nominal thickness of each E detector is 1500 μm, the true value for the thickness can differ from this value by up to 100 μm [133].

We make two important notes concerning the validity of this approach. First, the energy loss method relies on the assumption that the CsI detector response is linear at low energies. To confirm this, HiRA crystals were tested via direct proton beam at Western Michigan University using several different beam energies (see Figure 4.18). The crystals were found

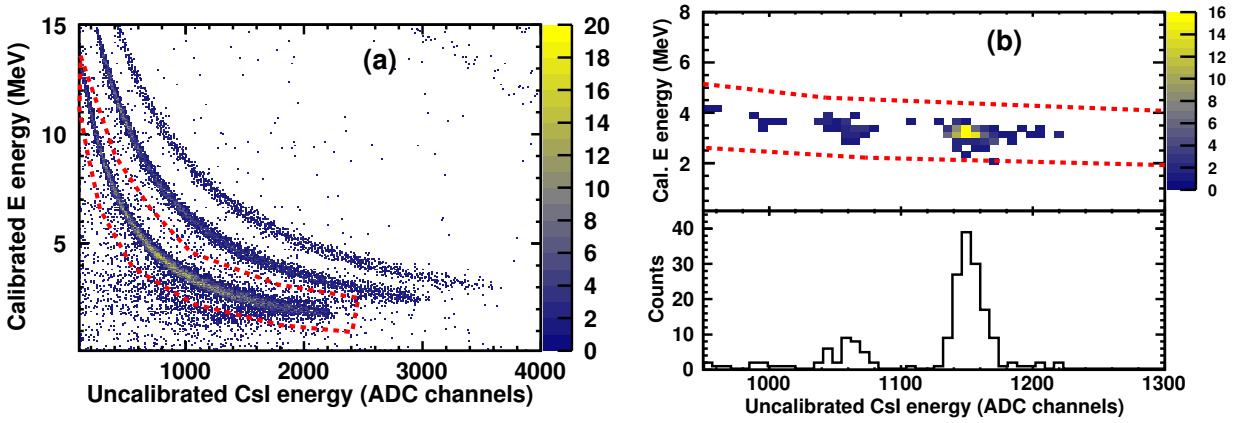

Figure 4.17: (a) HiRA PID plot for reaction data using one CsI crystal and its corresponding E silicon detector. The y-axis is calibrated energy in the E detector, and the x-axis is uncalibrated CsI energy in units of electronics channels. Protons (within the red-dashed line) can clearly be identified, even though the CsI energy is uncalibrated. (b) The top panel is the HiRA PID for the same CsI crystal as in (a), this time showing the scattering data (zoomed in to the relevant region). The red-dashed line is the same proton gate as in (a). The bottom panel is a projection of the top panel onto the x-axis. Two peaks are clearly visible: the higher energy peak corresponds to proton elastic scattering off of carbon, and the lower energy peak is from inelastic scattering ($E^*(^{12}\mathrm{C}) = 4.439$ MeV) [133].

to be linear down to approximately 1 MeV [140]. Secondly, since the CsI light output depends on the detected particle species, the energy loss method requires that only data from protons hitting the detector be used. Fortunately, by comparing single CsI crystals to their corresponding calibrated E detector, we can unambiguously identify protons in the CsI crystal even without a calibration (see Figure 4.17 and Figure 4.16).

We combined two separate CsI calibration methods in two different energy regions in order to determine the thickness of the E silicon detector within each telescope. The first calibration method is simply to use protons scattered from the CH_2 reaction target. The kinematics are well understood, so for a given angle we know the proton energy. Since these protons are at relatively high energies, they do not deposit a large amount of energy in the E, and they do not have high sensitivity to the E detector thickness; i.e. a large change in the detector thickness will only slightly change the energy lost by a high energy proton.

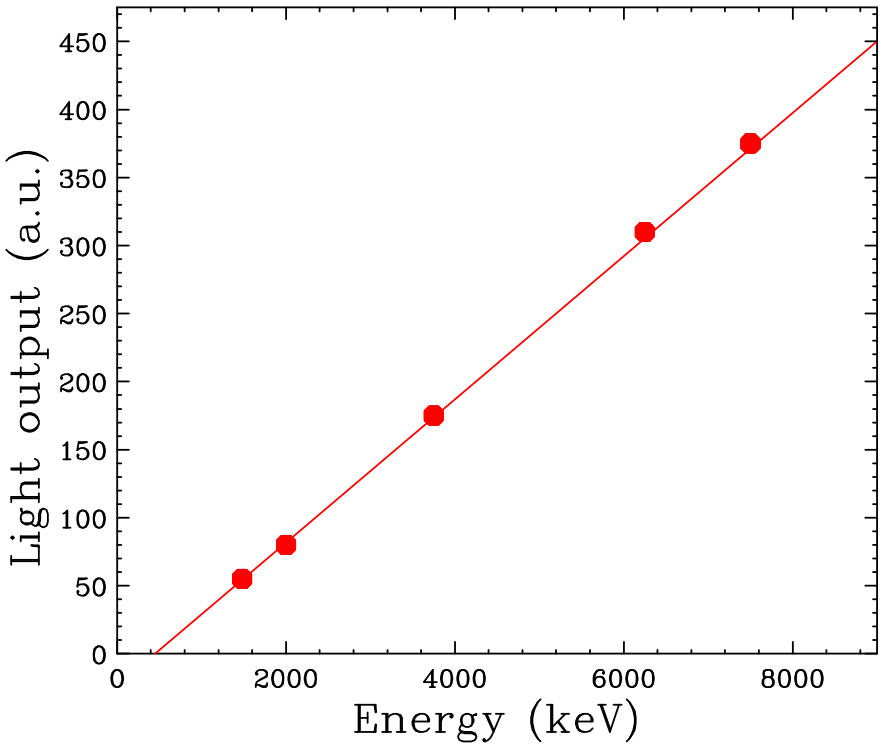

Figure 4.18: HiRA CsI light response with a direct proton beam at low energies. Data for one crystal is shown with a linear fit. Modified from [140].

However, the proton energy is so high that there is a long "lever arm" when extrapolating down to low energy. Small deviations in the high energy points will have a major impact on the low end of the dynamic range.

The second calibration method is the energy-loss method described above, which allows for a series of calibration points at low energy to be generated for a given detector thickness. These points are highly sensitive to the E thickness. The correct detector thickness should result in consistency between the low energy points calculated with the energy-loss method and the high energy scattering points. In this energy range the detector (Fig. 4.18) and electronics (Fig. 4.5) responses are linear, so therefore the energy-loss and scattering points should be collinear. To check this, the energy-loss and scattering points were calculated using detector thicknesses from 1400 μm to 1600 μm [133].

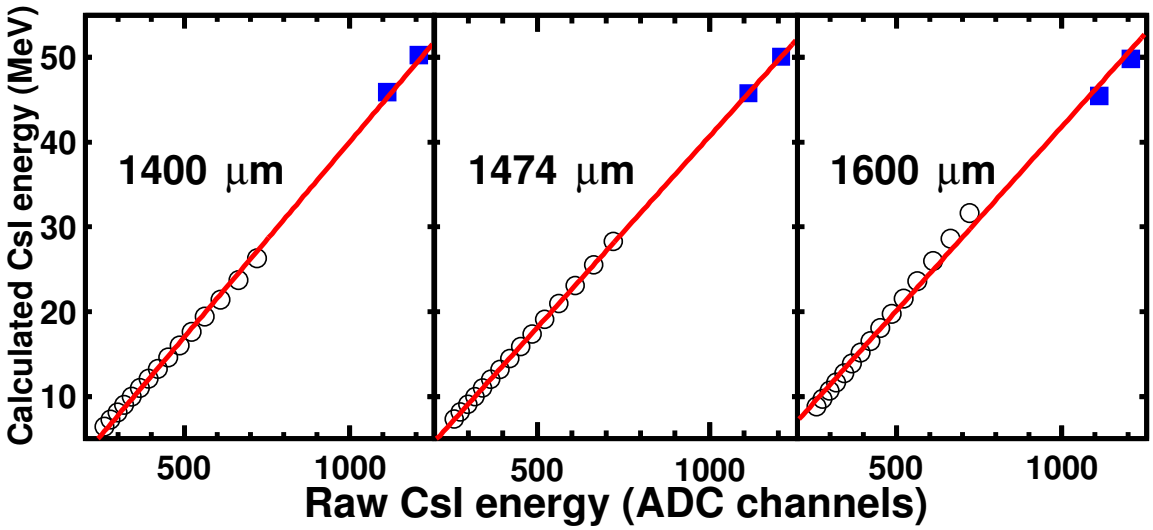

Figure 4.19: Relationship between calculated CsI energy and raw CsI channels for one telescope at three different E thicknesses. The blue squares correspond to scattered protons with well known energies that deposit a small amount of their energy in the E detector, and the open circles are calculated via the energy-loss method as described in the text using each of the three indicated E thicknesses. When fitting both sets of points together, an E thickness of 1474 μm provides the points that yield the best fit [133].

Figure 4.19 shows example plots of CsI energy vs raw CsI channels for one crystal, with CsI energies calculated using three different values for the E detector thickness: 1400 μm, 1474 μm, and 1600 μm. The blue squares are the scattering data, and the open circles are the energy-loss calculation data. All points were calculated using the indicated thickness. At the correct thickness value, these points should be collinear. As the assumed thickness value diverges from the correct value, the fit quality drops. Thus, we can extract the thickness by finding the fit with minimum Chi-square. The resulting thicknesses for 10 telescopes are directly compared to the thicknesses provided by the manufacturer in Figure 4.20 [133].

Now we can use the appropriate E thicknesses to generate deuteron calibrations for each crystal that are reliable up to $\approx$ 56 MeV.

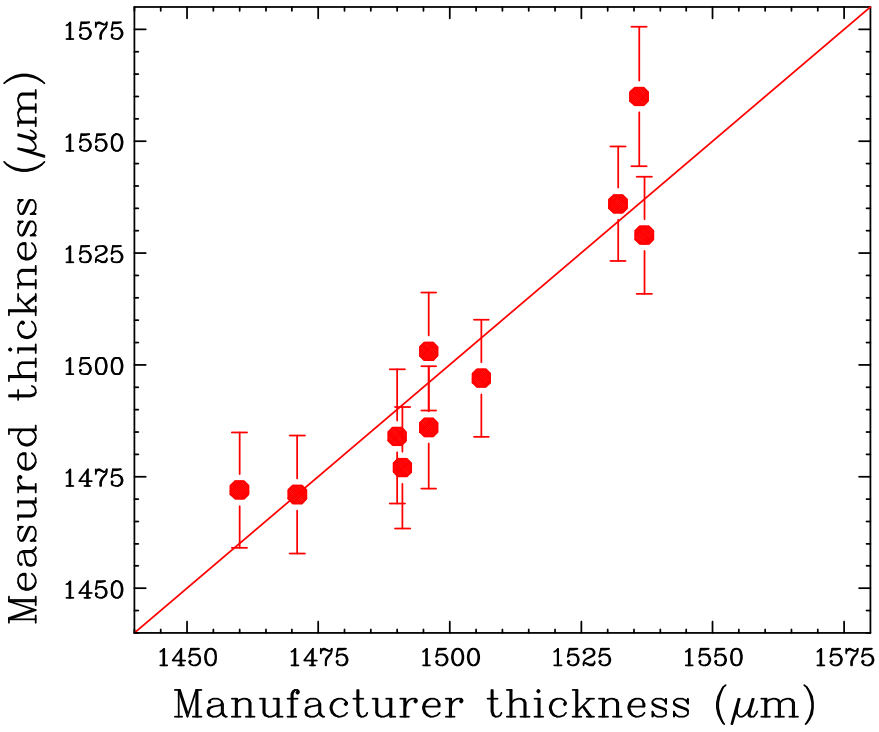

Figure 4.20: Summary of results from E thickness extraction in comparison with manufacturer provided detector thicknesses. The line corresponds to exact agreement. The measured values agree within error to the manufacturer values. Wide variation from the nominal value of 1500 μm is evident [133].

4.1.6 Pixelation

The analysis described in the previous sections results in calibrated EF, EB, and DE silicon strips, as well as calibrated CsI crystals. Next, we need to put together the calibrated information from different detectors in a given event (e.g. E_{DE} MeV deposited into strip i_{DE} of the DE detector, E_{EF} MeV deposited into strip i_{EF} of the EF detector, etc.) into a cohesive description of a single particle (e.g. a deuteron with total energy E at angle θ). We have already shown that we can identify particles (including deuterons) in two separate stages of PID: we now proceed to the rest of the analysis needed to achieve the stated goal.

Our approach is to first categorize all events in a given telescope depending on which detectors in that telescope contain data. By doing so, we leverage the fact that the data we seek will necessarily feature coincidences and correlations between detectors in a telescope. For example, any events that only contain data in the CsI and DE and none in the E clearly do not correspond to deuterons from (p, d) reactions, and can therefore be discarded. Most likely, the CsI+DE counts and other nonsensical categories are either noise or due to detector inefficiencies. The only categories with relevant data are DE+EF+EB, DE+EF+EB+CsI, and EF+EB+CsI[2]. Using this logic, we can significantly narrow down the amount of data we need to process.

We now focus on the E detector for events with potentially relevant data. When a particle deposits energy in the E, the resulting cloud of charge carriers can diffuse across the 1.5-mm thickness of the detector and be collected on more than one strip. This problem is more severe for the strips at the back of the detector (EB) than for those at the front (EF). For example, Figure 4.21 shows thorium-source data for two adjacent strips in an example EB

[2]EF+EB+CsI can contain good data despite the lack of a DE hit. For particles energetic enough to punch through the E into the CsI, the amount of energy deposited in the DE can be quite small and not always detected. We account for this easily by simulating the expected energy loss in the DE.

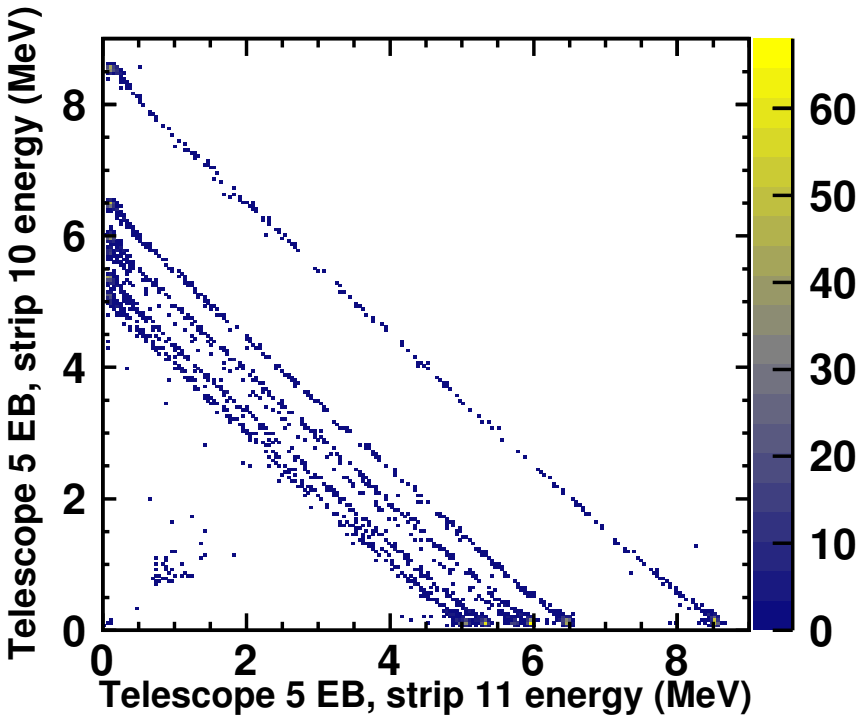

Figure 4.21: Comparison between two adjacent strips in an example EB detector. The diagonal lines indicate charge splitting from each alpha particle from the thorium source.

detector. For about 10% of the events shown, charge from a single alpha particle is split across the two strips resulting in the diagonal lines in Figure 4.21. We see a smaller charge splitting effect (1%) in the EF, as well.

Charge splitting can be accounted for by "gluing" together energies in adjacent strips that likely correspond to the same particle. For each detector in each event, we search for adjacent pairs of strips with positive energies. If the strip with a smaller energy is above a particular threshold (i.e. not noise), then we combine the energies from both strips and assign the combined energy to the strip that originally had the larger energy.

Our next step is to associate a strip in the EF with a strip in the EB to form a pixel. In the case of this experiment, HiRA detects a single deuteron whenever the (p, d) reaction occurs. This simplifies the pixelation algorithm as we need not be concerned with disentangling

multiple particles passing through a single E detector. We check that the location of the E pixel is consistent with information from other detectors. For events with data in a CsI crystal, the E pixel must be in front of that particular crystal. Otherwise, the event is thrown out. For events that stop in the E, we use the fact that DE strips and EF strips are parallel to each other to ensure that the DE and EF signals are consistent. If the DE strip is not within 2 strips of the EF strip, the event is discarded.

After performing these checks, we apply the PID gates and throw out all non-deuteron particles. Using our pixel determination, we can assign a particular detection angle to each deuteron. We know what polar angle θ each pixel corresponds to from the ROMER Arm measurements described in Section 3.6.

Finally, we calculate the correct total energy of the deuteron by combining energies from all detectors in the telescope. We include energy loss effects from various materials including the aluminized Mylar foil around the CsI crystal, the EB dead layer, the EF dead layer, the DE dead layers (on both sides of the detector), and the aluminized Mylar foil on the front of the telescope. Furthermore, we account for the energy lost by the deuteron in the reaction target, which depends on the deuteron angle. For now we assume that the reaction occurs at the center of the target. With the MCP, we can improve our determination of the deuteron angle as discussed in Chapter 5.

4.2 S800

The S800 Spectrograph (which consists mainly of two dipole magnets and a downstream set of detectors as described in Chapter 3) measured outgoing recoils from the (p, d) transfer reactions. The dipole magnets select particles (according to a set rigidity) that enter the focal

plane detector box. There, two Cathode Readout Drift Chambers (CRDCs) track particle trajectory, an Ion Chamber (IC) measures energy loss, and a plastic scinatillator (known as the E1) serves as both a time-of-flight detector and a trigger for the data acquisition system.

The two primary goals for the S800 analysis are to identify heavy recoils from (p, d) reactions, and to identify the incoming beam. Unlike in the case of HiRA, we are not concerned with precise calibrations and measurements using the S800: our aim is simply to identify particles. To do so, we use the energy loss (ΔE) measured in the ion chamber as well as various times-of-flight (TOFs) relative to the E1 scintillator. Here we describe the S800 analysis, including beam identification, the CRDC position calibration, and the trajectory corrections necessary for the S800 PID.

4.2.1 Beam Identification

Identifying incoming beam particles is critical in order to ensure that we are studying the correct transfer reactions. To perform this identification, we take advantage of the fact that at a given rigidity, particles with different mass and/or charge will have different velocities. Therefore, we can use the measured TOF through a given segment of the beam line to distinguish beam particles. The spread in the momentum of the beam makes this distinction challenging if only using one TOF, so we instead look at the correlation between two TOFs.

The E1 scintillator at the focal plane of the S800 served as the S800 data acquisition trigger as well as the start signal for all TOF measurements. The TOF-OBJ is between the OBJ scintillator in the analysis line of the S800 and the E1. The TOF-RF is between the RF signal coming from the K1200 cyclotron and the E1. PID plots comparing the TOF-OBJ and the TOF-RF are shown in Figures 4.22 and 4.23 for the ^{34}Ar and the ^{46}Ar beams, respectively. We can clearly identify separate beam species.

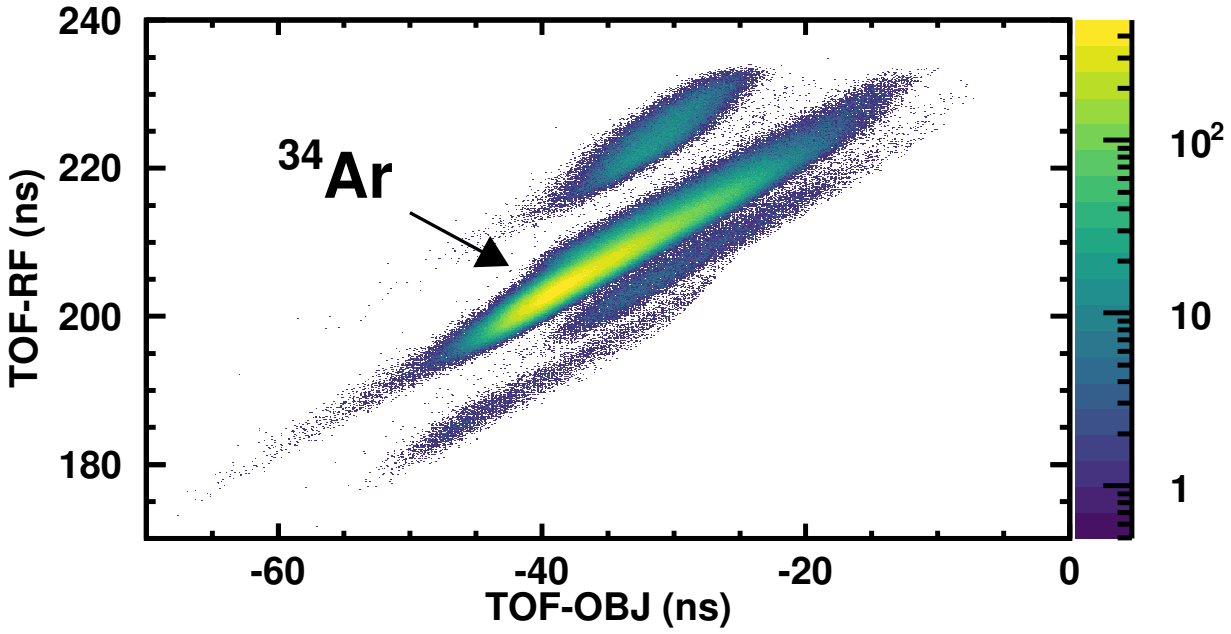

Figure 4.22: Incoming beam PID for the ^{34}Ar beam.

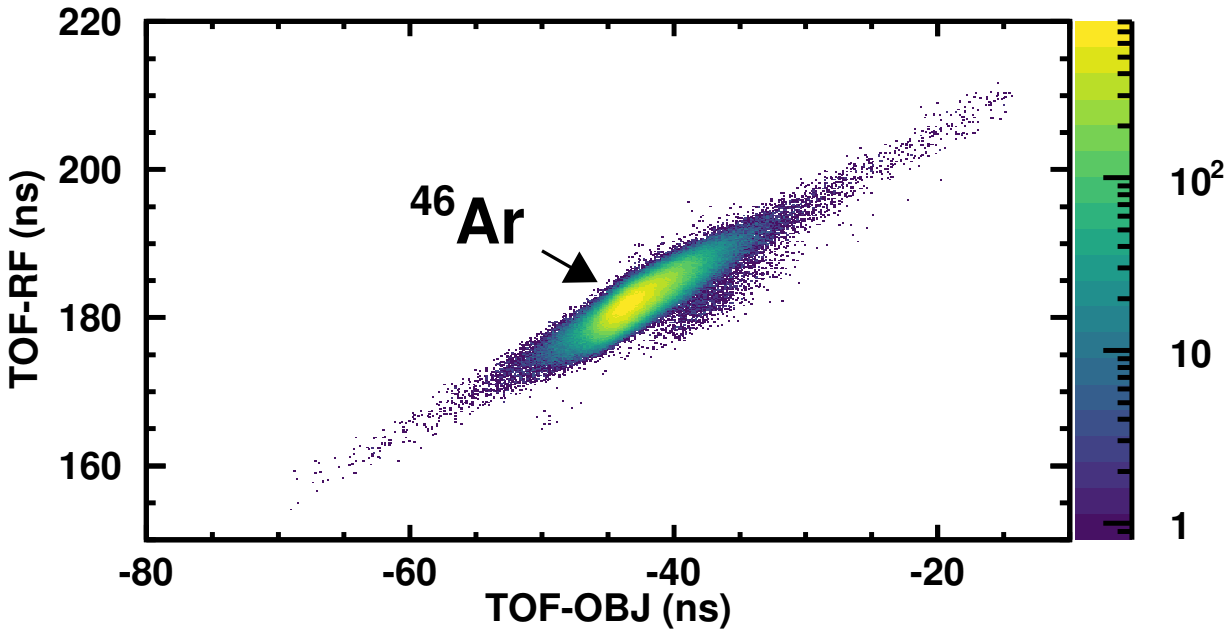

Figure 4.23: Incoming beam PID for the ^{46}Ar beam.

Using these PID plots, we can gate on the events with the appropriate incoming beam particle. We can also calculate the beam purity for each system: the ^{34}Ar beam is 94% pure, and the ^{46}Ar beam is 99.5% pure.

4.2.2 CRDC Position Calibration

Each CRDC measures the position at which the fragment passed through the detector. With the CRDC1 and CRDC2 positions, we can calculate the angle of the fragment as it travels towards the focal plane. To do this, we need to calibrate both CRDCs (from the raw electronics channels to physical distance) so that they are on the same scale.

We performed this calibration by inserting a mask with a well-defined pattern of holes in front of each CRDC. We then fit this mask spectrum with first-order polynomials in both the x (dispersive) and y (non-dispersive) directions. The slope in the x direction is known, since it depends only on the fixed geometry of the 2.54-mm cathode pads. Figure 4.24 shows example data for CRDC2. Mask data was taken periodically throughout the experiment to ensure that the CRDC detector response was stable.

Using the calibrated CRDC data, we can now calculate the angles (in both the dispersive and non-dispersive directions) of the fragment in the S800.

4.2.3 Particle Identification and Trajectory Corrections

We must identify recoil fragments in the S800 in order to properly tag on the transfer reaction channels we would like to study. We use the ΔE-TOF method to obtain the PID.

The first ingredient of this method is ΔE, the energy lost by the fragment in the ion chamber. According to Equation 3.2, this quantity is proportional to Z^2A. The second is

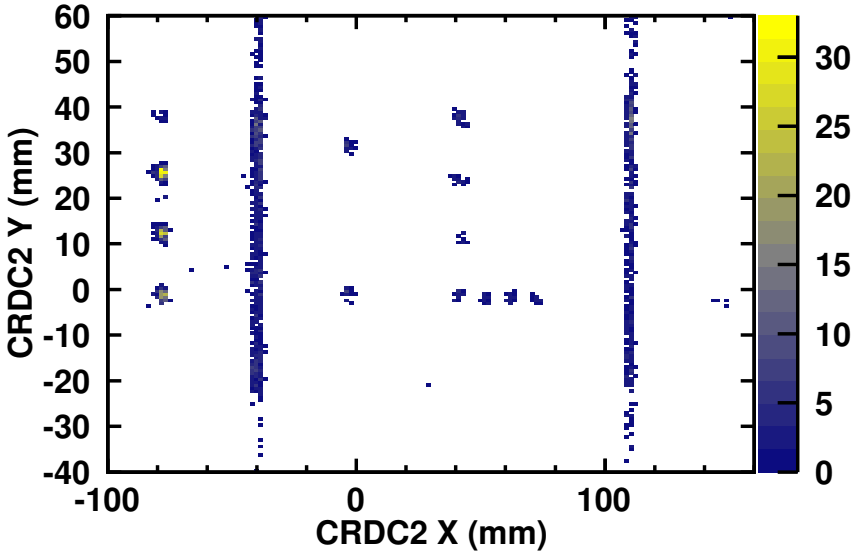

Figure 4.24: Example calibrated CRDC mask.

TOF-OBJ, the time-of-flight between the OBJ scintillator upstream of the reaction target and the E1 scintillator. As seen in Equation 3.1, the mass-to-charge ratio A/Z is related to the velocity at fixed $B\rho$, and therefore related to the TOF. We choose to use the object scintillator as the TOF stop signal, but in principle other signals could be used. Both ΔE and TOF-OBJ depend on the particle species in different ways, so we can look at the correlation between the two quantities to unambiguously identify the isotopes passing through the spectrograph.

So far we have assumed that all particles travel the exact same path through the S800. In fact, the S800 acceptance allows for substantial variation in the particle trajectory, which affects both ΔE and TOF-OBJ. To illustrate this, consider two particles identical in Z, A, and $B\rho$ that exit the target at slightly different angles. They will travel different trajectories of different lengths and will arrive at the E1 scintillator at different times (resulting in different times-of-flight). These two particles will also have different values for ΔE. The situation is further complicated by other path-dependent effects, like the propagation time

of the light in the E1 scintillator traveling to the photomultiplier tubes on either end.

Rather than microscopically modeling these effects, we follow the standard procedure of empirically correcting both time-of-flight and ΔE for dependence on focal plane coordinates (i.e. on trajectory) in an iterative process [141]. The first iteration is described in the following two equations:

$$\text{TOF-OBJ}_1 = \text{TOF-OBJ}_0 - \Big(\frac{\text{d(TOF-OBJ}_0)}{\text{d}(x_1)}\Big)x_1 - \Big(\frac{\text{d(TOF-OBJ}_0)}{\text{d(AFP)}}\Big)\text{AFP} \tag{4.4}$$

$$\Delta E_1 = \Delta E_0 - \Big(\frac{\text{d}(\Delta E_0)}{\text{d}(x_1)}\Big)x_1 - \Big(\frac{\text{d}(\Delta E_0)}{\text{d}(y_1)}\Big)y_1 \tag{4.5}$$

where x_1 is the x-coordinate in CRDC1, y_1 is the y-coordinate in CRDC1, and AFP is the dispersive focal-plane angle. TOF-OBJ$_n$ and ΔE_n are the time-of-flight and energy loss, respectively, after n correction iterations (so $n = 0$ corresponds to no corrections at all). Equations 4.4 and 4.5 portray the subtraction of linear focal plane coordinate dependencies from both TOF-OBJ and ΔE. These dependencies are correlated with each other, so further iterations are necessary to converge on the goal of having all derivatives in the above equations equal to 0.

To demonstrate these corrections further, we consider the ^{34}Ar beam. Figure 4.25 depicts TOF-OBJ$_0$ (a,b) and ΔE_0 (c,d) plotted against x_1 (a,c), AFP (b), and y_1 (d). In each figure, we see several bands (each of which correspond to a different Z). In all four plots we see a clear linear dependence on the focal plane coordinate. We can fit these linear correlations in order to get the parameters $\frac{\text{d(TOF-OBJ}_0)}{\text{d}(x_1)}$, $\frac{\text{d(TOF-OBJ}_0)}{\text{d(AFP)}}$, $\frac{\text{d}(\Delta E_0)}{\text{d}(x_1)}$, and $\frac{\text{d}(\Delta E_0)}{\text{d}(y_1)}$ for Equations 4.4 and 4.5. The results from this first correction TOF-OBJ$_1$ and ΔE_1 are still slightly dependent on focal plane coordinates, so we apply a second iteration of corrections. In this work, two stages of corrections for x_1 and AFP resolved the isotopes of interest. From this

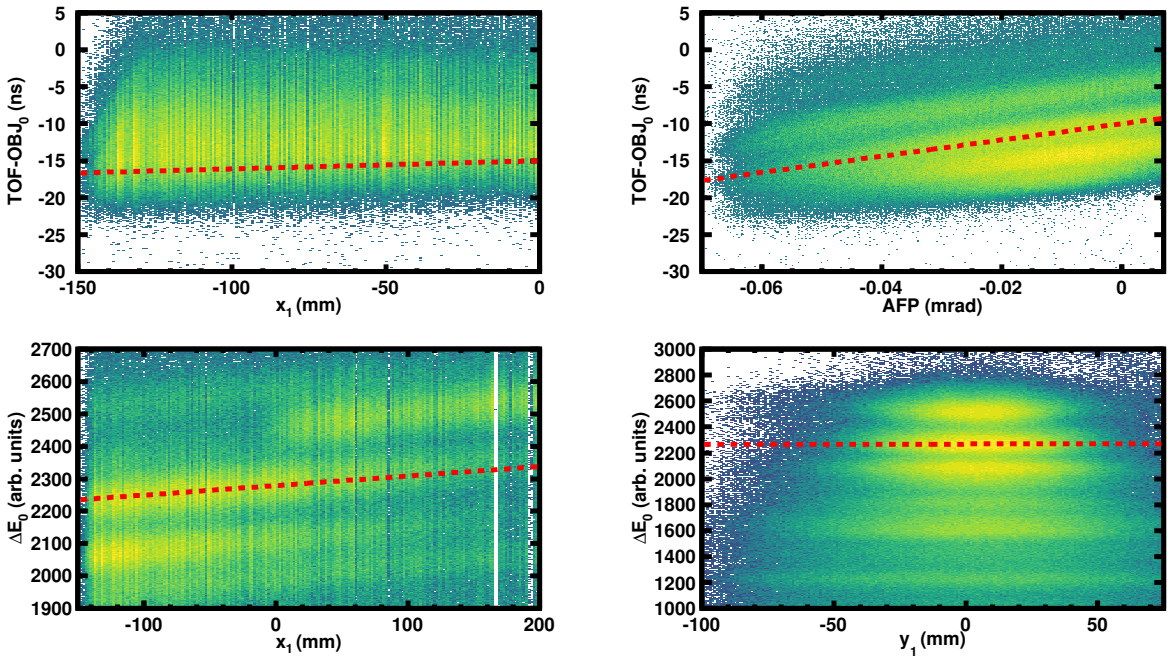

Figure 4.25: (a) TOF-OBJ$_0$ plotted against x_1. (b) TOF-OBJ$_0$ plotted against AFP. (c) ΔE_0 plotted against x_1. (d) ΔE_0 plotted against y_1. Red dotted lines correspond to linear fits.

point forward, we refer to TOF-OBJ$_2$ and ΔE_2 as the corrected TOF and ΔE, respectively.

We performed this correction procedure for each final recoil isotope of interest. Figures 4.26 and 4.27 show the ΔE-TOF PID for the uncorrected and corrected quantities. Different isotopes, each one represented by a "blob", can be clearly resolved in both corrected PID plots. The isotopic resolution will be further improved later in the analysis by gating on emitted deuterons in HiRA. We then look at data in which the S800 blocker was moved slightly in order to let the unreacted beam into the focal plane. Using this data we can unambiguously identify which of the many "blobs" in the PID plot corresponds to the beam species. We can now easily determine the identities of all other blobs, including the heavy recoils ^{33}Ar and ^{45}Ar (indicated in Figures 4.26 and 4.27 by red circles). Gates around these heavy recoils allow us to narrow our analysis to the (p, d) reactions of interest.

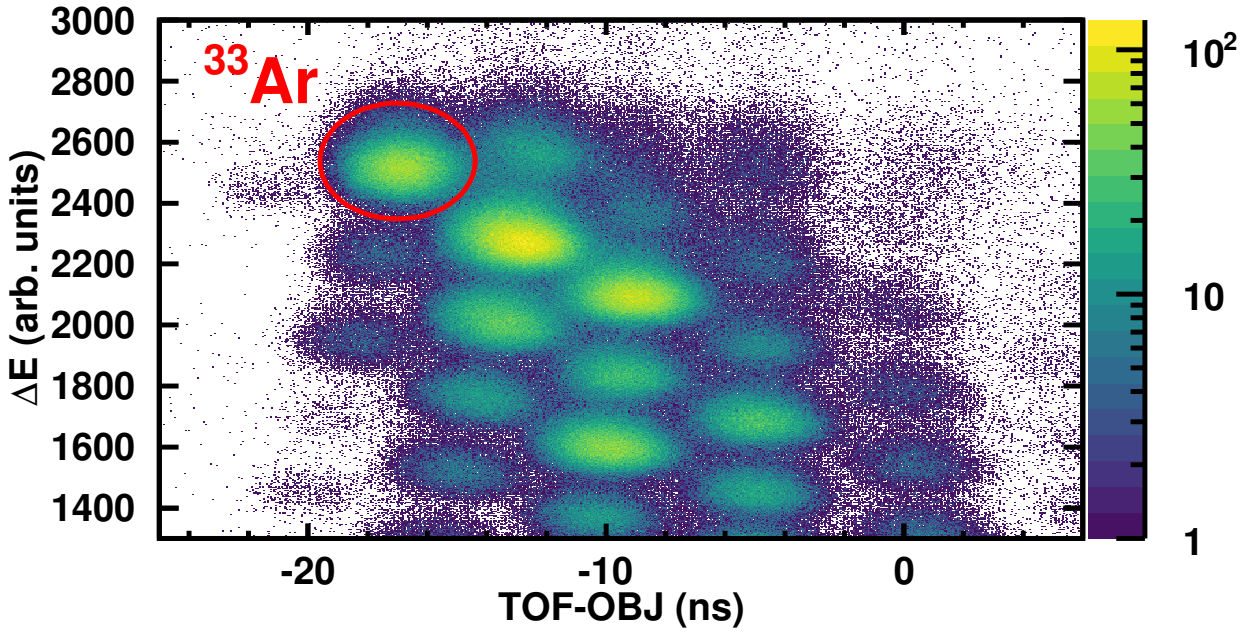

Figure 4.26: S800 PID for the ^{34}Ar beam, with the (p, d) residue ^{33}Ar clearly indicated.

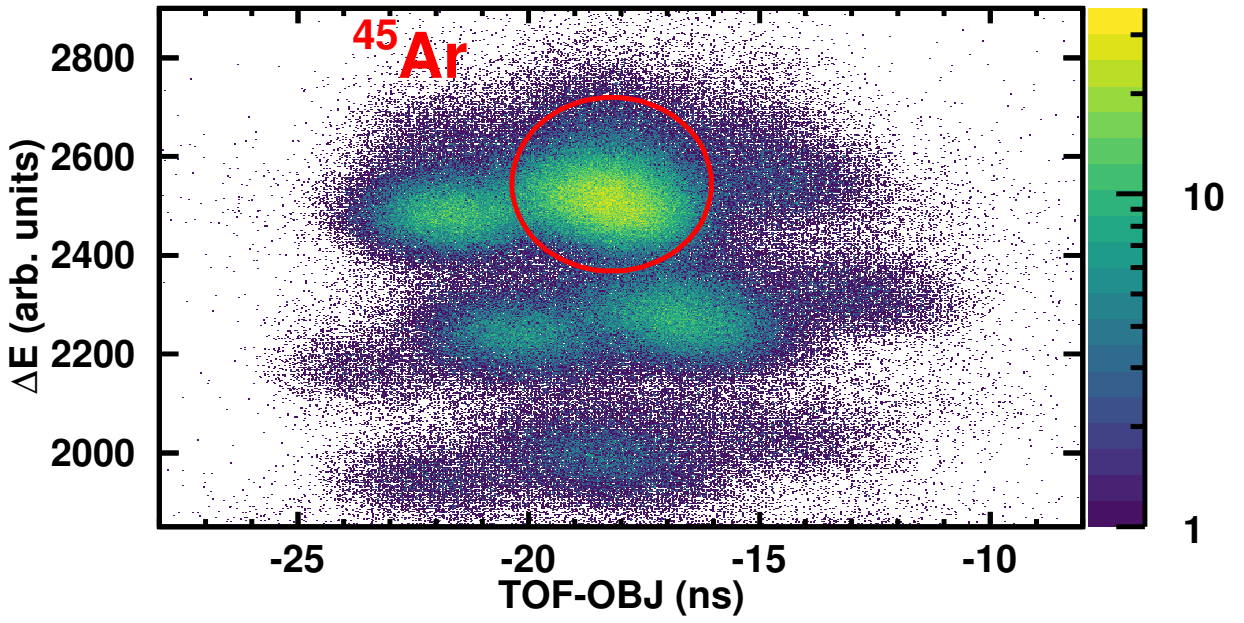

Figure 4.27: S800 PID for the ^{46}Ar beam, with the (p, d) residue ^{45}Ar clearly indicated.

4.3 MCP Beam Tracking

Two Microchannel Plate setups (MCPs) detect the beam upstream of the reaction target. Each MCP setup has two individual Microchannel Plate detectors, each of which is a 0.5-mm-thick array of tiny glass tubes coated with a conductive surface. Each tube acts as an electron amplifier. The two detectors, arranged in the chevron stack configuration shown in Figure 3.12, sit near the beamline and detect secondary electrons from the beam impinging on a layer of aluminized Mylar. One MCP sits about one meter upstream from the target position, and the other is about 10 cm upstream. Section 3.5 features a more detailed technical description of the MCPs.

We used MCPs in this experiment for two reasons. First, the MCPs count the number of incoming beam particles, therefore giving us the incident flux necessary to calculate the transfer reaction differential cross sections. Secondly, the position sensitivity of the MCPs allows for tracking of the beam and subsequently the localization of the reaction on target. This provides a valuable boost in angular and energy resolution. We describe analysis relevant to the latter objective below, and leave the discussion of beam normalization to Chapter 5.

Each anode has four corner signals, and the amplitude of each signal is inversely proportional to the distance between the corner and the location on the anode where electrons are deposited. The signal amplitude will be higher if the deposition is closer to that corner, and conversely the amplitude will be lower if the deposition is farther away. We then can reconstruct the deposition location (and therefore the beam position on the aluminized Mylar foil) using these corner signals. Once we have the beam position at each MCP setup, we can trivially project to the target position.

Using the charge-division method [130], we can calculate raw x and y positions using the upper left (UL), lower left (LL), upper right (UR), and lower right (LR) corner signals:

$$\begin{aligned} x_{\text{raw}} &= \frac{(UL + LL) - (UR - LR)}{UL + LL + UR + LR} \\ y_{\text{raw}} &= \frac{(UL - LL) + (UR - LR)}{UL + LL + UR + LR} \end{aligned} \tag{4.6}$$

With a proper calibration, we can associate x_{raw} and y_{raw} with real physical coordinates for tracking the beam as it travels towards the target.

As discussed in Section 3.5, we recorded a low-gain and a high-gain version of each corner signal. Due to complications with the high-gain signals as well as the reasonably good efficiency of the low-gain signals, we only use the low-gain signals in this analysis. All subsequent discussion of the corner signals refer to the low-gain signals.

Before we can sensibly combine the corner signals as described in Equation 4.6, we must ensure that these signals are on the same (albeit uncalibrated) scale. Although all corners undergo the same amount of amplification, they do not have the same *pedestal* values. The pedestal is the mean value of the signal when no beam is present. We determined this pedestal by taking data with no beam in the vault. Then, we can subtract from each corner signal the corresponding pedestal so that they all have the same zero offset, as shown in Figure 4.28. Now that all MCP corner signals have value equal to 0 when there is no incoming signal, we can combine the corners to produce meaningful position information.

Beam tracking is not available for the ^{34}Ar data due to a misconfigured electronics fast clear circuit. We discovered this problem during the experiment and fixed it in time for the ^{46}Ar beam, so below we discuss the beam spot reconstruction for this system. During the ^{34}Ar beam tuning, we estimated the size of the beam spot to be roughly 50 mm^2, which is

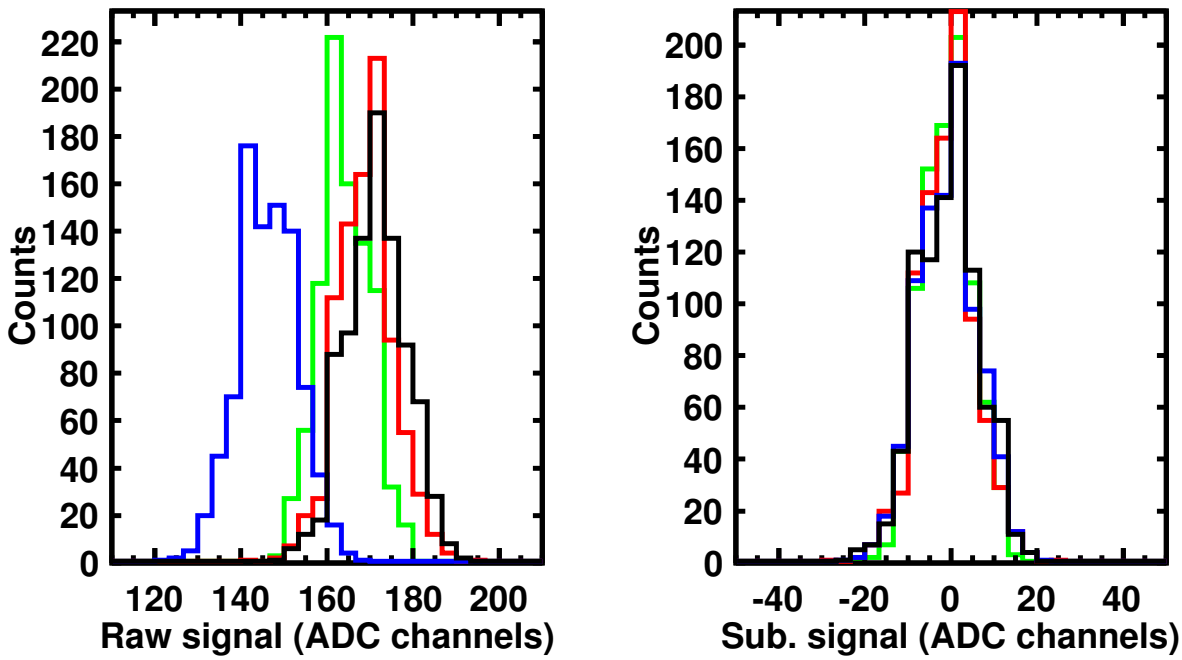

Figure 4.28: MCP1 raw corner signals (left), and MCP1 pedestal-subtracted corner signals (right).

much smaller than the size of the ^{46}Ar beam spot. So, fortunately, beam tracking is not as critical for the ^{34}Ar beam.

4.3.1 Mask Calibration

In order to measure the mapping from raw position calculated with charge division to calibrated position corresponding to a particular location relative to the beam axis, we inserted brass masks with well-defined hole patterns (shown in Figure 4.29) in front of the aluminized Mylar foils for several data runs. These masks feature asymmetric hole patterns to unambiguously tell their orientation relative to the beam axis. Although the brass masks do not stop the beam from going through, they do change the rigidity of the beam. Therefore, the S800 deflects any beam particles that passed through either mask such that they do not pass through the focal-plane box, and do not trigger the DAQ. We measured the exact positions

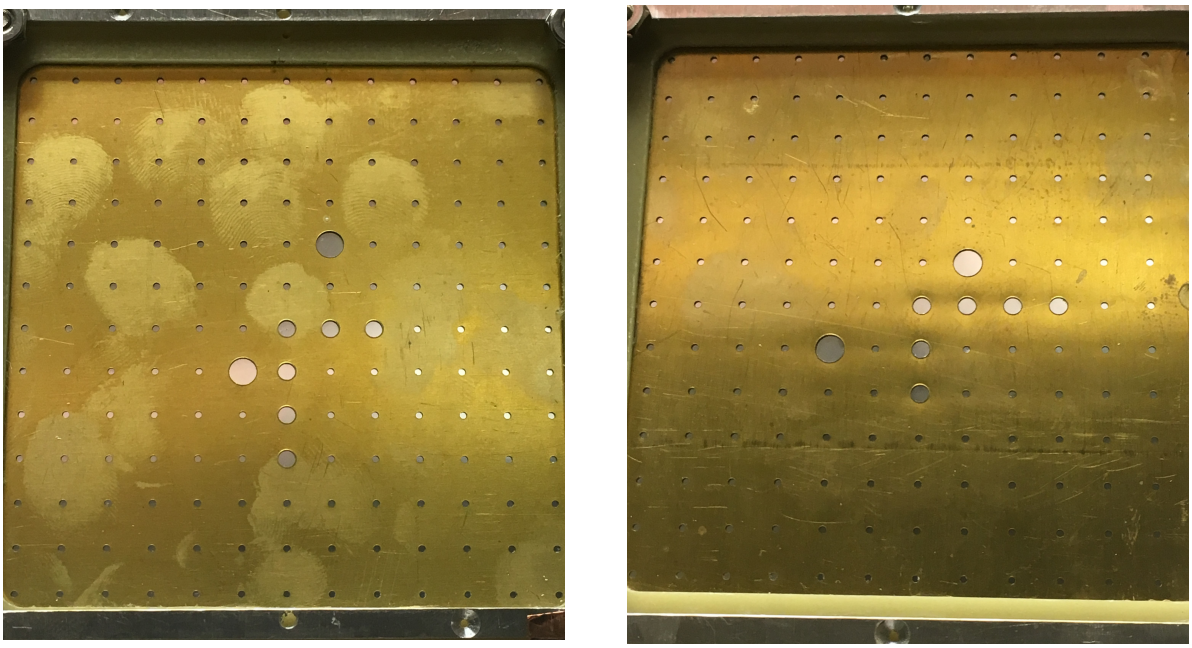

Figure 4.29: MCP brass calibration masks for MCP0 (left) and MCP1 (right). The holes in the mask pattern are 1, 2, or 3 mm in diameter.

of the masks in the laboratory frame using the ROMER arm described in Section 3.6. We can reconstruct the mask pattern with the MCP data to make a calibration. Once we have this mapping, we can use it to calculate the position of the beam in the transfer reaction data.

Since we know the exact locations of the holes in the mask, we can match the raw x and y values to their appropriate positions with a two-dimensional, third-order polynomial:

$$\begin{aligned} x_{\text{cal}} &= a_0 + a_1 x_{\text{raw}} + a_2 y_{\text{raw}} + a_3 x_{\text{raw}}^2 + a_4 y_{\text{raw}}^2 + a_5 x_{\text{raw}}^3 \\ &\quad + a_6 y_{\text{raw}}^3 + a_7 x_{\text{raw}} y_{\text{raw}} + a_8 x_{\text{raw}}^2 y_{\text{raw}} + a_9 x_{\text{raw}} y_{\text{raw}}^2 \\ y_{\text{cal}} &= b_0 + b_1 y_{\text{raw}} + b_2 x_{\text{raw}} + b_3 y_{\text{raw}}^2 + b_4 x_{\text{raw}}^2 + b_5 y_{\text{raw}}^3 \\ &\quad + b_6 x_{\text{raw}}^3 + b_7 y_{\text{raw}} x_{\text{raw}} + b_8 y_{\text{raw}}^2 x_{\text{raw}} + b_9 y_{\text{raw}} x_{\text{raw}}^2 \end{aligned} \tag{4.7}$$

The calibrated masks are shown in Figure 4.30. All of the holes are within 1 millimeter

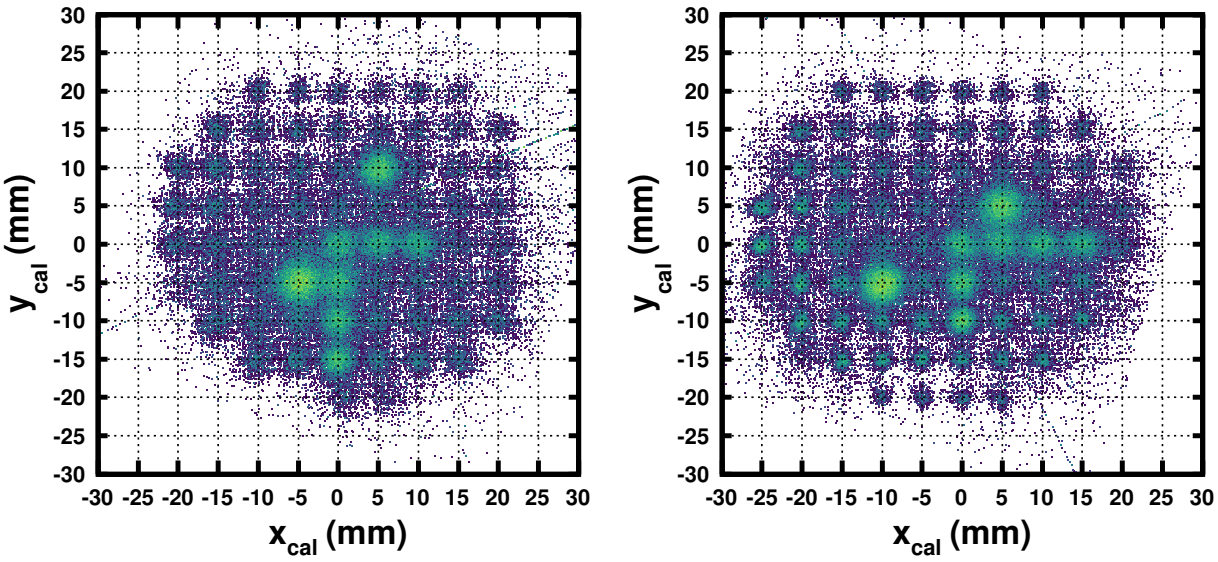

Figure 4.30: MCP0 x_{cal} vs. y_{cal} calibrated mask data (left) and MCP1 x_{cal} vs. y_{cal} calibrated mask data (right).

of the expected mask position. To determine the position resolution of each MCP, we select holes of different sizes near the center of the detector (where the beam is likely to be concentrated). Then we perform a Gaussian fit for the vertical and horizontal projections for each hole. Table 4.1 lists the widths of a sample hole peak in both the vertical (y) and horizontal (x) directions for holes of the three different sizes, as well as the intrinsic position resolutions for both MCPs found via extrapolation to a hole size of 0 mm. We assume that the resolution is uniform across the entire MCP.

4.3.2 Beam Spot Reconstruction

We now have a mapping from the MCP corner signals to real position on the beamline. Next, we can apply this mapping to the real data for each MCP and then use the resulting MCP0 position and MCP1 position to calculate the position of the beam at the reaction target using simple geometrical considerations. As in [140], we assume that the deflection of

MCP	Hole size (mm)	σ_x (mm)	σ_y (mm)
0	3	1.5	1.6
0	2	1.3	1.5
0	1	1.2	1.3
0	$\rightarrow$0 Intrinsic	1.0	1.2
1	3	1.5	1.5
1	2	1.3	1.2
1	1	1.0	1.0
1	$\rightarrow$0 Intrinsic	0.73	0.77

Table 4.1: MCP position resolutions along both axes for several hole sizes in both MCPs, as well as the intrinsic resolutions found be linearly extrapolating to a 0 mm hole size.

the beam due to the field from the permanent magnets at each MCP is negligible. Figure 4.31 shows the resulting beam spot for the ^{46}Ar beam, which has FWHM of 16 mm in the horizontal direction and 26 mm in the vertical direction.

This beam spot reconstruction gives us an event-by-event determination of the transfer reaction location in the plane of the target for the ^{46}Ar beam. As mentioned above, the MCPs did not function properly for the ^{34}Ar beam, and so we will assume the reaction locus is at the center of the target plane for every event.

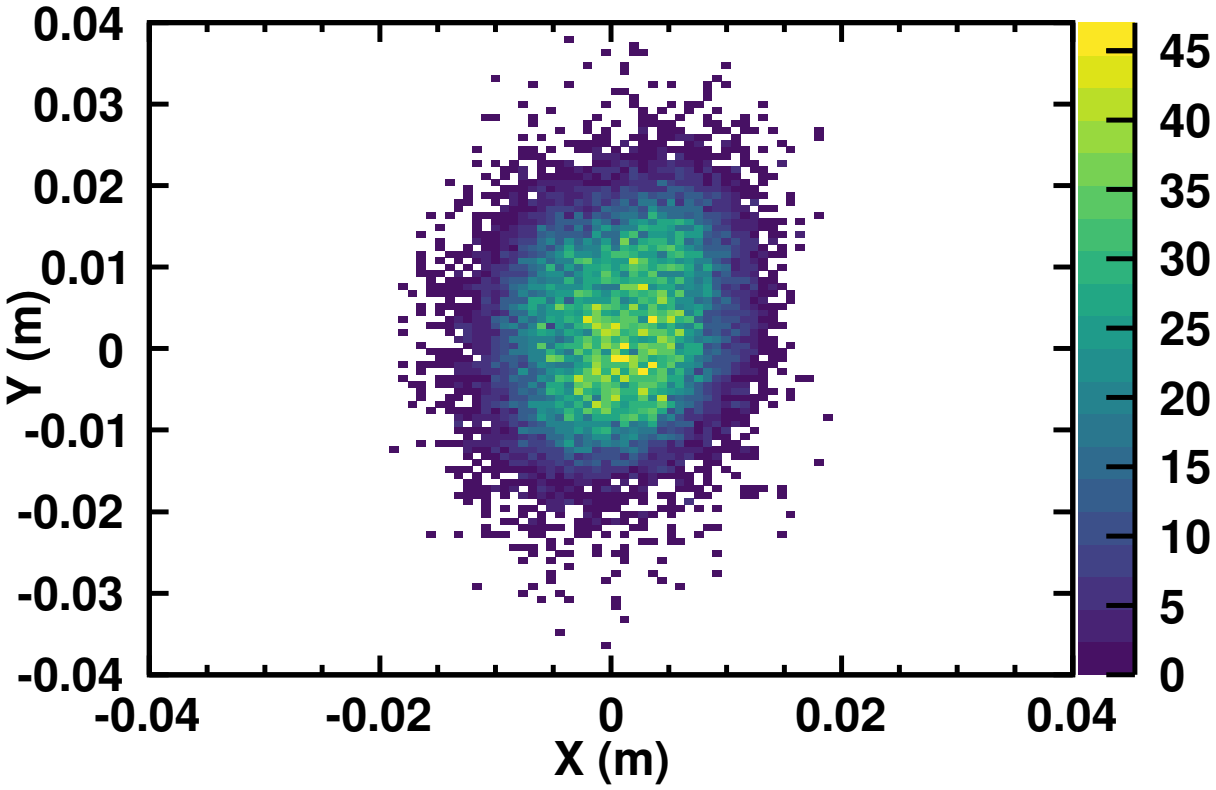

Figure 4.31: Reconstructed beam spot at the target for the ^{46}Ar beam.

Chapter 5

Data Analysis II: Cross Sections and Reduction Factors

> In God we trust, others must provide data.
>
> Edwin R. Fisher

The calibrated and corrected detector data do not by themselves tell us about the transfer reactions of interest: we must perform more analysis to reach our goal. This chapter describes the process of producing differential cross sections from calibrated HiRA, S800, and MCP data.

We first merge the data via an *event generation* procedure in which data from separate detectors are assembled into a single transfer reaction event. For each beam, we isolate the (p, d) transfer reactions by gating on the incoming beam PID, on the appropriate recoil in the S800 PID, and on deuterons in HiRA. We also gate on the appropriate pixel codes (see Section 4.1.6) in HiRA, and we discard HiRA strips (or, in a few cases, entire detectors[1]) that are not working properly. In the case of the ^{46}Ar beam, we gather beam tracking information from the MCPs. This merged event data is then written to a ROOT Tree, allowing for direct study of the (p, d) transfer reactions.

Once we have gated on the (p, d) reaction channel, we calculate the reaction kinematics

[1] For instance, two telescopes had EB detectors that did not function correctly. This made pixelation impossible, so the data from these telescopes was discarded.

as well as the recoil excitation energy. For the ^{46}Ar beam, we can also include MCP beam tracking to boost the deuteron energy resolution. We then generate angular distributions by fitting peaks in the excitation energy spectra. Next, we normalize these angular distributions with the incoming number of beam particles as well as corrections for detector performance and geometry. This process yields the differential cross sections of interest. We use these cross sections in combination with ADWA calculations to extract spectroscopic factors for (p, d) reactions to different final states in the heavy argon recoil. Finally, we compare the extracted SFs to shell model calculations to calculate reduction factors and study their asymmetry dependence.

We note that the term "normalization" is used in two separate ways in this chapter. First, we discuss normalization of angular distributions to produce our observable of interest, differential cross sections. Later in the chapter, normalization refers to the comparison of differential cross sections to ADWA reaction calculations in order to extract spectroscopic factors. To avoid confusion, we advise the reader to consider the context in which this term is used throughout the chapter.

5.1 Reaction Kinematics

After event generation, we examine the two-body kinematic relationship between the emitted deuteron angle and its energy as detected in HiRA. This relationship does not depend on any advanced underlying physics, and we can calculate it via simple conservation laws. Furthermore, as depicted in Figure 3.2, the kinematics are sensitive to the final state of the heavy recoil. Figures 5.1 and 5.2 show the kinematics data for each reaction system along with several calculated kinematic lines corresponding to different final states in the argon

recoil. Table 5.1 shows the energy levels for both ^{33}Ar and ^{45}Ar below 5 MeV. The states listed in bold are represented with kinematic lines in Figures 5.1 and 5.2. Although in most cases the measured kinematics agreed with the calculated lines, for some telescopes (despite our best efforts in calibration) we had to shift the measured energy in order to better match the expected kinematics. These shifts were on the order of 100 keV for particles in the silicon and 1 MeV for particles in the CsI. Because the goal of this experiment is measuring cross sections involving known states rather than characterizing new states, these energy shifts are inconsequential to our measurement.

In both reaction systems, resolution worsens going from forward to backward angles. This is due to the higher energy particles at backward angles punching into the CsI crystals, which have inherently worse resolution than the E silicon detectors. Kinematic broadening further exacerbates this effect. This issue can at least partially be mitigated using the improved angular resolution via the MCP beam tracking system. As mentioned in Chapter 4, the MCPs did not function properly during the ^{34}Ar beam run. In that case, we are largely concerned with the forward-angle peak corresponding to the ^{33}Ar ground state. Fortunately this peak is almost entirely detected in the silicon detectors at forward angles, so the inferior resolution at backward angles is not a major obstacle. Furthermore, the beam spot for the ^{34}Ar was rather small (50 mm^2), as pointed out in Chapter 4.

5.2 Excitation Energy

So far, this analysis has taken place entirely in the reference frame of the laboratory. By transforming to the center-of-mass (COM) frame, we can reconstruct the excitation energy of the heavy argon recoil left behind after the (p, d) transfer reaction. We use the fact that

^{33}Ar		^{45}Ar	
Energy (MeV)	J^π	Energy (MeV)	J^π
0	$1/2^+$	**0**	$5/2^-, 7/2^-$
1.359	$3/2^+$	0.542	$1/2^-, 3/2^-$
1.798	$5/2^+$	1.340	
2.439	$3/2^+$	1.416	$1/2^-, 3/2^-$
3.154	$3/2^+$	1.660	
3.361	$5/2^+$	**1.734**	
3.456	$7/2^+$	**1.770**	
3.819	$5/2^+$	1.876	$1/2^-, 3/2^-$
		1.911	
		2.420	
		2.510	$1/2^-, 3/2^-$
		2.757	
		3.230	
		3.295	
		3.718	
		3.950	
		4.280	
		4.326	
		4.800	

Table 5.1: Energy levels below 5 MeV as well as known spin and parity assignments for ^{33}Ar and ^{45}Ar.

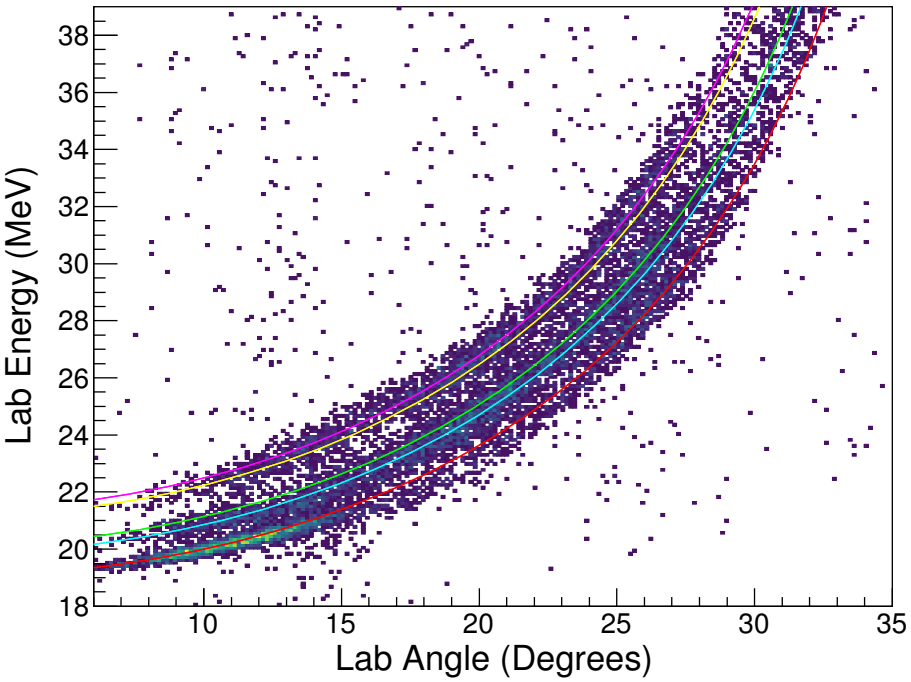

Figure 5.1: Measured kinematic curves for $^{34}\mathrm{Ar}(p,d)^{33}\mathrm{Ar}$ shown with calculations for comparison.

the kinematics of the deuteron detected in HiRA tells us the final state of the argon recoil, as discussed in Section 5.1. So, we can use HiRA to identify the final state of the heavy Ar recoil, and generate differential cross sections to individual final states.

We first must calculate the reaction *Q-value*, or the amount of energy released in the reaction. Conceptually, the Q-value is simply the difference between the initial and final kinetic energies of the system. Via mass-energy equivalence, we define the Q-value for the reaction $A(p,d)B$ as:

$$Q = m_A + m_p - m_d - m_B^* \tag{5.1}$$

where m_A, m_p, m_d, and m_B^* are the rest masses of the beam particle, the proton, the deuteron, and the heavy recoil. The superscript on m_B^* denotes that B can have non-zero excitation energy, and that we include this in the rest mass. Both the proton and deuteron

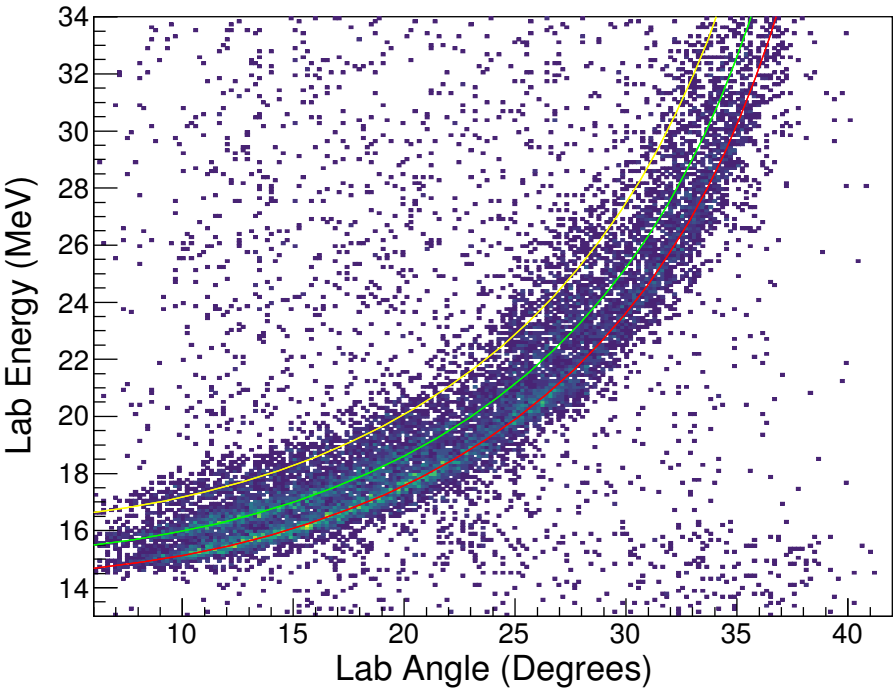

Figure 5.2: Measured kinematic curves for $^{46}\mathrm{Ar}(p,d)^{45}\mathrm{Ar}$ shown with calculations for comparison.

have no particle-bound excited states, and we assume that the incoming projectile is in the ground state. All of the ground-state rest masses of particles measured in this experiment are known, so m_B^* is the only variable quantity in Equation 5.1: once we have m_B^*, we immediately have the Q-value.

We determine m_B^* by first performing a Lorentz transformation (using the beam momentum) to determine the deuteron kinetic energy in the COM frame (t_d^{COM}). Because this transformation has no effect on momentum vectors perpendicular to the beam momentum, the relationship between t_d^{COM} and the kinetic energy in the lab depends on both the deuteron energy as well as its angle. Applying conservation of energy and momentum, we

derive a relation between t_d^{COM} and m_B^*:

$$(m_B^*)^2 = (M - m_d)^2 - 2Mt_d^{\mathrm{COM}} \tag{5.2}$$

where M is the invariant mass of the system which we calculate using the beam energy, the beam rest mass, and the target rest mass. Now, we have a complete prescription for calculating the Q-value event-by-event starting from the deuteron energy and angle in the laboratory frame.

We can easily calculate the expected Q-value for the ground state using masses from literature tabulations like [134]. Therefore, we can compute the excitation energy of B for a given event by simply subtracting the Q-value for the event from the known ground-state Q-value. Once we have the event-by-event excitation energy, we can generate excitation energy spectra to unambiguously identify final states in the heavy Ar recoil.

Figures 5.3 and 5.4 show excitation energy spectra for ^{33}Ar and ^{45}Ar (respectively). Fig. 5.3 depicts excitation energies for ^{33}Ar at forward angles (the approximate angular range of the main peak of interest) in the center-of-mass frame. We see a prominent peak at 0 MeV with a standard deviation of about 240 keV, which agrees with the expected resolution from simulation. As shown in Table 5.1, the lowest lying excited state of ^{33}Ar is at 1.359 MeV, so we are confident that the 0 MeV peak is well-separated from any excited state contributions. For the $^{46}\mathrm{Ar}(p,d)^{45}\mathrm{Ar}$ case, each panel of Figure 5.4 shows excitation energy spectra calculated both with (red) and without (black) MCP beam tracking for a given angular range. On the left panel (forward angles), we see a peak at 0 MeV, but cannot separate the ground state of ^{45}Ar from the first excited state at 0.542 MeV. In any case, the peak at 0 MeV is distinguishable from higher-lying peaks. The right panel, corresponding to

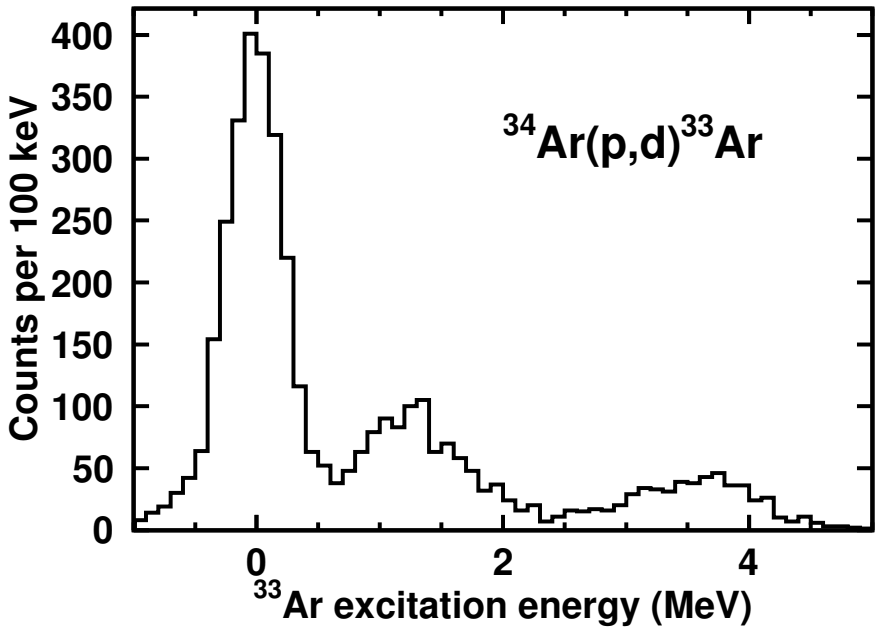

Figure 5.3: Measured $^{34}\mathrm{Ar}(p,d)^{33}\mathrm{Ar}$ excitation energy spectrum for $\theta_{\mathrm{COM}} < 10$ degrees.

more backward angles and worse experimental resolution, shows the 0 MeV peak with a long tail at higher excitation. We note that the spectra calculated without MCP beam tracking (in black) are scaled down for comparison to spectra that did use the MCP beam tracking. This is necessary because of the imperfect efficiency of the MCP beam tracking system.

Figure 5.4 also depicts the excitation energy both with and without MCP beam tracking in the angle determination. At forward angles (left panel) the excitation energy resolution for the ground state of ^{45}Ar is similar with and without beam tracking, but for backwards angles (right panel) the MCP beam tracking provides a boost in resolution. Fig 5.5 shows explicitly the improvement of MCP beam tracking for large angles.

To generate angular distributions, we gate the excitation energy on several angular slices in the center of mass. We then fit these spectra with a sum of several Gaussian functions, each one corresponding to a separate peak in a given reaction system. All peaks are fit simultaneously to account for overlap between different peaks. Integrating these Gaussian

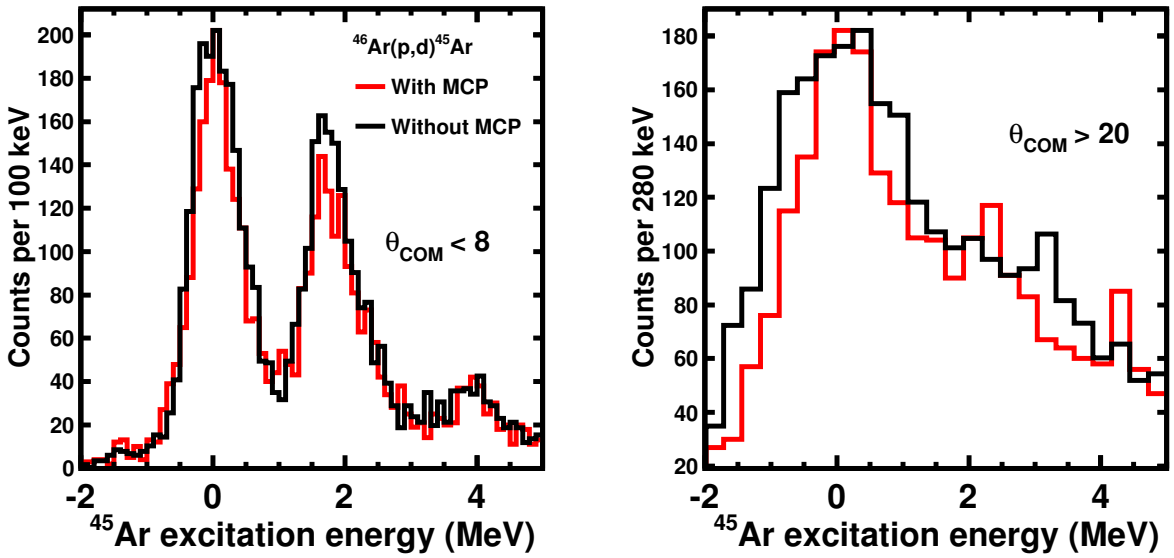

Figure 5.4: Measured $^{46}\mathrm{Ar}(p,d)^{45}\mathrm{Ar}$ excitation energy spectra for several different angular ranges. We show the excitation energies calculated without MCP beam tracking (black) and with MCP beam tracking (red).

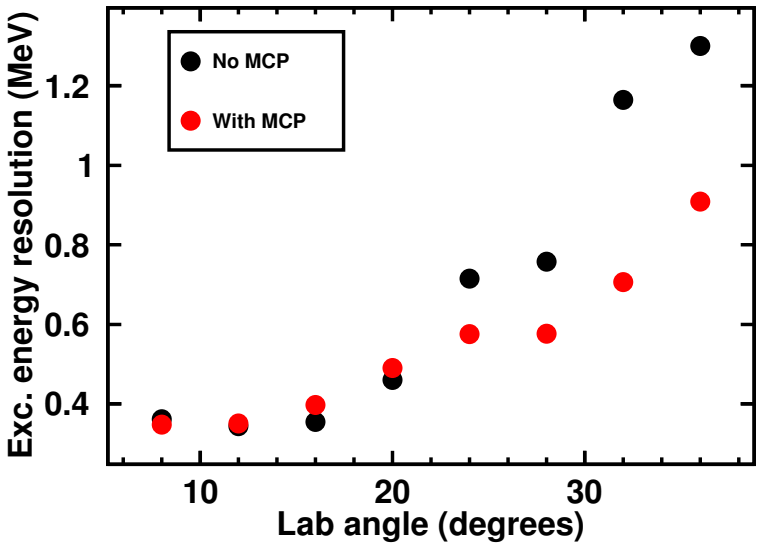

Figure 5.5: Widths of the Gaussian fits for $^{46}\mathrm{Ar}(p,d)^{45}\mathrm{Ar}_{\mathrm{g.s.}}$. The black (red) points correspond to data without (with) MCP beam tracking..

functions yields the number of counts for each peak, which corresponds to the number of deuterons emitted from transfer reactions where the argon recoil occupied one (or more) particular state(s).

Because the ground state peak in the ^{33}Ar excitation spectra is relatively well separated, the fitting is straightforward. The ^{45}Ar case is slightly more complicated. At backward angles, the ^{45}Ar 0 MeV peak blends into a smooth spectrum without distinguishable peaks at higher excitation (as in the right panel of Figure 5.4). To address this problem, we fit the uncontaminated lower-energy half of the 0 MeV peak to get the Gaussian function. At forward angles, we expect to see some contribution in the 0-MeV peak from the $l = 1$ first excited state in ^{45}Ar at 542 keV. Unfortunately we are unable to resolve these two peaks cleanly. However we can see a distortion in the 0-MeV peak which indicates the presence of the unresolved first-excited-state peak, as shown in the left panel of Figure 5.4. We deal with this issue by fitting the 0 MeV peak with two Gaussian functions in order to constrain the excited state contribution to the cross section. We also use the angular distribution at more backward angles (where the cross section for the excited state drops significantly) to check these results. Section 5.5 features more details about the excitation energy fits.

Now, our goal is to produce differential cross sections by normalizing the angular distributions to account for detector performance and beam purity. Before taking this step, we consider the possibility of non-(p, d) contamination of our spectra from background.

5.3 Background Subtraction

Because the reaction target we used in this measurement is polyethylene, it is possible that some of our deuteron and heavy recoil coincidences are due to non-transfer reactions on

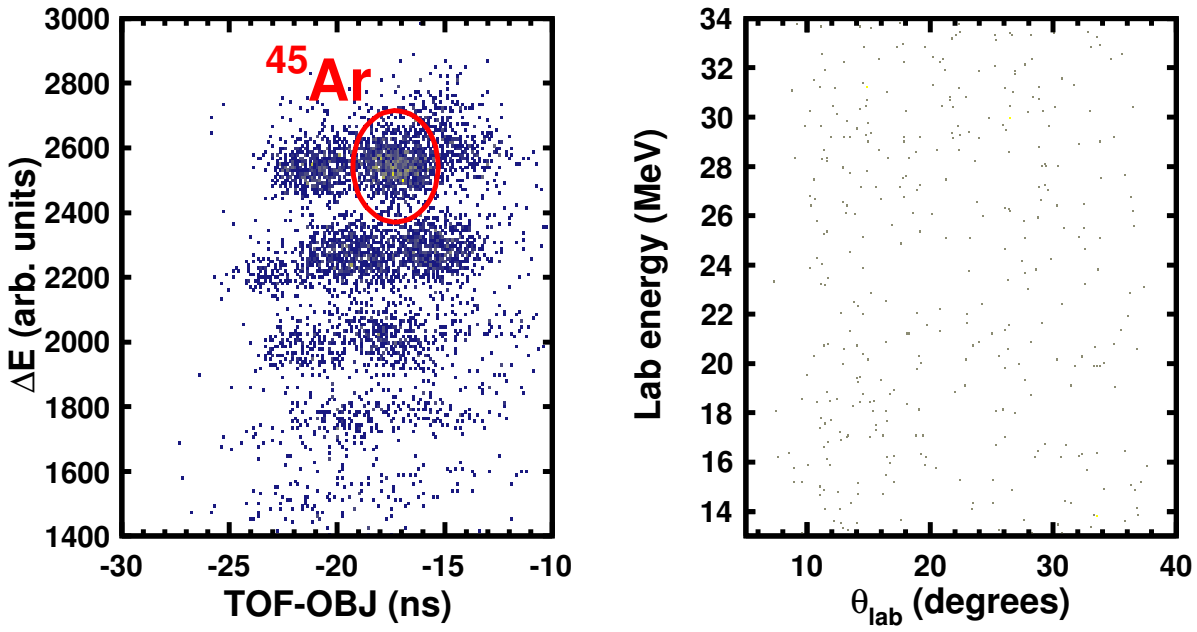

Figure 5.6: S800 PID (left) and deuteron kinematics (right) for the carbon target runs with the ^{46}Ar beam. The kinematics plot is gated on the ^{45}Ar residue indicated in the S800 PID plot.

carbon nuclei. To address contributions from reactions on carbon, we used a 17 mg/cm^2 C target to evaluate the background. This target is substantially thicker than our reaction targets, so any carbon-induced reactions potentially coming from the reaction target should be plainly visible using the thick C target.

Figure 5.6 shows the S800 PID spectrum for the C target data runs, as well as the deuteron kinematics for these runs gated on the ^{45}Ar residue. The number of background counts in the kinematics plot is negligible compared to the statistics measured with the polyethylene reaction target. The same is true for the case of the ^{34}Ar beam on C target runs. Therefore, a background subtraction is not necessary.

5.4 Normalization

The results of our analysis to this point consist of detected deuterons with known angle and energy that have been emitted from (p, d) transfer reactions for two separate beams. In order to produce our desired differential cross sections, we must account for the efficiency of our experimental setup and also the number of argon-hydrogen beam-target interactions. This process is called *normalization*, and we discuss it in detail for both beams in the following section. First, we quickly introduce the general plan for normalization, and then delve into the various necessary corrections.

For the (p, d) transfer reactions measured here, the differential cross section is given by:

$$\left(\frac{d\sigma}{d\Omega}\right)_{\theta_i} = \frac{N_d(\theta_i)}{N_{\text{target}} N_{\text{beam}}} \tag{5.3}$$

where θ_i is the i^{th} angular bin, N_{target} is number of hydrogen nuclei per square centimeter in the polyethylene reaction target, N_{beam} is the total number of beam particles that impacted the target, and $N_d(\theta_i)$ is the number of deuterons emitted from the reaction in θ_i.

N_{target} is fixed throughout the experiment for a given target thickness. We calculate N_{beam} with the following relation:

$$N_{\text{beam}} = \eta \frac{N_{\text{beam}}^{\text{Det}}}{\varepsilon_{\text{MCP}}} \tag{5.4}$$

where $N_{\text{beam}}^{\text{Det}}$ is the number of beam particles counted by the MCP1 scaler, η is the purity of the beam, and ε_{MCP} is the MCP1 scaler efficiency.

To get $N_d(\theta_i)$, we count the number of deuterons detected within the given angular bin

θ_i and then adjust for detector efficiencies in the following way:

$$N_d(\theta_i) = \frac{N_d^{\mathrm{Det}}(\theta_i)/\varepsilon_{\mathrm{HiRA}}(\theta_i)}{\varepsilon_{\mathrm{DAQ}}\varepsilon_{\mathrm{OBJ}}\varepsilon_{\mathrm{MCPTrack}}} \tag{5.5}$$

where $N_d^{\mathrm{Det}}(\theta_i)$ is the number of deuterons detected in our experimental setup at the angular bin θ_i, and $\varepsilon_{\mathrm{HiRA}}(\theta_i)$ is the angle-dependant efficiency of HiRA detecting a deuteron in θ_i (and includes the solid angle subtended by θ_i). The terms in the denominator are overall efficiency corrections: $\varepsilon_{\mathrm{DAQ}}$ is the live time of the data acquisition (DAQ) system, $\varepsilon_{\mathrm{OBJ}}$ is the efficiency of the OBJ scintillator used for beam and S800 particle identification, and $\varepsilon_{\mathrm{MCPTrack}}$ is the overall efficiency of the MCP beam tracking system[2].

We first will calculate the assorted efficiency corrections needed to determine $N_d(\theta_i)$ and N_{beam}. Then we will use Equation 5.3 to compute differential cross sections.

5.4.1 DAQ Live Time

Recording an event with the DAQ takes a nonzero amount of time. If another event arrives while the previous event is being processed, this new event is lost completely. The fraction of time that the DAQ is available to record data is called the *live time* (the fraction of time the DAQ is not available for data taking is fittingly called the *dead time*). Because transfer reaction events can occur during the DAQ dead time, we use the live time ($\varepsilon_{\mathrm{DAQ}}$) as a correction factor in Equation 5.5.

During the experiment a scaler module counted logic signals for a variety of electronics circuits, which allows us to track how much those circuits are firing. For example, we recorded the scaler rates of the OBJ and HiRA detectors. We can split a logic signal coming from

[2]This quantity is distinct from $\varepsilon_{\mathrm{MCP}}$, the scaler efficiency of the MCP which comes from the MCP time signal.

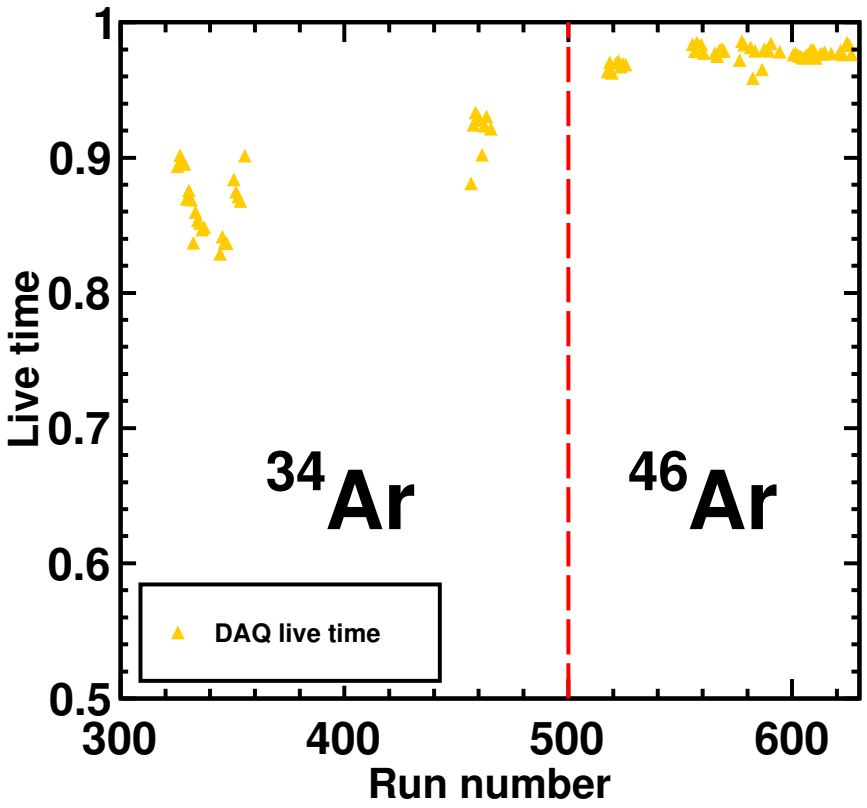

Figure 5.7: Live time of the DAQ system plotted against run number.

the detector, sending one side directly into the scaler module as the *raw* scaler. We block the other side with the overall DAQ trigger before sending it to the scaler module as the *live* scaler. In other words, the live scaler only fires when (a) there is a logic pulse in the corresponding raw scaler and (b) the DAQ is available for recording data. The ratio of the live scaler to the raw scaler is a measure of the total DAQ live time.

In this analysis, we use the HiRA scaler to compute the live time. Figure 5.7 shows the live-to-raw scaler ratio for the HiRA trigger plotted against the run number. On average, the live time is 98.3% for the ^{46}Ar beam, and 88.1% for the ^{34}Ar beam.

5.4.2 HiRA Efficiency

HiRA does not have perfect angular coverage, and therefore deuterons emitted at an angle not covered by HiRA are not detected. To correct for this, we simulated the geometrical acceptance of HiRA using the NPTool Monte Carlo simulation package (as described in Section 3.3.3). The outcome of this simulation is $\varepsilon_{\mathrm{HiRA}}(\theta_i)$, the fraction of deuterons emitted within the θ_i angular bin that are detected in HiRA. NPTool allows us to easily remove individual faulty detector elements (e.g. missing silicon strips or poorly biased detectors) from the Monte Carlo calculations to fold these effects into the resulting efficiency. Accounting for the variable electronics dead time across the array requires a more subtle approach.

Individual noisy strips in the silicon can clog up the fast clear circuits in the HiRA ASIC electronics, resulting in a high electronics dead time[3]. This problem is notably pronounced in the thin, high-capacitance DE detectors. We measured this electronics dead time during the experiment by pulsing the silicon detectors at a fixed frequency and an energy far above what was relevant for the transfer reaction deuterons. By comparing the number of measured pulses in each silicon strip to the total number of expected pulses (found by multiplying the known pulser frequency by the total run-time), we can extract the electronics dead time for individual strips. Figure 5.8 shows that the electronics dead time varied not only from detector to detector but also within individual detectors. This is due to each detector having two ASIC chips (with each chip responsible for 16 channels) that can have different amounts of noise.

We include the effects of individual-strip electronics dead times into the Monte Carlo simulation via an extra step of random sampling for each event. We see a pronounced effect

[3]Note that here we mean the dead time of just the HiRA electronics system, not the overall DAQ dead time discussed in Section 5.4.1.

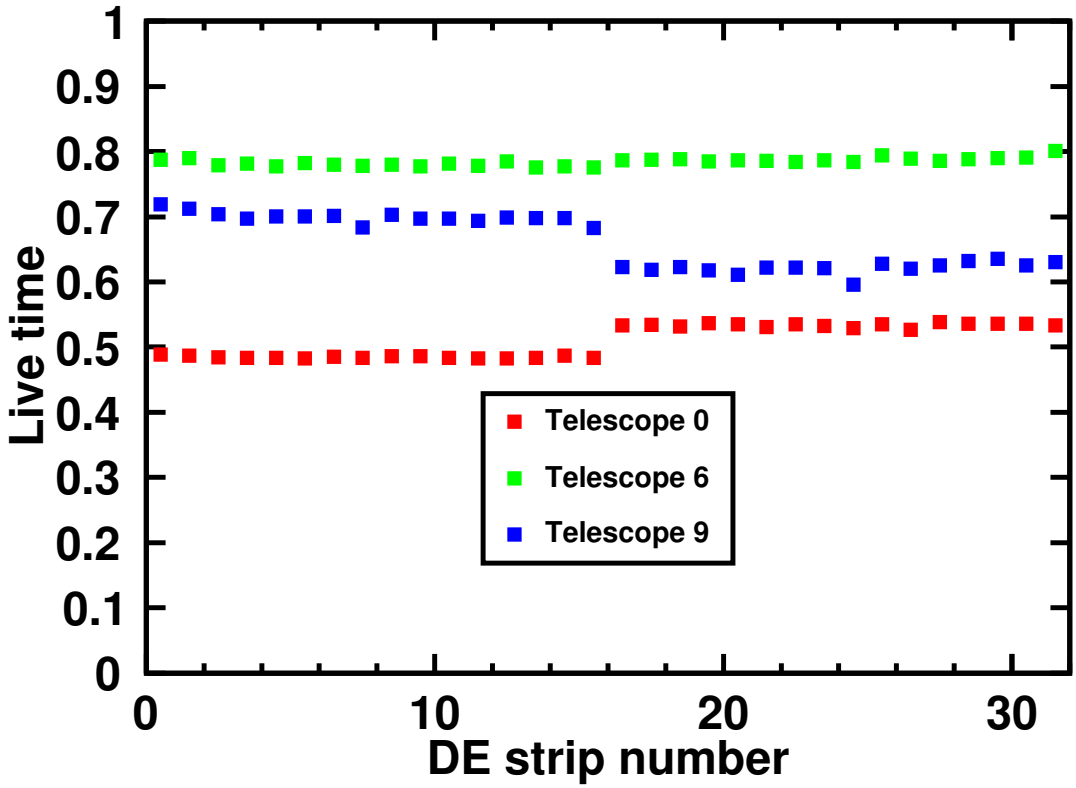

Figure 5.8: Strip-by-strip electronics live times for three example HiRA DE detectors. We see variation from detector to detector, as well as within individual detectors.

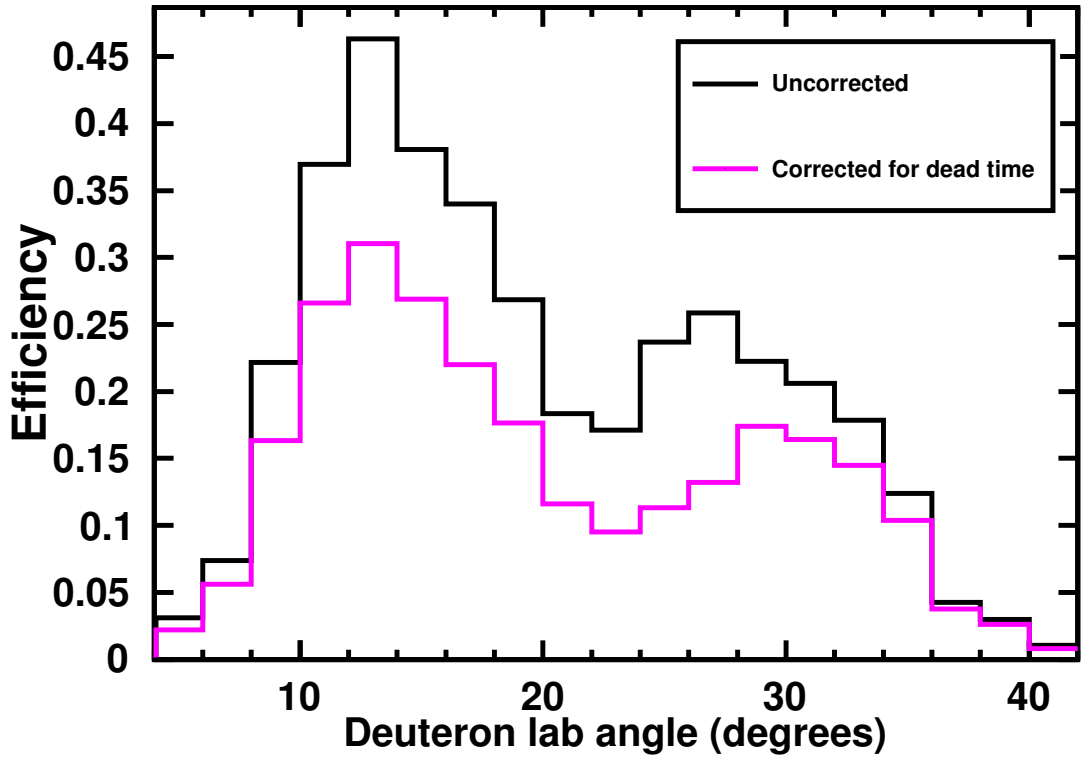

Figure 5.9: HiRA geometrical efficiency for ^{46}Ar(p, d) without (black) and with (pink) dead time corrections as described in the text.

on the final geometrical efficiency, in particular at forward angles below the E punch through energy. Figure 5.9 shows the efficiency dependence on laboratory angle from simulations with and without the dead time corrections.

5.4.3 Beam Detector Efficiencies

Several important detectors lay directly in the path of the incoming beam: the OBJ scintillator upstream from the S800 (which identifies the incoming beam and the heavy recoil), and the MCPs (which count the number of incoming beam particles, and also track the beam trajectory). These detectors are not perfectly efficient due to the sustained high beam rate. Clearly, we require these detector efficiencies in order to properly normalize the data.

We first assume that both the RF signal the E1 scintillator in the S800 are 100% efficient. The RF signal is trivially 100% efficient, and the E1 assumption is grounded in the fact that due to the presence of the blocker in the S800, the rate of particles hitting the E1 scintillator is multiple orders of magnitude below the full beam rate. Then, we gate either the RF or E1 time on the corresponding beam detector signal (OBJ, MCP time, or MCP position signals). The relative presence of any of these detectors when compared to the RF or E1 gives a measure of the corresponding detector efficiency.

5.4.3.1 OBJ

We monitored the OBJ scintillator efficiency during the course of the experiment to track performance deterioration related to radiation damage. If necessary, we raised the scintillator voltage or adjusted the scintillator position so that the beam was focused on a different spot. Figure 5.10 shows the ungated and gated RF time spectra for the OBJ.

Figure 5.11 depicts the OBJ efficiency over the course of the experiment. For the total normalization, we use the efficiency values that result from combining data from all runs. For the ^{34}Ar beam, this efficiency is 90.1%, and for the ^{46}Ar beam it is 78.7%.

5.4.3.2 MCP Time

The MCP scalers (triggered by the MCP TDC signals) count the number of particles that impinge upon each MCP. The TDC signal from each MCP triggers the MCP scaler circuits. Therefore, the efficiency of the MCP scalers are given by the respective efficiencies of the MCP timing signals. We are especially concerned with the MCP1 scaler because of its proximity to the target, but we also measure MCP0 as a consistency check (as discussed further in Section 5.4.5).

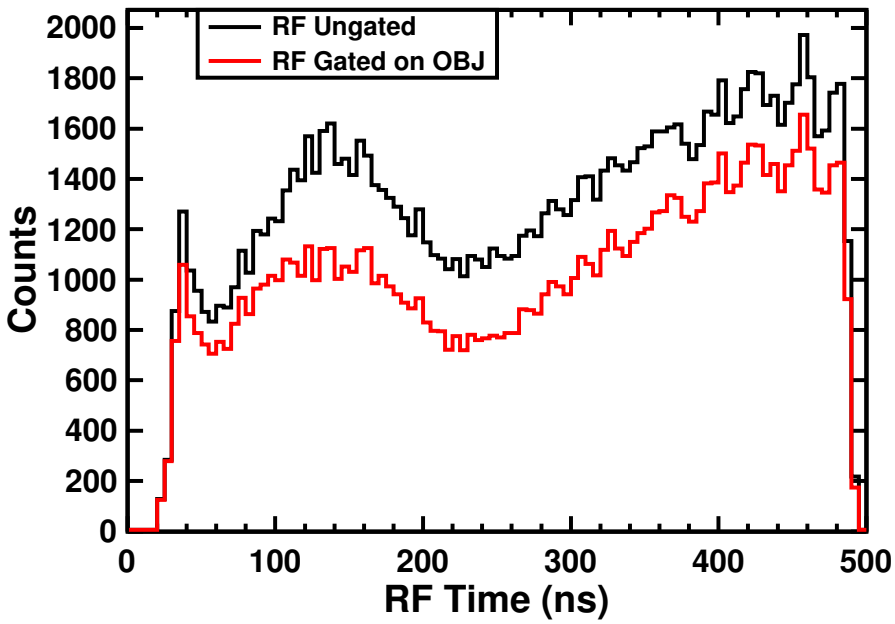

Figure 5.10: RF time plots that illustrate the OBJ efficiency. The black histogram is the ungated RF time for an example run, and the red histogram is the RF time for the same run gated on valid counts in the OBJ.

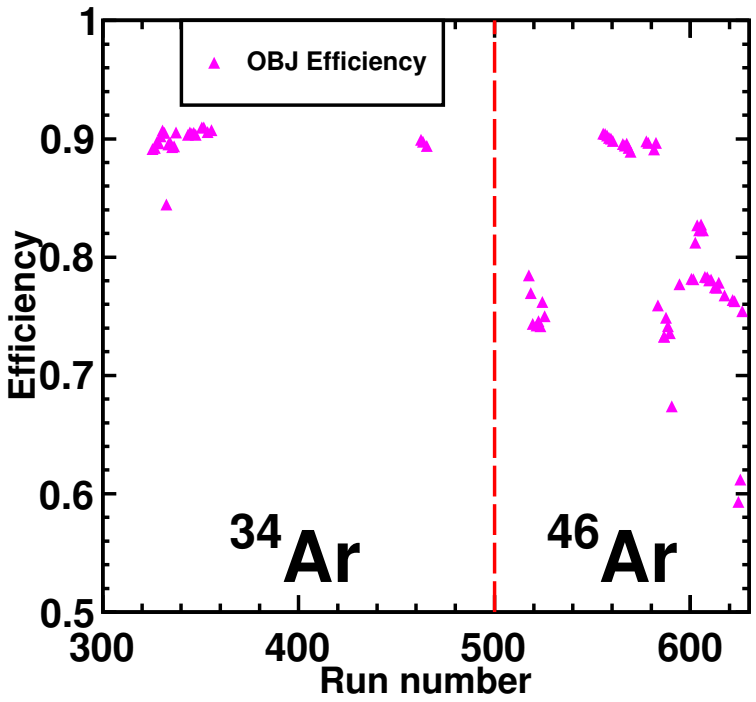

Figure 5.11: OBJ efficiency plotted against the experiment run number.

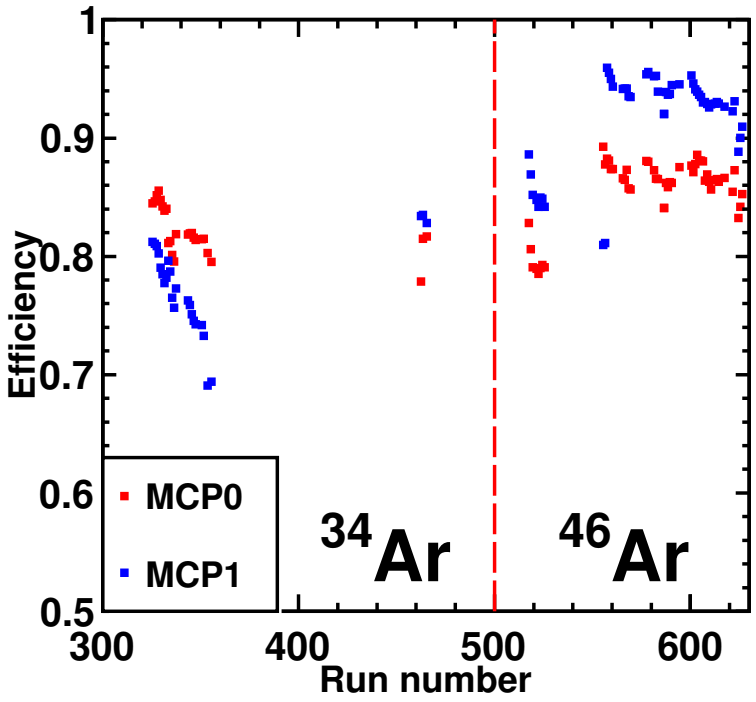

Figure 5.12: MCP0 (red) and MCP1 (blue) scaler efficiencies plotted against the experiment run number.

We compare the ungated S800 (E1 scintillator) data with data gated on each MCP TDC signal to compute the efficiency. The resulting efficiencies are shown in Figure 5.12. Increases in MCP efficiency correspond to increases in MCP bias voltage.

5.4.3.3 MCP Position

For the ^{46}Ar beam, we need to know the overall efficiency of the MCP beam tracking system ($\varepsilon_{\mathrm{MCPTrack}}$). This quantity expresses what fraction of the data has valid beam positions in both MCP0 and MCP1. In the case of the ^{34}Ar beam, we simply set $\varepsilon_{\mathrm{MCPTrack}}$ to 1 in Equation 5.5.

Each MCP has four corner signals that together give us the position of the beam particle in the plane of the aluminized Mylar foil sitting in the beam path. A naive approach to

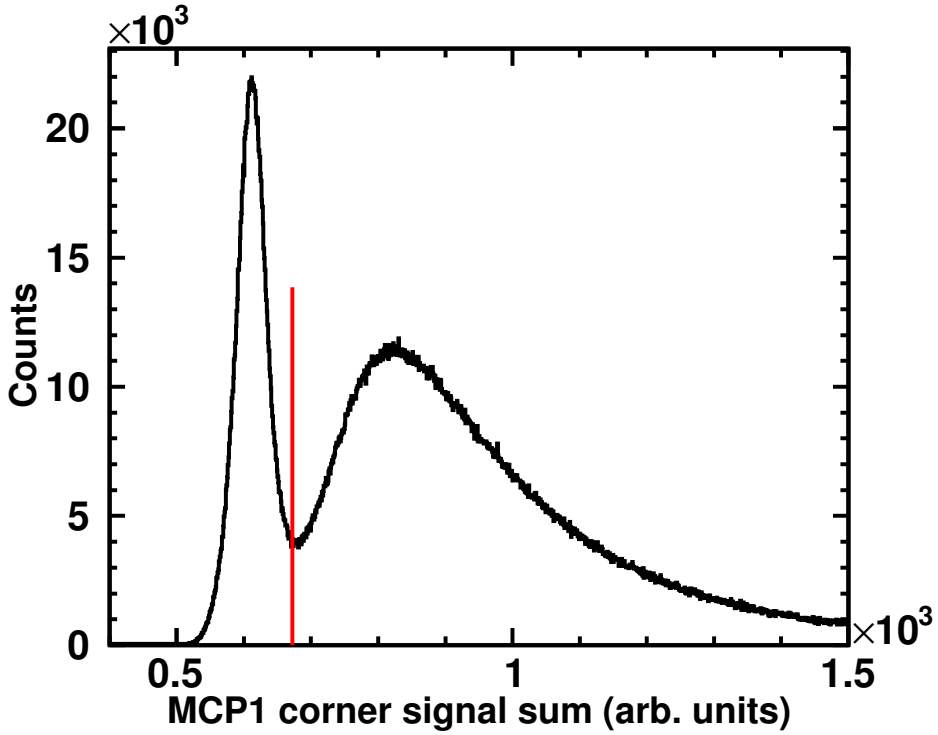

Figure 5.13: Sum of the MCP1 corner signals, as well as a red line indicating the threshold value.

calculating the MCP tracking efficiency would be to set a threshold on each individual corner signal for a given MCP and count how many events have all four corners above the threshold (compared to counts in the S800). However, this prescription results in throwing out legitimate data. Some counts of interest might have above-threshold signal in only 2 or 3 MCP corners, depending on where the charge deposition occurs. So, we instead set a threshold on the *sum* of all the corner signals in an MCP, as shown in Figure 5.13. The prominent peak below the threshold corresponds to events with pedestal data in all four corners, which are exactly the events we wish to discard.

We also cut on the calculated MCP position to remove non-physical data that results from negative values in the pedestal-subtracted corner signals (due to the non-zero width of the pedestal peak) that are used to calculate the raw x and y positions.

Now we can calculate the overall beam tracking efficiency using the same approach as with the MCP scalers. We calculate the ratio of counts in the S800 gated on both MCP corner-sum cuts and both MCP position cuts to the ungated S800 counts. The resulting efficiency $\varepsilon_{\mathrm{MCPTrack}}$ is 81.1%.

5.4.4 Beam Purity

To correct for the incoming beam purity, we simply generate beam identification plots (see Figs. 4.22 and 4.23) for each data run and calculate the relative presence of the desired beam species. The resulting beam purity for each run is shown in Figure 5.14. The average beam purities were 94% for the ^{34}Ar beam and 99.6% for the ^{46}Ar beam. The beam purity for each species remained consistent throughout the experiment.

5.4.5 Beam Normalization

We used the MCP scalers to count the incoming beam particles and determine the $N_{\mathrm{beam}}^{\mathrm{Det}}$ term needed for the absolute differential cross sections (see Equations 5.3 and 5.4). Unfortunately, the experiment suffered from high noise in the MCP electronics, which adversely affected the scalers. Much of the problem was due to multiple-firing of the circuit for a single beam particle. In order to address this issue, we set up another scaler circuit, which we will refer to as the *cleaned-up* (CU) scaler, that was blocked off for 200 ns after the arrival of a signal from the MCP TDC. The CU scaler essentially vetoed the multiple-firing, and significantly reduced the noise.

However, the CU scaler is not completely free of noise. To further understand the effect of noise on the MCP scalers we performed beam "ramps" in which the beam rate was

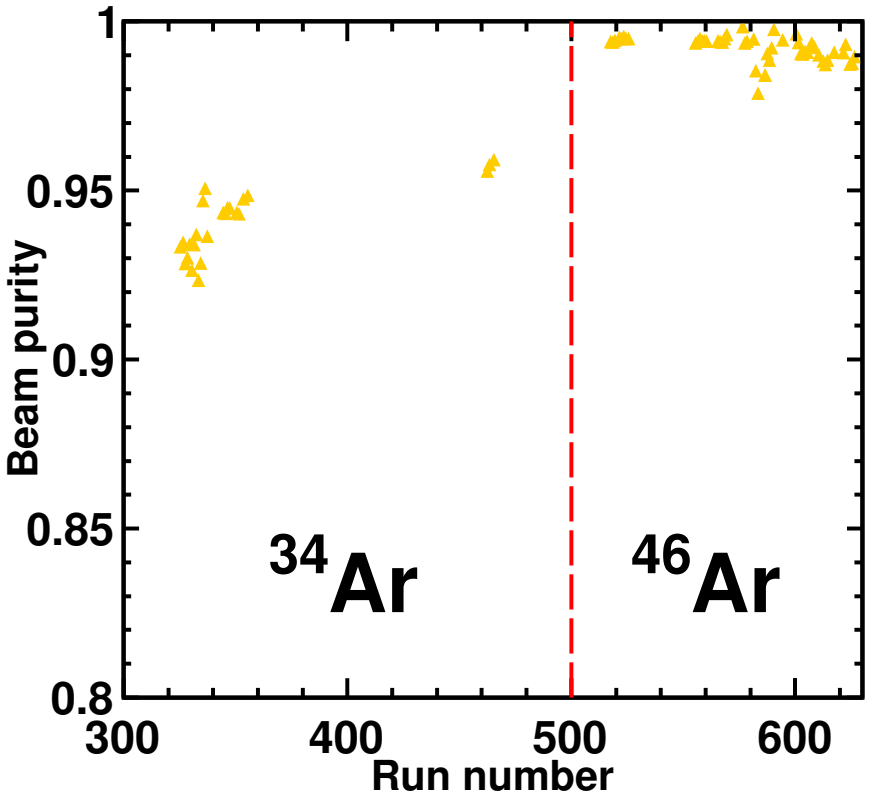

Figure 5.14: Purity of both argon secondary beams over time.

changed incrementally to determine how much of the scaler data was real and how much was electronics noise. Figure 5.15 shows plots of the beam ramp scaler data for both MCP0 and MCP1. Clearly, there is still a positive scaler rate for both MCPs even when the beam is completely attenuated (i.e. when there is no beam present at all). We use this rate as a measure for the noise in each MCP.

Once we have the rate of noise for each MCP, we then subtract it from the MCP CU scaler rates in each run of the data to yield a noise-corrected MCP scaler. We use this noise-corrected scaler as well as the MCP scaler efficiencies (found in Section 5.4.3.2) to calculate the number of beam particles on target for each run, which we then sum together to get $N_{\text{beam}}^{\text{Det}}$. In principle, the number of beam particles detected at MCP0 and MCP1 should be consistent within 5 to 10 %. A small number of runs had large deviations (20%) between the number of beam particles on MCP0 and on MCP1, and so these runs were discarded. For the ^{46}Ar beam, the result is 8.04×10^{10} total beam particles (the associated uncertainty will be discussed in the next chapter).

Unfortunately, the CU scalers were only implemented towards the end of the ^{34}Ar beam. So while there are a few runs of ^{34}Ar data that have these scalers, most of the runs for this beam do not. Therefore we need a different approach to normalize the ^{34}Ar data. We must also keep in mind that the ultimate goal of this work is a comparison between the $^{34}\text{Ar}(p,d)$ and $^{46}\text{Ar}(p,d)$, so the normalization procedures must be consistent between the two reaction systems.

Our approach is to use the ^{34}Ar data runs (many of which were for calibration) that do have CU scalers and find other scalers (which exist in all of the data) that correlate well. Then, we can fit the relationship and calculate expected values for the CU scaler. Figure 5.16 shows two such scaler correlations. The left plot shows correlations for MCP1 relative

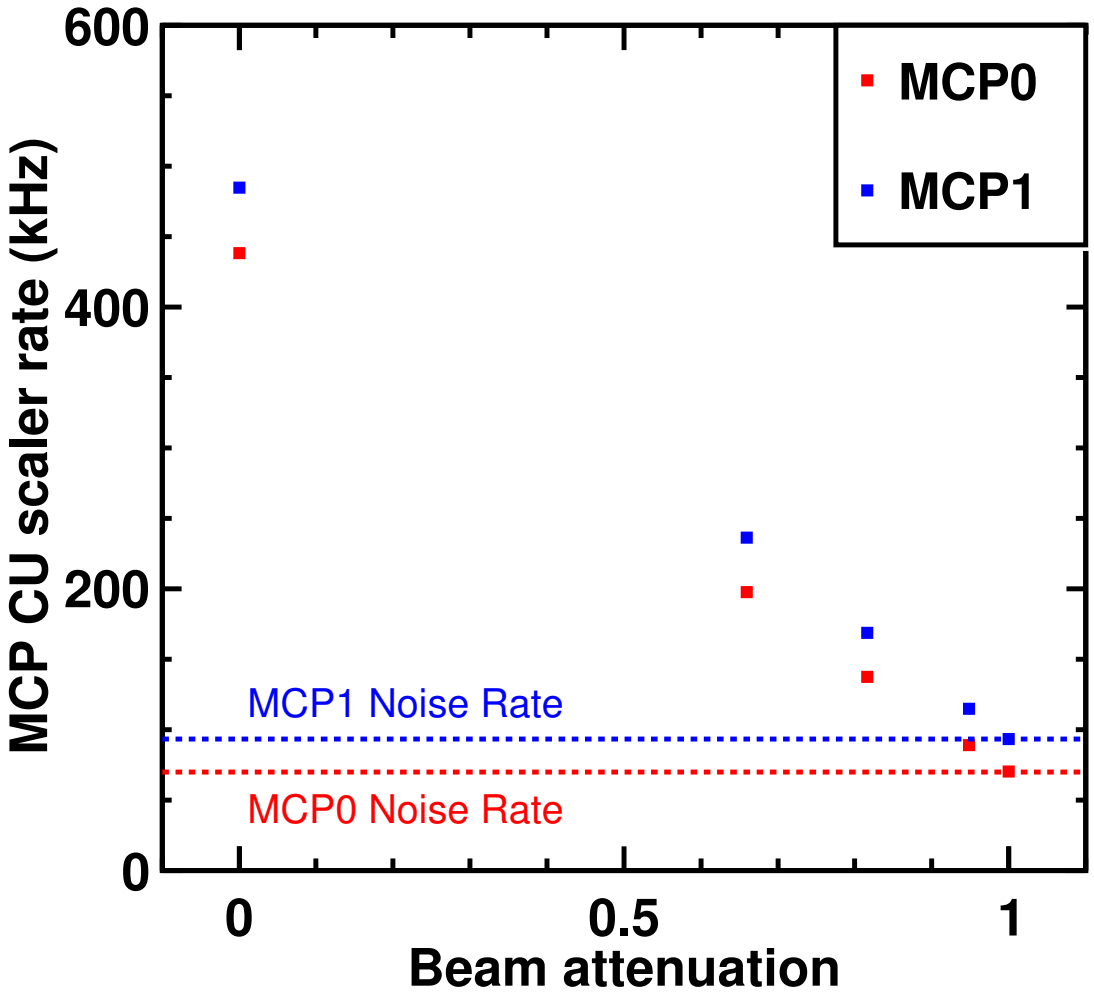

Figure 5.15: Detected MCP cleaned-up (CU) scaler rates vs. beam attenuation for both MCP0 (red) and MCP1 (blue). When the beam attenuation is 1, the beam is completely removed from the experimental setup.

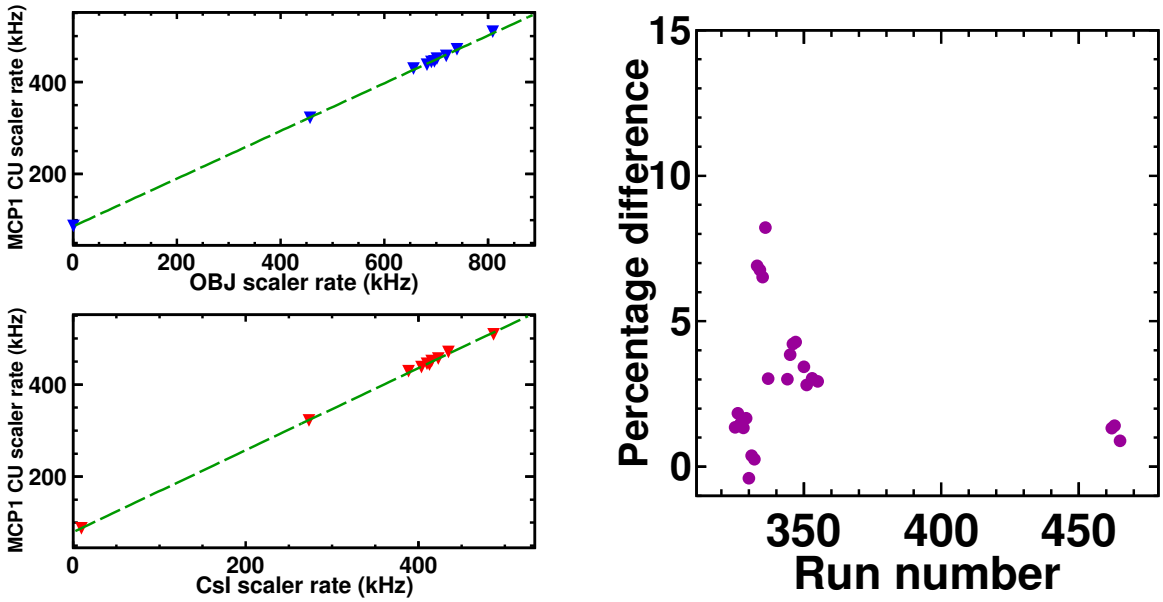

Figure 5.16: (a) MCP1 CU scaler correlations with the OBJ scintillator scaler (top, blue) and the CsI OR of OR scaler (bottom, red). We use the resulting linear fits (dashed green lines) to calculate the expected CU scaler for data runs in which it was not directly recorded. (b) Percentage difference between the expected MCP1 CU scaler calculated from the OBJ scaler and the CsI OR of OR scaler. They agree within 10%.

to the CsI OR of OR scaler as well as the OBJ scaler. We then use the resulting fits to calculate expected CU scaler rates. The right plot shows the percentage difference between the CU scaler calculated from the CsI scaler and the CU scaler calculated from the OBJ scaler. Each point corresponds to an ^{34}Ar data run that lacks the CU scaler. Clearly, using either the CsI scaler or the OBJ scaler yields similar results within less than 10%.

Using the calculated CU scalers in combination with the run-by-run MCP scaler efficiency and beam purity, we calculate 6.28×10^{10} total ^{34}Ar beam particles from the OBJ scaler, and 6.09×10^{10} from the CsI scaler. These values agree within 3%, so we simply use the average of the two (6.18×10^{10}) as our measure of the total number of beam particles on target.

We applied a similar approach to the ^{46}Ar data to demonstrate that this method produces consistent results for both beams. Using this correlation method, we get 8.13×10^{10} ^{46}Ar

beam particles from the OBJ scaler and 7.99×10^{10} from the CsI scaler. These values are within 1% of the 8.04×10^{10} value calculated above with the measured CU scalers. Therefore, we are confident that our normalization technique yields consistent results for both reaction systems.

5.4.6 Overall Normalization Uncertainty

In order to assess the uncertainty of the normalization procedure, we divide the data up into five groups and calculate cross sections for each. The fluctuation of the cross section across separate data groups gives us an estimate of the overall normalization uncertainty.

Figure 5.17 presents the absolute differential cross section at 7 degrees in the center-of-mass frame for both the ^{46}Ar (to $^{45}\mathrm{Ar}_{\mathrm{g.s.}}$ and $^{45}\mathrm{Ar}_{\mathrm{E^*=0.542\ MeV}}$, shown in red) and ^{34}Ar (to $^{33}\mathrm{Ar}_{\mathrm{g.s.}}$, shown in blue) reaction systems. The solid lines indicate the cross section value taken from the complete data set. Although there is some fluctuation from group to group, the total normalization uncertainty is on the order of 10% (indicated by the dotted lines).

5.5 Differential Cross Sections and Spectroscopic Factors

After normalization, we have a set of differential cross sections that we can compare to theory to elicit nuclear structure information. Here, we present the final differential center-of-mass cross sections for $^{34}\mathrm{Ar}(p,d)$ and $^{46}\mathrm{Ar}(p,d)$ reactions. We also extract SFs from the differential cross sections by normalizing the data to (p,d) reaction calculations generated in the ADWA framework using the TWOFNR code as described in Chapter 2. For the

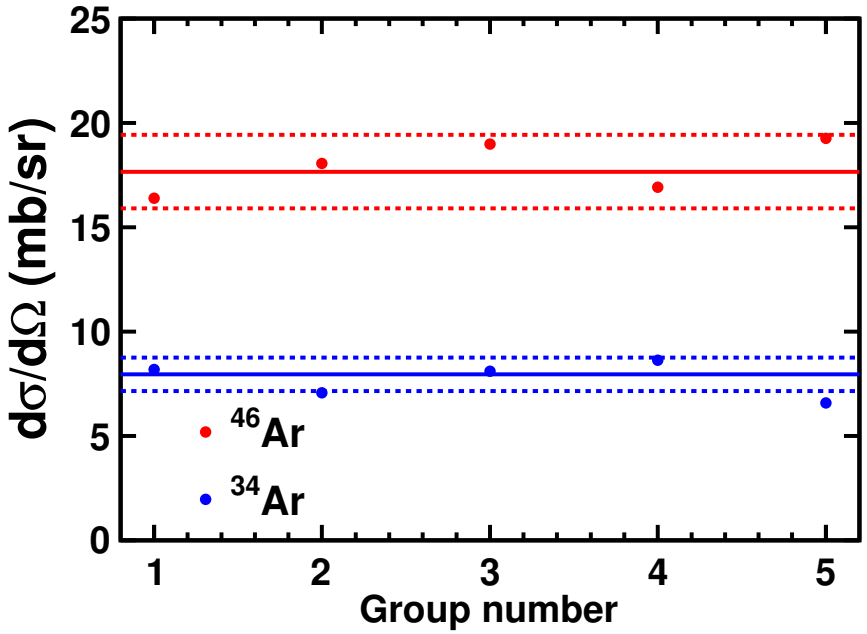

Figure 5.17: Absolute differential cross sections at 7 degrees in the center-of-mass frame for several different subsets (or groups) of data. The ^{34}Ar cross section is shown in blue, and the ^{46}Ar in red. The solid line corresponds to the cross section value for the entire data set, and the dotted lines are 10% from the solid line.

ground state transitions, we use two different optical models in the ADWA calculations: the CH89 global optical potential, and the JLM microscopic optical potential constrained by Hartree-Fock density calculations. Each of these two optical models yields different SFs, so we label them SF(CH89) and SF(JLM), accordingly. The JLM calculations are not available for excited states because the nucleon density calculations are more complicated, so for the ^{45}Ar excited-state calculations we only use the CH89 potential.

The depicted uncertainty for each angular bin in the differential cross sections includes statistical error as well correlated parameter uncertainty from the Gaussian fit. The cross section also has an overall normalization uncertainty (discussed in Section 5.4.6) which is only taken into account during the spectroscopic factor extraction.

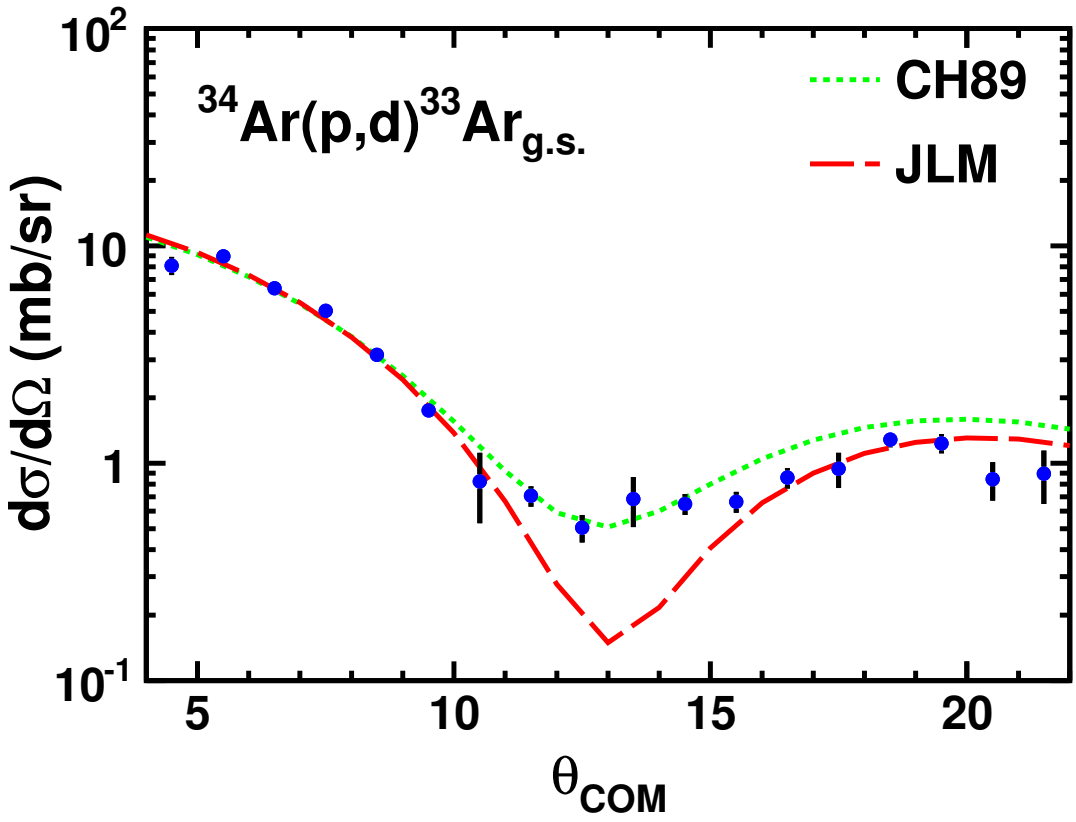

Figure 5.18: Differential cross section for $^{34}\mathrm{Ar}(p,d)^{33}\mathrm{Ar}_{\mathrm{g.s.}}$ in the COM frame. The blue circles are the data from the present work. The lines correspond to TWOFNR calculations normalized to the first peak using CH89 (dotted, green) and JLM (dashed, red) optical potentials. The calculations shown are multiplied by the best fit spectroscopic factors.

5.5.1 $^{34}\mathbf{Ar}(p,d)$

Figure 5.18 shows the measured differential cross section in the COM frame for $^{34}\mathrm{Ar}(p,d)^{33}\mathrm{Ar}_{\mathrm{g.s.}}$, along with SF-normalized single-nucleon transfer reaction calculations. The $l = 0$ shape of the data matches the calculations well, as expected. We observe a large peak at forward angles, and another (smaller) peak at ≈ 18 degrees. The relative uncertainty on lower cross section points between 10 and 15 degrees is high compared to larger cross section points. This is due to decreased statistics, as well as increased parameter correlations (i.e. higher sensitivity to small parameter shifts). Table 5.2 lists the cross section values and associated uncertainties.

^{34}Ar$(p,d)^{33}$Ar, $E^* = 0$ MeV		
θ_{COM} (degrees)	$d\sigma/d\Omega$ (mb/sr)	Uncertainty (mb/sr)
4.5	8.11	0.77
5.5	8.98	0.49
6.5	6.38	0.29
7.5	5.03	0.21
8.5	3.15	0.16
9.5	1.75	0.12
10.5	0.82	0.29
11.5	0.71	0.08
12.5	0.51	0.07
13.5	0.69	0.18
14.5	0.65	0.07
15.5	0.66	0.07
16.5	0.86	0.09
17.5	0.94	0.17
18.5	1.29	0.10
19.5	1.23	0.13
20.5	0.84	0.17
21.5	0.90	0.25

Table 5.2: Differential cross section for ^{34}Ar$(p,d)^{33}$Ar$_{\mathrm{g.s.}}$ in the COM frame with statistical uncertainty.

We follow the methodology outlined in [26] and extract the spectroscopic factor by comparing the TWOFNR calculations to the most forward peak. The normalization procedure is a χ^2-minimization using the six data points located in the first peak. We get a 10% uncertainty from the minimization and another 10% uncertainty from the overall normalization described in the previous section. Combining these two sources of uncertainty yields 14% relative error. Figure 5.18 shows normalized calculations for both the CH89 global optical model (dotted, green) and the JLM-HF microscopic optical model (dashed, red). We extract SF(CH89) = 1.00 ± 0.14 and SF(JLM) = 0.73 ± 0.10. Comparing to SF(LBSM) = 1.31 yields R_s(CH89) = 0.76 ± 0.11 and R_s(JLM) = 0.56 ± 0.08.

5.5.2 ^{46}Ar(p,d)

To extract the spectroscopic factor corresponding to the ^{45}Ar ground state, we must first disentangle the cross section contributions from the ground state and first excited state. Although we are unable to cleanly resolve each peak, at forward angles we see a "shoulder" at slightly positive excitation energy on the 0-MeV peak that most likely represents minor population of the first excited state. Our approach is to fit the 0-MeV peak with two Gaussians (one for each state). We generate excitation energy spectra for different angular slices and fit these two Gaussians (as well as higher lying peaks) simultaneously so that the sum of all Gaussian functions reproduces the measured histogram. We also fix the widths of the two Gaussian functions to be identical, since the experimental response for each state should be the same. Figure 5.19 depicts an example excitation spectrum. The individual Gaussian fits are drawn in blue, and their sum in red. The best-fit means for the ground state and first excited state are indicated in green. Although we do not exactly reproduce the correct values of 0 and 0.542 MeV, the values from the fit are reasonably close and there are no other nearby states in ^{45}Ar. As described above, we integrate each Gaussian peak to generate angular distributions at forward angles for both the ground state and the first excited state, and then perform a χ^2-minimization to get the SFs. The resulting spectroscopic factors are SF(CH89) = 4.77 $\pm$ 0.67 and SF(JLM) = 3.59 $\pm$ 0.50 for the ground state, and SF(CH89) = 0.38 $\pm$ 0.12 for the first excited state. Comparing to the LBSM values of 5.16 for the ground state and 0.78 for the first excited state, we get reduction factors of R_s(CH89) = 0.92 $\pm$ 0.13 and R_s(JLM) = 0.70 $\pm$ 0.10 for the ground state, and R_s(CH89) = 0.49 $\pm$ 0.15 for the first excited state. As in the ^{34}Ar case, we combine 10% statistical uncertainty with 10% overall normalization uncertainty for 14% total uncertainty.

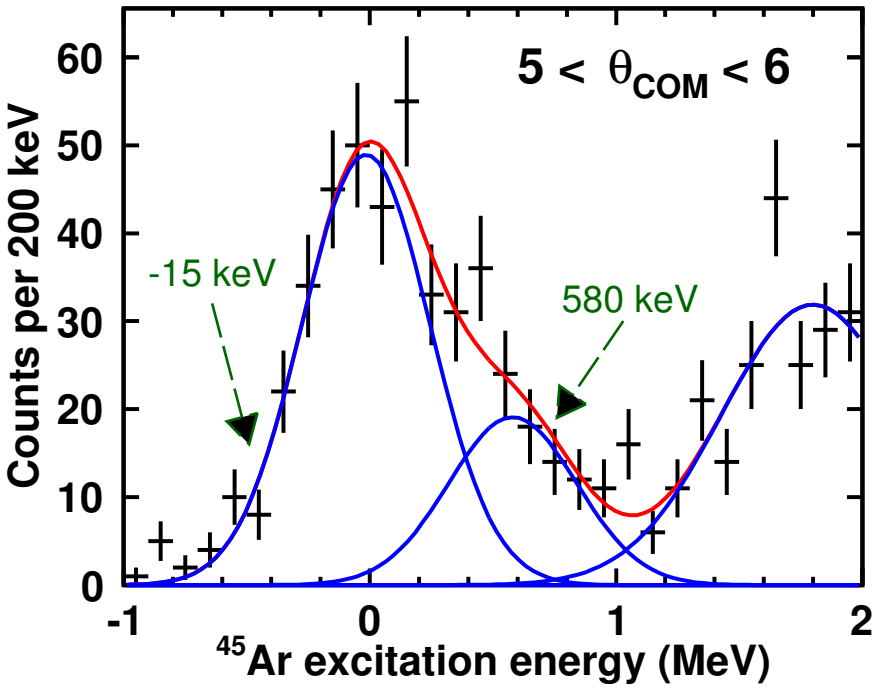

Figure 5.19: ^{45}Ar excitation energy spectrum for one angular bin in which the 0 MeV peak is fit with two Gaussians. Individual Gaussian fits are drawn in blue, and their sum in red.

Although we extract the SFs from only the most forward angles, we can still use other data in the differential cross section to check our results. The expected differential cross section for the $p_{3/2}$ first excited state drops with increasing COM angle when compared to ground state cross section. In Figure 5.20, we show ADWA calculations for transfer into the ground state (red) and first excited state (blue) of ^{45}Ar. For illustration, each calculation is scaled by the LBSM predicted SF (5.16 for the ground state, 0.78 for the excited state). The green dashed line shows the ratio between the two cross sections. Between 11 and 18 degrees, the ground state to first excited state ratio reaches a relative maximum of about an order of magnitude. Therefore, we assume that in this angular range the 0-MeV peak purely (within 10%) consists of the ^{45}Ar ground state. Normalizing the ground state calculations to the data in this angular range yields SF(CH89) = 4.67 and SF(JLM) = 3.43. These results

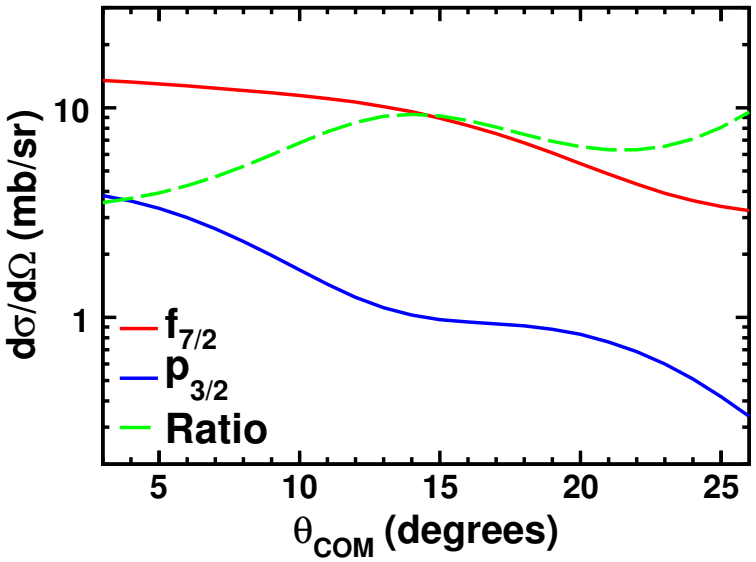

Figure 5.20: ADWA calculations for 46Ar$(p,d)^{45}$Ar for the ground state (red) and first excited state (blue) of ^{45}Ar. The ratio of the two cross sections is given by the green dashed line.

are well within the stated 14% uncertainty of the SFs extracted from the forward-angle double-Gaussian fits.

Fig. 5.21 and Table 5.3 show the final differential cross section for the combined (p,d) transfer to both the ground state and the 542 keV excited state. The cross section drops steadily with increasing center-of-mass angle without any significant peaks. We note that the shape of the ground state calculation matches the data quite well with the exception of a small enhancement at the most forward angles. This is exactly the region at which the first excited state calculation has a maximum. This, in combination with the distorted shape of the 0-MeV peak described above, gives us confidence that we are in fact seeing contribution from the first excited state.

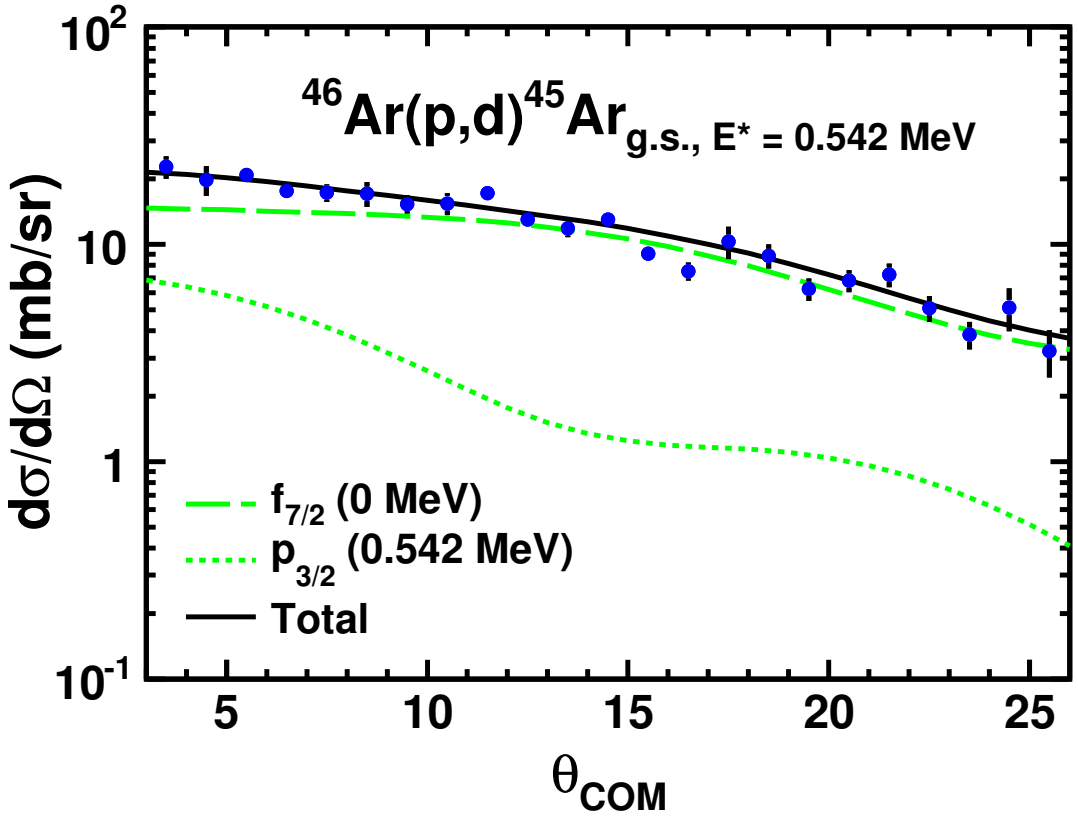

Figure 5.21: Differential cross section for $^{46}\mathrm{Ar}(p,d)^{45}\mathrm{Ar}_{\mathrm{g.s.},E^*=0.542\ \mathrm{MeV}}$ in the COM frame. The blue circles are the data from the present work. The lines correspond to TWOFNR calculations for two different final ^{45}Ar states normalized to the SFs which were obtained as described in the text.

$^{46}\mathrm{Ar}(p,d)^{45}\mathrm{Ar}$, $E^* = 0, 0.542$ MeV		
θ_{COM} (deg.)	$d\sigma/d\Omega$ (mb/sr)	$\Delta d\sigma/d\Omega$ (mb/sr)
3.5	15.36	2.92
4.5	14.34	2.56
5.5	14.21	1.46
6.5	12.75	1.73
7.5	12.68	1.68
8.5	12.02	1.12
9.5	10.79	1.42
10.5	10.85	1.42
11.5	11.31	0.48
12.5	8.94	0.78
13.5	8.34	0.80
14.5	9.47	1.05
15.5	6.25	0.58
16.5	5.32	0.68
17.5	8.29	1.27
18.5	6.61	0.91
19.5	5.33	0.75
20.5	4.42	0.58
21.5	5.55	0.95
22.5	3.64	0.60
23.5	2.60	0.42
24.5	2.39	0.41
25.5	2.41	0.56

Table 5.3: Combined differential cross section for $^{46}\mathrm{Ar}(p,d)^{45}\mathrm{Ar}$ to states at 0 and 0.542 MeV in $^{45}\mathrm{Ar}$ in the COM frame with uncertainty.

Isotope	ΔS (MeV)	SF(LBSM)	SF(CH89)	R_s(CH89)	SF(JLM)	R_s(JLM)
^{34}Ar	12.40	1.31	1.00 ± 0.14	0.76 ± 0.11	0.73 ± 0.10	0.56 ± 0.08
^{46}Ar	-10.63	5.16	4.77 ± 0.67	0.92 ± 0.13	3.59 ± 0.50	0.70 ± 0.10

Table 5.4: Extracted spectroscopic factors and reduction factors for both ^{34}Ar and ^{46}Ar. Results are shown using both the CH89 global model as well as the JLM microscopic model.

5.6 Reduction Factor Asymmetry Dependence

Table 5.4 shows a summary of the extracted SFs and reduction factors. We compare the current work to the previous 33 MeV/u transfer measurement [55] using both the CH89 global potential and the JLM microscopic potential in Figures 5.22 and 5.23, respectively. The green squares represent reduction factors from this work, and the open red circles are from [55]. For both optical potentials, the reduction factor magnitudes are comparable between the current work and the low-energy measurement. More importantly, the asymmetry trend (indicated by the colored lines) from the current work agrees with the previous measurement with either potential. We conclude that with a consistent analysis methodology, single-neutron pickup reactions give consistent results for the same reactions at different energies.

In Figure 5.25, we compare both the low and high energy transfer reduction factors (red circles and green squares, respectively) to those extracted from knockout reaction data (blue triangles). We see a clear discrepancy between the asymmetry trend in the transfer data (red and green lines) to the one in the knockout data (blue line) [52]. We conclude that our 70 MeV/u single-neutron pickup reactions do not reproduce the systematic asymmetry dependence seen in the single-nucleon knockout results. Although we plot the CH89 results to illustrate the disagreement, it persists when using the JLM as well (even though the positive-ΔS reduction factors are closer in magnitude to the knockout).

Finally, we compare our results to recent quasi-elastic proton scattering work in Fig-

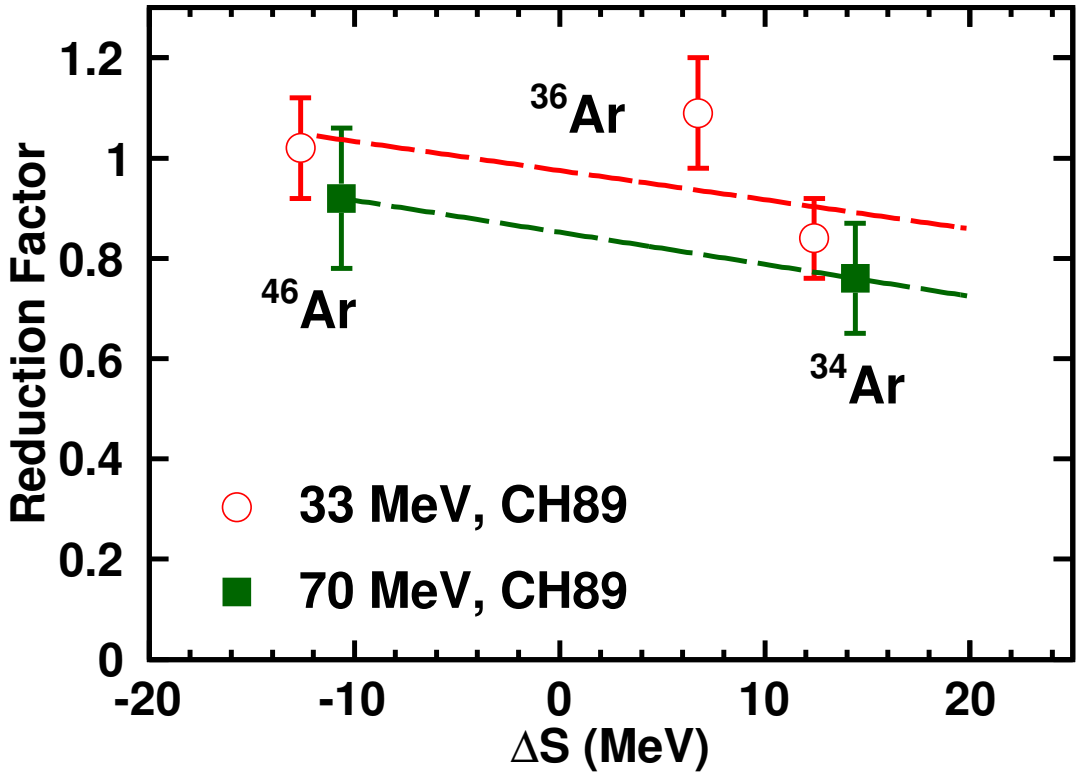

Figure 5.22: Asymmetry dependence of reduction factors using the CH89 global optical model. We show reduction factors from the current work (green squares) as well as the 33 MeV/u measurement (open red circles). Each line represents the best fit to the corresponding reduction factor data.

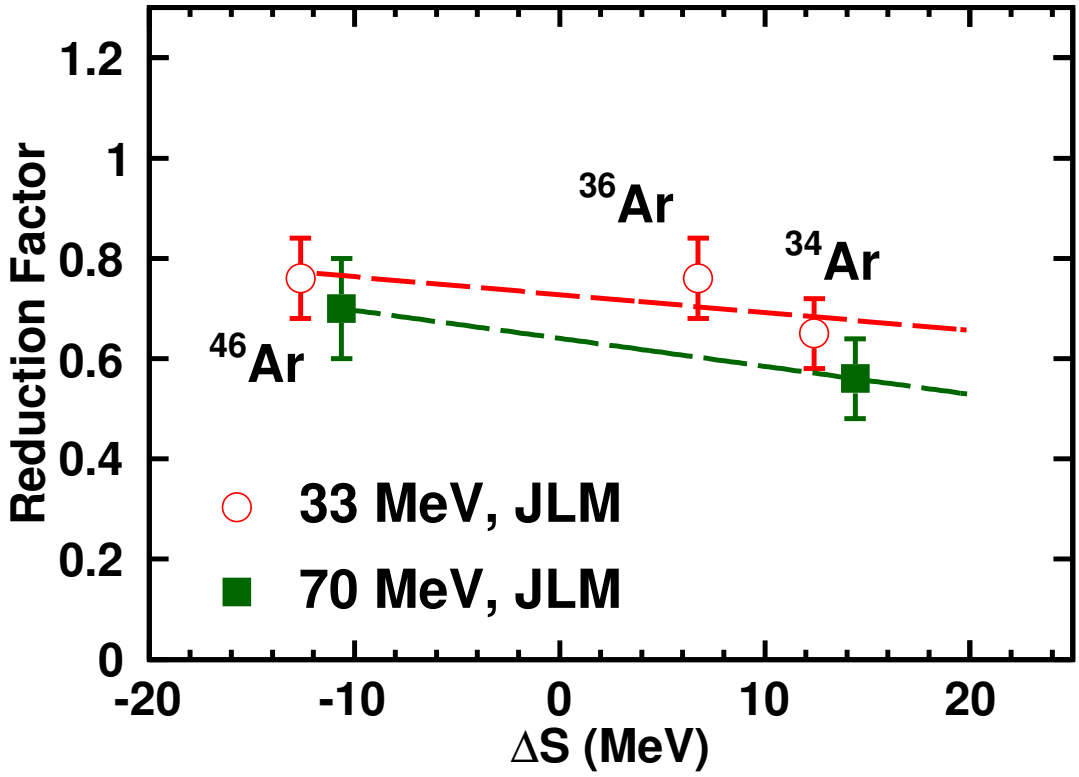

Figure 5.23: Asymmetry dependence of reduction factors using the JLM microscopic optical model. We show reduction factors from the current work (green squares) as well as the 33 MeV/u measurement (open red circles). Each line represents the best fit to the corresponding reduction factor data.

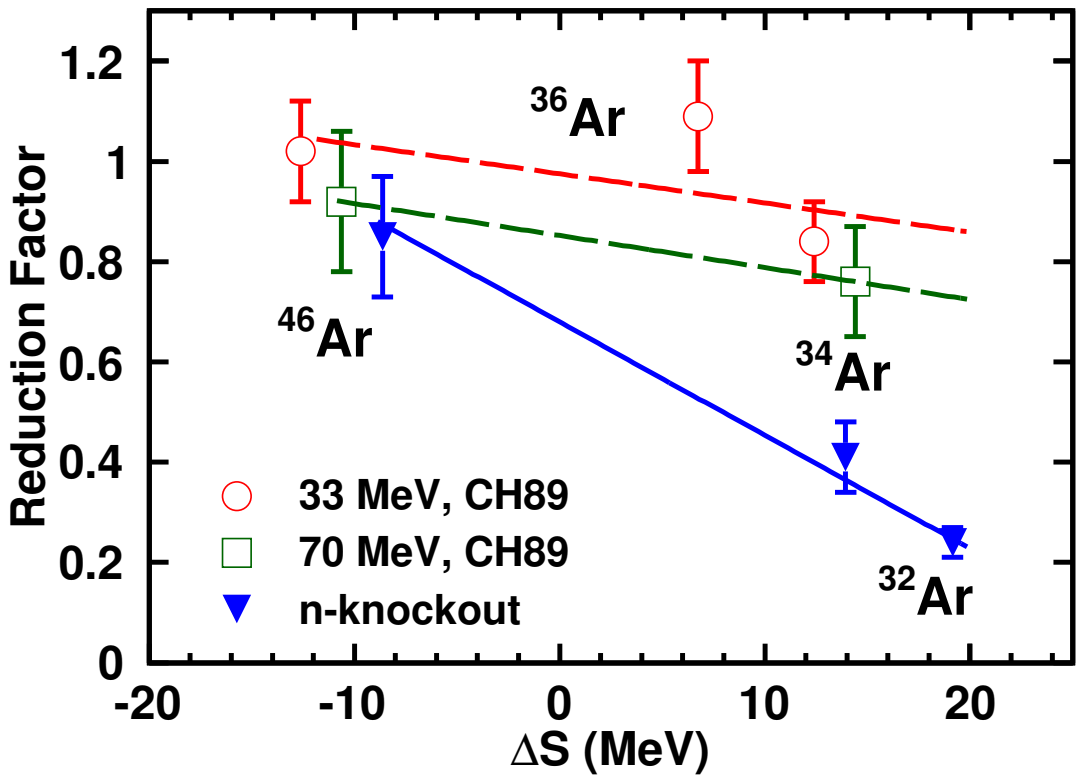

Figure 5.24: Asymmetry dependence of reduction factors from transfer reactions using CH89 (open green squares and open red circles) and from knockout reactions (blue triangles). Each line represents the best fit to the corresponding reduction factor data.

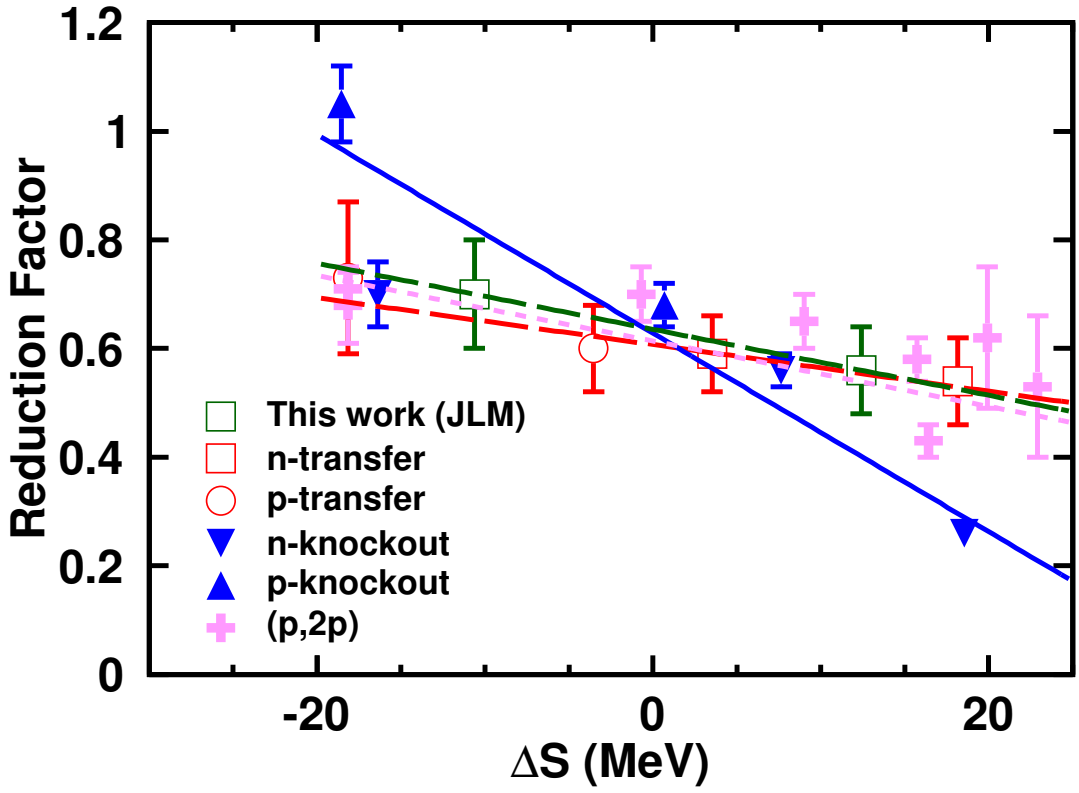

Figure 5.25: Asymmetry dependence of reduction factors from transfer reactions using CH89 (open green squares and open red circles), from knockout reactions (blue triangles), and from $(p, 2p)$ reactions (pink crosses). All data points represent measurements on oxygen isotopes except for the open green squares, which come from the present work on argon isotopes.

ure 5.24. The red open square (circle) points show reduction factors from single-neutron (proton) transfer measurements [53], while the blue triangles that face downward (upward) correspond to neutron (proton) knockout measurements [52]. The pink crosses indicate reduction factors from $(p, 2p)$ quasi-elastic scattering data from [75] and [76]. Lastly, the green squares are from the current work using the JLM microscopic model. All points in this figure represent reduction factors from oxygen isotopes except the green squares, and each colored line represents a best fit to the data of the corresponding color. We see that our results show an asymmetry dependence consistent with the one seen in the oxygen transfer data in [53] as well as the one seen in the $(p, 2p)$ data from [75] and [76].

Chapter 6

Summary and Conclusions

> All of physics is either impossible or trivial. It is impossible until you understand it, and then it becomes trivial.
>
> Ernest Rutherford

In this work, we explored the asymmetry dependence of single-particle structure across the argon isotopic chain by studying two argon isotopes: ^{34}Ar and ^{46}Ar. Our goal was to extract *spectroscopic factors* (SFs), which quantify the occupancy of a single-particle orbital, in order to constrain the influence of nucleon-nucleon correlations along the argon isotopic chain. Previous transfer measurements of single-particle structure in the argon isotopes indicate weak asymmetry dependence in the reduction factor, whereas knockout measurements of these isotopes show a strong dependence. This discrepancy between transfer and knockout techniques is an unresolved problem that has consequences on both our understanding of nuclear structure as well as the theoretical reaction models that describe these experimental techniques. To address this inconsistency, we performed (p, d) measurements on argon isotopes at 70 MeV/u, a much higher beam energy than the previously used 33 MeV/u. This is the first high energy transfer reaction measurement for nuclei with this much asymmetry. If the 70 MeV/u results disagree with the 33 MeV/u trend, this would indicate deficiency in the current understanding of the transfer mechanism. To ensure a consistent comparison

with the lower energy measurement, we used the adiabatic distorted wave approximation (ADWA) as a theoretical framework to extract SFs.

To obtain the SFs, we measured (p, d) single-neutron transfer reaction differential cross sections on each isotope. We determined these differential cross section in a kinematically complete measurement using the High Resolution Array (HiRA) to detect the outgoing deuterons, the S800 Spectrograph to detect the heavy recoil (either ^{33}Ar or ^{45}Ar), and Microchannel Plates (MCPs) to normalize the cross section and also localize the single-neutron transfer on the reaction target. Each individual detector system required separate calibration techniques. As part of this calibration process, we characterized the dead layer and detector thicknesses for the HiRA "E" silicon detectors. We then merged the calibrated data to study events which featured the coincidence of a deuteron in HiRA and the appropriate heavy argon recoil in the S800. From these coincidence events we generated angular distributions, which we then normalized to produce the absolute differential cross sections.

We then extracted experimental spectroscopic factors (SFs) taking the ratio of the experimental cross sections to the ADWA transfer reaction cross section calculations. The resulting ground-state spectroscopic factors were then compared to the large-basis shell model (LBSM) calculations to produce reduction factors. From ^{46}Ar to ^{34}Ar we see a relatively weak reduction trend. This corroborates the previous transfer data and is not consistent with the quenching observed in the knockout results. This trend holds true for both of our choices of optical model: the CH89 global optical model and the JLM microscopic model. Therefore, we conclude that the transfer reaction mechanism is consistent in this energy range. Although this conclusion does not resolve the transfer-knockout discrepancy, these results do support the reliability of the transfer reaction as a probe of nuclear structure.

At this point we wish to emphasize that despite the discrepancy in absolute spectroscopic

factors, both knockout and transfer are crucial probes for studying nuclear structure. Each of these probes has unique advantages, and together they offer a complementary approach to studying single-particle structure rather than a competing one. Furthermore, each technique has consistently reproduced the asymmetry trends discussed here across different systems and different experimental groups. We assert, therefore, that the difference in asymmetry dependence between transfer and knockout originates from an incomplete understanding of one or both of these reaction mechanisms. Clearly, more work is needed before this disparity is settled.

A better theoretical understanding of the knockout model is important, especially regarding the validity of the eikonal approximation for deeply bound nucleons as well as the role of core excitations in the knockout mechanism [67, 68]. On the transfer side, theoretical work is underway to address open questions regarding the proper treatment of nonlocality in optical potentials, and also to expand the applicability of the Faddeev equations in transfer reactions [142]. More generally, the nuclear theory community has begun making concerted efforts towards proper uncertainty quantification in reaction models (see [143] for an example of this work in the transfer reaction context). Aside from increasing transparency, putting explicit error bars on theoretical calculations will enable better diagnosis of critical weaknesses in nuclear reaction models.

More transfer reaction measurements for asymmetric systems are necessary, as well as further investigation of new techniques like quasi-elastic proton scattering and electron scattering on unstable isotopes [144]. Electron scattering is a particularly promising avenue of investigation, as its electromagnetic nature provides a different pathway to access nuclear structure than hadronic probes like transfer and knockout. More systematic studies in the spirit of [26] would be useful in order to better understand the wide spread of transfer

reaction reduction factors at a given asymmetry. Future rare isotope facilities like FRIB will significantly expand the boundaries of reachable asymmetry for any of these reaction mechanisms.

Ultimately, the specific question of reduction-factor asymmetry dependence illuminates a larger issue in nuclear physics: the separation between nuclear structure and nuclear reactions. Transfer, knockout, and other reaction probes are commonly used to study nuclear structure, despite the fact that the underlying theoretical scheme of the reaction technique is segregated from the one used to understand the structure. This holds true in our work: the LBSM spectroscopic factors were calculated with an entirely different Hamiltonian than the one used by the ADWA model (which assumes that the $A(p,d)B$ reaction is a three-body system). This gap between the two disciplines is an inherent weak link in our ability to distill insight into the properties of nuclei from experimental data. In order to make progress, the field of nuclear physics faces the challenging task of uniting nuclear structure and nuclear reactions within a single theoretical framework based in first principles. There are already encouraging results on this front, albeit limited to simple systems like alpha-alpha scattering or single-neutron transfer on light nuclei [145, 146, 147, 148]. Next-generation experimental facilities, innovations in reaction theory, and advanced leadership-class supercomputing facilities all promise a deeper understanding of nuclei and their interactions.

BIBLIOGRAPHY

BIBLIOGRAPHY

[1] E. Rutherford. "The Scattering of α and β Particles by Matter and the Structure of the Atom". In: *Philosophical Magazine* 21 (1911), pp. 669–688.

[2] Gerald Cleaver. *Universe and Multiverse, Part 3*. 2012. URL: https://biologos.org/blogs/archive/universe-and-multiverse-part-3.

[3] *Science at the NSCL*. URL: http://nscl.msu.edu/public/science/index.html (visited on 06/01/2018).

[4] C. F. v. Weizsäcker. "Zur Theorie der Kernmassen". In: *Zeitschrift für Physik* 96.7 (July 1935), pp. 431–458. ISSN: 0044-3328. DOI: 10.1007/BF01337700. URL: https://doi.org/10.1007/BF01337700.

[5] H. A. Bethe and R. F. Bacher. "Nuclear Physics A. Stationary States of Nuclei". In: *Rev. Mod. Phys.* 8 (2 Apr. 1936), pp. 82–229. DOI: 10.1103/RevModPhys.8.82. URL: https://link.aps.org/doi/10.1103/RevModPhys.8.82.

[6] E. Rutherford. "Discussion on the structure of atomic nuclei". In: *Proceedings of the Royal Society of London A: Mathematical, Physical and Engineering Sciences* 123.792 (1929), pp. 373–390. ISSN: 0950-1207. DOI: 10.1098/rspa.1929.0074. eprint: http://rspa.royalsocietypublishing.org/content/123/792/373.full.pdf. URL: http://rspa.royalsocietypublishing.org/content/123/792/373.

[7] G. Gamow. "Mass defect curve and nuclear constitution". In: *Proceedings of the Royal Society of London A: Mathematical, Physical and Engineering Sciences* 126.803 (1930), pp. 632–644. ISSN: 0950-1207. DOI: 10.1098/rspa.1930.0032. eprint: http://rspa.royalsocietypublishing.org/content/126/803/632.full.pdf. URL: http://rspa.royalsocietypublishing.org/content/126/803/632.

[8] Einstein A. "Ist die Trägheit eines Körpers von seinem Energieinhalt abhängig?" In: *Annalen der Physik* 323.13 (1905), pp. 639–641. DOI: 10.1002/andp.19053231314. eprint: https://onlinelibrary.wiley.com/doi/pdf/10.1002/andp.19053231314. URL: https://onlinelibrary.wiley.com/doi/abs/10.1002/andp.19053231314.

[9] William D. Myers and Wladyslaw J. Swiatecki. "Nuclear masses and deformations". In: *Nuclear Physics* 81.1 (1966), pp. 1–60. ISSN: 0029-5582. DOI: https://doi.org/10.1016/0029-5582(66)90639-0. URL: http://www.sciencedirect.com/science/article/pii/0029558266906390.

[10] Elsasser, W. M. "Sur le principe de Pauli dans les noyaux". In: *J. Phys. Radium* 4.10 (1933), pp. 549–556. DOI: 10.1051/jphysrad:01933004010054900. URL: https://doi.org/10.1051/jphysrad:01933004010054900.

[11] Elsasser, W.M. “Sur le principe de Pauli dans les noyaux - II.” In: *J. Phys. Radium* 5.8 (1934), pp. 389–397. DOI: 10.1051/jphysrad:0193400508038900. URL: https://doi.org/10.1051/jphysrad:0193400508038900.

[12] B. Alex Brown. *Lecture Notes in Nuclear Structure Physics*. 2005.

[13] G. Audi. “The history of nuclidic masses and of their evaluation”. In: *International Journal of Mass Spectrometry* 251 (Apr. 2006), pp. 85–94. DOI: 10.1016/j.ijms.2006.01.048. eprint: physics/0602050.

[14] Maria Goeppert Mayer. “On Closed Shells in Nuclei. II”. In: *Phys. Rev.* 75 (12 June 1949), pp. 1969–1970. DOI: 10.1103/PhysRev.75.1969. URL: https://link.aps.org/doi/10.1103/PhysRev.75.1969.

[15] Otto Haxel, J. Hans D. Jensen, and Hans E. Suess. “On the "Magic Numbers" in Nuclear Structure”. In: *Phys. Rev.* 75 (11 June 1949), pp. 1766–1766. DOI: 10.1103/PhysRev.75.1766.2. URL: https://link.aps.org/doi/10.1103/PhysRev.75.1766.2.

[16] M.G. Mayer and J.H.D. Jensen. *Elementary Theory of Nuclear Shell Structure*. Structure of matter series. John Wiley & Sons, 1955. URL: https://books.google.com/books?id=9g9RAAAAMAAJ.

[17] W. Pauli. “Über den Zusammenhang des Abschlusses der Elektronengruppen im Atom mit der Komplexstruktur der Spektren”. In: *Zeitschrift für Physik* 31.1 (Feb. 1925), pp. 765–783. ISSN: 0044-3328. DOI: 10.1007/BF02980631. URL: https://doi.org/10.1007/BF02980631.

[18] Norman Cook. *Models of the atomic nucleus : unification through a lattice of nucleons*. Berlin Heidelberg: Springer, 2010. ISBN: 978-3642147364.

[19] O. Hen et al. “Momentum sharing in imbalanced Fermi systems”. In: *Science* 346.6209 (2014), pp. 614–617. ISSN: 0036-8075. DOI: 10.1126/science.1256785. eprint: http://science.sciencemag.org/content/346/6209/614.full.pdf. URL: http://science.sciencemag.org/content/346/6209/614.

[20] Or Hen et al. “Nucleon-nucleon correlations, short-lived excitations, and the quarks within”. In: *Rev. Mod. Phys.* 89 (4 Nov. 2017), p. 045002. DOI: 10.1103/RevModPhys.89.045002. URL: https://link.aps.org/doi/10.1103/RevModPhys.89.045002.

[21] G. Colò, P.F. Bortignon, and R.A. Broglia. “Response function beyond mean field of neutron-rich nuclei”. In: *Nuclear Physics A* 649.1 (1999). Giant Resonances, pp. 335–343. ISSN: 0375-9474. DOI: https://doi.org/10.1016/S0375-9474(99)00081-0. URL: http://www.sciencedirect.com/science/article/pii/S0375947499000810.

[22] W.H. Dickhoff and C. Barbieri. "Self-consistent Green's function method for nuclei and nuclear matter". In: *Progress in Particle and Nuclear Physics* 52.2 (2004), pp. 377–496. ISSN: 0146-6410. DOI: https://doi.org/10.1016/j.ppnp.2004.02.038. URL: http://www.sciencedirect.com/science/article/pii/S0146641004000535.

[23] J. P. Schiffer et al. "Test of Sum Rules in Nucleon Transfer Reactions". In: *Phys. Rev. Lett.* 108 (2 Jan. 2012), p. 022501. DOI: 10.1103/PhysRevLett.108.022501. URL: https://link.aps.org/doi/10.1103/PhysRevLett.108.022501.

[24] B.A. Brown. "The nuclear shell model towards the drip lines". In: *Progress in Particle and Nuclear Physics* 47.2 (2001), pp. 517–599. ISSN: 0146-6410. DOI: https://doi.org/10.1016/S0146-6410(01)00159-4. URL: http://www.sciencedirect.com/science/article/pii/S0146641001001594.

[25] M. H. Macfarlane and J. B. French. "Stripping Reactions and the Structure of Light and Intermediate Nuclei". In: *Rev. Mod. Phys.* 32 (3 July 1960), pp. 567–691. DOI: 10.1103/RevModPhys.32.567. URL: https://link.aps.org/doi/10.1103/RevModPhys.32.567.

[26] H.C. Lee. "Survey of Neutron Spectroscopic Factors and Asymmetry Dependence of Neutron Correlations in Transfer Reactions". PhD thesis. East Lansing, MI, 2010.

[27] R J Furnstahl and A Schwenk. "How should one formulate, extract and interpret 'non-observables' for nuclei?" In: *Journal of Physics G: Nuclear and Particle Physics* 37.6 (2010), p. 064005. URL: http://stacks.iop.org/0954-3899/37/i=6/a=064005.

[28] B. K. Jennings. "Non-observability of Spectroscopic Factors". In: (2011). arXiv: 1102.3721 [nucl-th].

[29] R.J. Furnstahl and H.-W. Hammer. "Are occupation numbers observable?" In: *Physics Letters B* 531.3 (2002), pp. 203–208. ISSN: 0370-2693. DOI: https://doi.org/10.1016/S0370-2693(01)01504-0. URL: http://www.sciencedirect.com/science/article/pii/S0370269301015040.

[30] T. Duguet et al. "Nonobservable nature of the nuclear shell structure: Meaning, illustrations, and consequences". In: *Phys. Rev. C* 92 (3 Sept. 2015), p. 034313. DOI: 10.1103/PhysRevC.92.034313. URL: https://link.aps.org/doi/10.1103/PhysRevC.92.034313.

[31] G.J. Kramer, H.P. Blok, and L. Lapikás. "A consistent analysis of (e,e'p) and (d,3He) experiments". In: *Nuclear Physics A* 679.3 (2001), pp. 267–286. ISSN: 0375-9474. DOI: https://doi.org/10.1016/S0375-9474(00)00379-1. URL: http://www.sciencedirect.com/science/article/pii/S0375947400003791.

[32] X. D. Liu et al. "Systematic extraction of spectroscopic factors from ^{12}C$(d,p)^{13}$C and ^{13}C$(p,d)^{12}$C reactions". In: *Phys. Rev. C* 69 (6 June 2004), p. 064313. DOI: 10.1103/PhysRevC.69.064313. URL: https://link.aps.org/doi/10.1103/PhysRevC.69.064313.

[33] J. Okolowicz et al. "Consistent analysis of one-nucleon spectroscopic factors involving weakly- and strongly-bound nucleons". In: *Physics Letters B* 757 (2016), pp. 303–306. ISSN: 0370-2693. DOI: https://doi.org/10.1016/j.physletb.2016.03.086. URL: http://www.sciencedirect.com/science/article/pii/S0370269316300673.

[34] Jenny Lee et al. "Neutron spectroscopic factors of Ni isotopes from transfer reactions". In: *Phys. Rev. C* 79 (5 May 2009), p. 054611. DOI: 10.1103/PhysRevC.79.054611. URL: https://link.aps.org/doi/10.1103/PhysRevC.79.054611.

[35] F. Lu et al. "Neutron-hole states in ^{45}Ar from ^{1}H(^{46}Ar, d) ^{45}Ar reactions". In: *Phys. Rev. C* 88 (1 July 2013), p. 017604. DOI: 10.1103/PhysRevC.88.017604. URL: https://link.aps.org/doi/10.1103/PhysRevC.88.017604.

[36] M. B. Tsang, Jenny Lee, and W. G. Lynch. "Survey of Ground State Neutron Spectroscopic Factors from Li to Cr Isotopes". In: *Phys. Rev. Lett.* 95 (22 Nov. 2005), p. 222501. DOI: 10.1103/PhysRevLett.95.222501. URL: https://link.aps.org/doi/10.1103/PhysRevLett.95.222501.

[37] Jenny Lee, M. B. Tsang, and W. G. Lynch. "Neutron spectroscopic factors from transfer reactions". In: *Phys. Rev. C* 75 (6 June 2007), p. 064320. DOI: 10.1103/PhysRevC.75.064320. URL: https://link.aps.org/doi/10.1103/PhysRevC.75.064320.

[38] M. B. Tsang et al. "Survey of Excited State Neutron Spectroscopic Factors for $Z = 8 - 28$ Nuclei". In: *Phys. Rev. Lett.* 102 (6 Feb. 2009), p. 062501. DOI: 10.1103/PhysRevLett.102.062501. URL: https://link.aps.org/doi/10.1103/PhysRevLett.102.062501.

[39] Jenny Lee et al. "Reduced neutron spectroscopic factors when using potential geometries constrained by Hartree-Fock calculations". In: *Phys. Rev. C* 73 (4 Apr. 2006), p. 044608. DOI: 10.1103/PhysRevC.73.044608. URL: https://link.aps.org/doi/10.1103/PhysRevC.73.044608.

[40] L. Lapikás. "Quasi-elastic electron scattering off nuclei". In: *Nuclear Physics A* 553 (1993), pp. 297–308. ISSN: 0375-9474. DOI: https://doi.org/10.1016/0375-9474(93)90630-G. URL: http://www.sciencedirect.com/science/article/pii/037594749390630G.

[41] S. T. Butler. "On Angular Distributions from (d, p) and (d, n) Nuclear Reactions". In: *Phys. Rev.* 80 (6 Dec. 1950), pp. 1095–1096. DOI: 10.1103/PhysRev.80.1095.2. URL: https://link.aps.org/doi/10.1103/PhysRev.80.1095.2.

[42] J. R. Holt and T. N. Marsham. "An Investigation of (d, p) Stripping Reactions I: Apparatus and Results for Aluminium". In: *Proceedings of the Physical Society. Section A* 66.3 (1953), p. 249. URL: http://stacks.iop.org/0370-1298/66/i=3/a=307.

[43] K Wimmer. "Nucleon transfer reactions with radioactive beams". In: *Journal of Physics G: Nuclear and Particle Physics* 45.3 (2018), p. 033002. URL: http://stacks.iop.org/0954-3899/45/i=3/a=033002.

[44] P.G. Hansen and J.A. Tostevin. "DIRECT REACTIONS WITH EXOTIC NUCLEI". In: *Annual Review of Nuclear and Particle Science* 53.1 (2003), pp. 219–261. DOI: 10.1146/annurev.nucl.53.041002.110406. eprint: https://doi.org/10.1146/annurev.nucl.53.041002.110406. URL: https://doi.org/10.1146/annurev.nucl.53.041002.110406.

[45] D W Bardayan. "Transfer reactions in nuclear astrophysics". In: *Journal of Physics G: Nuclear and Particle Physics* 43.4 (2016), p. 043001. URL: http://stacks.iop.org/0954-3899/43/i=4/a=043001.

[46] Alexandre Obertelli. "Nuclear structure from direct reactions with rare isotopes: observables, methods and highlights". In: *The European Physical Journal Plus* 131.9 (Sept. 2016), p. 319. ISSN: 2190-5444. DOI: 10.1140/epjp/i2016-16319-8. URL: https://doi.org/10.1140/epjp/i2016-16319-8.

[47] T. Aumann et al. "One-Neutron Knockout from Individual Single-Particle States of ^{11}Be". In: *Phys. Rev. Lett.* 84 (1 Jan. 2000), pp. 35–38. DOI: 10.1103/PhysRevLett.84.35. URL: https://link.aps.org/doi/10.1103/PhysRevLett.84.35.

[48] A. Navin et al. "Direct Evidence for the Breakdown of the $N = 8$ Shell Closure in ^{12}Be". In: *Phys. Rev. Lett.* 85 (2 July 2000), pp. 266–269. DOI: 10.1103/PhysRevLett.85.266. URL: https://link.aps.org/doi/10.1103/PhysRevLett.85.266.

[49] J.A. Tostevin et al. "Direct reaction spectroscopy of exotic nuclei". In: *Nuclear Physics A* 746 (2004). Proceedings of the Sixth International Conference on Radioactive Nuclear Beams (RNB6), pp. 166–172. ISSN: 0375-9474. DOI: https://doi.org/10.1016/j.nuclphysa.2004.09.071. URL: http://www.sciencedirect.com/science/article/pii/S037594740400925X.

[50] R. Shane et al. "Proton and neutron knockout from ^{36}Ca". In: *Phys. Rev. C* 85 (6 June 2012), p. 064612. DOI: 10.1103/PhysRevC.85.064612. URL: https://link.aps.org/doi/10.1103/PhysRevC.85.064612.

[51] V. Maddalena et al. "Single-neutron knockout reactions: Application to the spectroscopy of ^{16,17,19}C". In: *Phys. Rev. C* 63 (2 Jan. 2001), p. 024613. DOI: 10.1103/PhysRevC.63.024613. URL: https://link.aps.org/doi/10.1103/PhysRevC.63.024613.

[52] J. A. Tostevin and A. Gade. "Systematics of intermediate-energy single-nucleon removal cross sections". In: *Phys. Rev. C* 90 (5 Nov. 2014), p. 057602. DOI: 10.1103/PhysRevC.90.057602. URL: https://link.aps.org/doi/10.1103/PhysRevC.90.057602.

[53] F. Flavigny et al. "Limited Asymmetry Dependence of Correlations from Single Nucleon Transfer". In: *Phys. Rev. Lett.* 110 (12 Mar. 2013), p. 122503. DOI: 10.1103/PhysRevLett.110.122503. URL: https://link.aps.org/doi/10.1103/PhysRevLett.110.122503.

[54] J. Lee et al. "Asymmetry dependence of reduction factors from single-nucleon knockout of 30Ne at $\approx$ 230 MeV/nucleon". In: *Progress of Theoretical and Experimental Physics* 2016.8 (2016), p. 083D01. DOI: 10.1093/ptep/ptw096. eprint: /oup/backfile/content_public/journal/ptep/2016/8/10.1093_ptep_ptw096/3/ptw096.pdf. URL: http://dx.doi.org/10.1093/ptep/ptw096.

[55] Jenny Lee et al. "Neutron-Proton Asymmetry Dependence of Spectroscopic Factors in Ar Isotopes". In: *Phys. Rev. Lett.* 104 (11 Mar. 2010), p. 112701. DOI: 10.1103/PhysRevLett.104.112701. URL: https://link.aps.org/doi/10.1103/PhysRevLett.104.112701.

[56] Jenny Lee et al. "Neutron spectroscopic factors of ^{34}Ar and ^{46}Ar from (p, d) transfer reactions". In: *Phys. Rev. C* 83 (1 Jan. 2011), p. 014606. DOI: 10.1103/PhysRevC.83.014606. URL: https://link.aps.org/doi/10.1103/PhysRevC.83.014606.

[57] A. Gade et al. "Reduced Occupancy of the Deeply Bound $0d_{5/2}$ Neutron State in ^{32}Ar". In: *Phys. Rev. Lett.* 93 (4 July 2004), p. 042501. DOI: 10.1103/PhysRevLett.93.042501. URL: https://link.aps.org/doi/10.1103/PhysRevLett.93.042501.

[58] A. Gade et al. "One-neutron knockout reactions on proton-rich nuclei with $N = 16$". In: *Phys. Rev. C* 69 (3 Mar. 2004), p. 034311. DOI: 10.1103/PhysRevC.69.034311. URL: https://link.aps.org/doi/10.1103/PhysRevC.69.034311.

[59] A. Gade et al. "Reduction of spectroscopic strength: Weakly-bound and strongly-bound single-particle states studied using one-nucleon knockout reactions". In: *Phys. Rev. C* 77 (4 Apr. 2008), p. 044306. DOI: 10.1103/PhysRevC.77.044306. URL: https://link.aps.org/doi/10.1103/PhysRevC.77.044306.

[60] A. Mutschler et al. "Spectroscopy of ^{35}P using the one-proton knockout reaction". In: *Phys. Rev. C* 93 (3 Mar. 2016), p. 034333. DOI: 10.1103/PhysRevC.93.034333. URL: https://link.aps.org/doi/10.1103/PhysRevC.93.034333.

[61] H. L. Crawford et al. "Unexpected distribution of $\nu 1f_{7/2}$ strength in ^{49}**Ca**". In: *Phys. Rev. C* 95 (6 June 2017), p. 064317. DOI: 10.1103/PhysRevC.95.064317. URL: https://link.aps.org/doi/10.1103/PhysRevC.95.064317.

[62] F. M. Nunes, A. Deltuva, and June Hong. "Improved description of ^{34,36,46}Ar(p,d) transfer reactions". In: *Phys. Rev. C* 83 (3 Mar. 2011), p. 034610. DOI: 10.1103/PhysRevC.83.034610. URL: https://link.aps.org/doi/10.1103/PhysRevC.83.034610.

[63] F. Flavigny et al. "Single-particle strength from nucleon transfer in oxygen isotopes: Sensitivity to model parameters". In: *Phys. Rev. C* 97 (3 Mar. 2018), p. 034601. DOI: 10.1103/PhysRevC.97.034601. URL: https://link.aps.org/doi/10.1103/PhysRevC.97.034601.

[64] B. P. Kay, J. P. Schiffer, and S. J. Freeman. "Quenching of Cross Sections in Nucleon Transfer Reactions". In: *Phys. Rev. Lett.* 111 (4 July 2013), p. 042502. DOI: 10.1103/PhysRevLett.111.042502. URL: https://link.aps.org/doi/10.1103/PhysRevLett.111.042502.

[65] N. K. Timofeyuk and R. C. Johnson. "Nonlocality in Deuteron Stripping Reactions". In: *Phys. Rev. Lett.* 110 (11 Mar. 2013), p. 112501. DOI: 10.1103/PhysRevLett.110.112501. URL: https://link.aps.org/doi/10.1103/PhysRevLett.110.112501.

[66] N. K. Timofeyuk and R. C. Johnson. "Nonlocality in the adiabatic model of $A(d,p)B$ reactions". In: *Phys. Rev. C* 87 (6 June 2013), p. 064610. DOI: 10.1103/PhysRevC.87.064610. URL: https://link.aps.org/doi/10.1103/PhysRevC.87.064610.

[67] F. Flavigny et al. "Nonsudden Limits of Heavy-Ion Induced Knockout Reactions". In: *Phys. Rev. Lett.* 108 (25 June 2012), p. 252501. DOI: 10.1103/PhysRevLett.108.252501. URL: https://link.aps.org/doi/10.1103/PhysRevLett.108.252501.

[68] C. Louchart et al. "Nucleon removal from unstable nuclei investigated via intranuclear cascade". In: *Phys. Rev. C* 83 (1 Jan. 2011), p. 011601. DOI: 10.1103/PhysRevC.83.011601. URL: https://link.aps.org/doi/10.1103/PhysRevC.83.011601.

[69] Y. L. Sun et al. "Experimental study of the knockout reaction mechanism using ^{14}O at 60 MeV/nucleon". In: *Phys. Rev. C* 93 (4 Apr. 2016), p. 044607. DOI: 10.1103/PhysRevC.93.044607. URL: https://link.aps.org/doi/10.1103/PhysRevC.93.044607.

[70] R. J. Charity, L. G. Sobotka, and W. H. Dickhoff. "Asymmetry Dependence of Proton Correlations". In: *Phys. Rev. Lett.* 97 (16 Oct. 2006), p. 162503. DOI: 10.1103/PhysRevLett.97.162503. URL: https://link.aps.org/doi/10.1103/PhysRevLett.97.162503.

[71] R. J. Charity et al. "Dispersive-optical-model analysis of the asymmetry dependence of correlations in Ca isotopes". In: *Phys. Rev. C* 76 (4 Oct. 2007), p. 044314. DOI: 10.1103/PhysRevC.76.044314. URL: https://link.aps.org/doi/10.1103/PhysRevC.76.044314.

[72] C. BARBIERI and W. H. DICKHOFF. "SPECTROSCOPIC FACTORS IN 16O AND NUCLEON ASYMMETRY". In: *International Journal of Modern Physics A* 24.11 (2009), pp. 2060–2068. DOI: 10.1142/S0217751X09045625. eprint: https://www.worldscientific.com/doi/pdf/10.1142/S0217751X09045625. URL: https://www.worldscientific.com/doi/abs/10.1142/S0217751X09045625.

[73] N. K. Timofeyuk. "New Insight into the Observation of Spectroscopic Strength Reduction in Atomic Nuclei: Implication for the Physical Meaning of Spectroscopic Factors". In: *Phys. Rev. Lett.* 103 (24 Dec. 2009), p. 242501. DOI: 10.1103/PhysRevLett.103.242501. URL: https://link.aps.org/doi/10.1103/PhysRevLett.103.242501.

[74] Ø. Jensen et al. "Quenching of Spectroscopic Factors for Proton Removal in Oxygen Isotopes". In: *Phys. Rev. Lett.* 107 (3 July 2011), p. 032501. DOI: 10.1103/PhysRevLett.107.032501. URL: https://link.aps.org/doi/10.1103/PhysRevLett.107.032501.

[75] L. Atar et al. "Quasifree (p, $2p$) Reactions on Oxygen Isotopes: Observation of Isospin Independence of the Reduced Single-Particle Strength". In: *Phys. Rev. Lett.* 120 (5 Jan. 2018), p. 052501. DOI: 10.1103/PhysRevLett.120.052501. URL: https://link.aps.org/doi/10.1103/PhysRevLett.120.052501.

[76] Shoichiro Kawase et al. "Exclusive quasi-free proton knockout from oxygen isotopes at intermediate energies". In: *Progress of Theoretical and Experimental Physics* 2018.2 (2018), p. 021D01. DOI: 10.1093/ptep/pty011. eprint: /oup/backfile/content_public/journal/ptep/2018/2/10.1093_ptep_pty011/1/pty011.pdf. URL: http://dx.doi.org/10.1093/ptep/pty011.

[77] Ian J Thompson and Filomena M Nunes. *Nuclear reactions for astrophysics: principles, calculation and applications of low-energy reactions*. Cambridge: Cambridge Univ. Press, 2009. URL: https://cds.cern.ch/record/1190499.

[78] N. Austern. *Direct nuclear reaction theories*. Interscience monographs and texts in physics and astronomy. Wiley-Interscience, 1970. ISBN: 9780471037705. URL: https://books.google.com/books?id=FVN9AAAAIAAJ.

[79] M.G. Moore. *PHY852 Lecture Notes: Introduction to Scattering Theory*. 2008. URL: http://web.pa.msu.edu/people/mmoore/852scattering.pdf.

[80] R. C. Johnson and P. J. R. Soper. "Contribution of Deuteron Breakup Channels to Deuteron Stripping and Elastic Scattering". In: *Phys. Rev. C* 1 (3 Mar. 1970), pp. 976–990. DOI: 10.1103/PhysRevC.1.976. URL: https://link.aps.org/doi/10.1103/PhysRevC.1.976.

[81] R.C. Johnson and P.J.R. Soper. "Relation between the deuteron and nucleon optical potentials". In: *Nuclear Physics A* 182.3 (1972), pp. 619–624. ISSN: 0375-9474. DOI: https://doi.org/10.1016/0375-9474(72)90540-4. URL: http://www.sciencedirect.com/science/article/pii/0375947472905404.

[82] F. M. Nunes and A. Deltuva. "Adiabatic approximation versus exact Faddeev method for (d,p) and (p,d) reactions". In: *Phys. Rev. C* 84 (3 Sept. 2011), p. 034607. DOI: 10.1103/PhysRevC.84.034607. URL: https://link.aps.org/doi/10.1103/PhysRevC.84.034607.

[83] P J A Buttle and L J B Goldfarb. "Finite range effects in deuteron stripping processes". In: *Proceedings of the Physical Society* 83.5 (1964), p. 701. URL: http://stacks.iop.org/0370-1328/83/i=5/a=302.

[84] A. Deltuva. "Three-body direct nuclear reactions: Nonlocal optical potential". In: *Phys. Rev. C* 79 (2 Feb. 2009), p. 021602. DOI: 10.1103/PhysRevC.79.021602. URL: https://link.aps.org/doi/10.1103/PhysRevC.79.021602.

[85] F Perey. "F. Perey and B. Buck, Nucl. Phys. 32, 353 (1962)". In: *Nucl. Phys.* 32 (1962), p. 353.

[86] G. W. Bailey, N. K. Timofeyuk, and J. A. Tostevin. "Sensitivity of (d, p) Reactions to High $n-p$ Momenta and the Consequences for Nuclear Spectroscopy Studies". In: *Phys. Rev. Lett.* 117 (16 Oct. 2016), p. 162502. DOI: 10.1103/PhysRevLett.117.162502. URL: https://link.aps.org/doi/10.1103/PhysRevLett.117.162502.

[87] G. W. Bailey, N. K. Timofeyuk, and J. A. Tostevin. "Nonlocal nucleon-nucleus interactions in (d,p) reactions: Role of the deuteron D state". In: *Phys. Rev. C* 95 (2 Feb. 2017), p. 024603. DOI: 10.1103/PhysRevC.95.024603. URL: https://link.aps.org/doi/10.1103/PhysRevC.95.024603.

[88] L. J. Titus and F. M. Nunes. "Testing the Perey effect". In: *Phys. Rev. C* 89 (3 Mar. 2014), p. 034609. DOI: 10.1103/PhysRevC.89.034609. URL: https://link.aps.org/doi/10.1103/PhysRevC.89.034609.

[89] L. J. Titus, F. M. Nunes, and G. Potel. "Explicit inclusion of nonlocality in (d,p) transfer reactions". In: *Phys. Rev. C* 93 (1 Jan. 2016), p. 014604. DOI: 10.1103/

PhysRevC.93.014604. URL: https://link.aps.org/doi/10.1103/PhysRevC.93.014604.

[90] L. Titus. "Effects of Nonlocality on Transfer Reactions". PhD thesis. East Lansing, MI, 2015.

[91] A. Ross et al. "Effects of nonlocal potentials on (p, d) transfer reactions". In: *Phys. Rev. C* 92 (4 Oct. 2015), p. 044607. DOI: 10.1103/PhysRevC.92.044607. URL: https://link.aps.org/doi/10.1103/PhysRevC.92.044607.

[92] S. J. Waldecker and N. K. Timofeyuk. "Implications for (d, p) reaction theory from nonlocal dispersive optical model analysis of ^{40}Ca$(d, p)^{41}$Ca". In: *Phys. Rev. C* 94 (3 Sept. 2016), p. 034609. DOI: 10.1103/PhysRevC.94.034609. URL: https://link.aps.org/doi/10.1103/PhysRevC.94.034609.

[93] A. E. Lovell et al. "Energy dependence of nonlocal optical potentials". In: *Phys. Rev. C* 96 (5 Nov. 2017), p. 051601. DOI: 10.1103/PhysRevC.96.051601. URL: https://link.aps.org/doi/10.1103/PhysRevC.96.051601.

[94] R.L. Varner et al. "A global nucleon optical model potential". In: *Physics Reports* 201.2 (1991), pp. 57–119. ISSN: 0370-1573. DOI: https://doi.org/10.1016/0370-1573(91)90039-O. URL: http://www.sciencedirect.com/science/article/pii/037015739190039O.

[95] X. Liu. "Study of (p, d) Reactions on ^{13}C, ^{11}B, and ^{10}Be In Inverse Kinematics". PhD thesis. East Lansing, MI, 2005.

[96] J. -P. Jeukenne, A. Lejeune, and C. Mahaux. "Microscopic calculation of the symmetry and Coulomb components of the complex optical-model potential". In: *Phys. Rev. C* 15 (1 Jan. 1977), pp. 10–29. DOI: 10.1103/PhysRevC.15.10. URL: https://link.aps.org/doi/10.1103/PhysRevC.15.10.

[97] J.-P. Jeukenne, A. Lejeune, and C. Mahaux. "Optical-model potential in finite nuclei from Reid's hard core interaction". In: *Phys. Rev. C* 16 (1 July 1977), pp. 80–96. DOI: 10.1103/PhysRevC.16.80. URL: https://link.aps.org/doi/10.1103/PhysRevC.16.80.

[98] Roderick V Reid. "Local phenomenological nucleon-nucleon potentials". In: *Annals of Physics* 50.3 (1968), pp. 411–448. ISSN: 0003-4916. DOI: https://doi.org/10.1016/0003-4916(68)90126-7. URL: http://www.sciencedirect.com/science/article/pii/0003491668901267.

[99] S. Mellema et al. "Microscopic and conventional optical model analysis of fast neutron scattering from ^{54,56}Fe". In: *Phys. Rev. C* 28 (6 Dec. 1983), pp. 2267–2277. DOI:

10.1103/PhysRevC.28.2267. URL: https://link.aps.org/doi/10.1103/PhysRevC.28.2267.

[100] L. F. Hansen et al. "Test of microscopic optical model potentials for neutron elastic scattering at 14.6 MeV over a wide mass range". In: *Phys. Rev. C* 31 (1 Jan. 1985), pp. 111–119. DOI: 10.1103/PhysRevC.31.111. URL: https://link.aps.org/doi/10.1103/PhysRevC.31.111.

[101] N. Olsson et al. "Microscopic and conventional optical model analysis of neutron elastic scattering at 21.6 MeV over a wide mass range". In: *Nuclear Physics A* 472.2 (1987), pp. 237–268. ISSN: 0375-9474. DOI: https://doi.org/10.1016/0375-9474(87)90209-0. URL: http://www.sciencedirect.com/science/article/pii/0375947487902090.

[102] H. S. Camarda, F. S. Dietrich, and T. W. Phillips. "Microscopic optical-model calculations of neutron total cross sections and cross section differences". In: *Phys. Rev. C* 39 (5 May 1989), pp. 1725–1729. DOI: 10.1103/PhysRevC.39.1725. URL: https://link.aps.org/doi/10.1103/PhysRevC.39.1725.

[103] B. Alex Brown. "New Skyrme interaction for normal and exotic nuclei". In: *Phys. Rev. C* 58 (1 July 1998), pp. 220–231. DOI: 10.1103/PhysRevC.58.220. URL: https://link.aps.org/doi/10.1103/PhysRevC.58.220.

[104] B.A Brown, W.A Richter, and R Lindsay. "Displacement energies with the Skyrme Hartree–Fock method". In: *Physics Letters B* 483.1 (2000), pp. 49–54. ISSN: 0370-2693. DOI: https://doi.org/10.1016/S0370-2693(00)00589-X. URL: http://www.sciencedirect.com/science/article/pii/S037026930000589X.

[105] B. A. Brown, S. Typel, and W. A. Richter. "Interaction cross sections for light neutron-rich nuclei". In: *Phys. Rev. C* 65 (1 Dec. 2001), p. 014612. DOI: 10.1103/PhysRevC.65.014612. URL: https://link.aps.org/doi/10.1103/PhysRevC.65.014612.

[106] W. A. Richter and B. A. Brown. "Nuclear charge densities with the Skyrme Hartree-Fock method". In: *Phys. Rev. C* 67 (3 Mar. 2003), p. 034317. DOI: 10.1103/PhysRevC.67.034317. URL: https://link.aps.org/doi/10.1103/PhysRevC.67.034317.

[107] A. E. Lovell et al. "Uncertainty quantification for optical model parameters". In: *Phys. Rev. C* 95 (2 Feb. 2017), p. 024611. DOI: 10.1103/PhysRevC.95.024611. URL: https://link.aps.org/doi/10.1103/PhysRevC.95.024611.

[108] E.J. Stephenson et al. "Implications of far-side dominance for the disagreement between distorted wave theory and well-matched intermediate energy (d, p) reactions". In: *Physics Letters B* 171.4 (1986), pp. 358–362. ISSN: 0370-2693. DOI: https://doi.

org/10.1016/0370-2693(86)91420-6. URL: http://www.sciencedirect.com/science/article/pii/0370269386914206.

[109] R.C. Johnson, E.J. Stephenson, and J.A. Tostevin. "Nature of the amplitudes missing from adiabatic distorted-wave models of medium energy (d, p) and (p, d) reactions". In: *Nuclear Physics A* 505.1 (1989), pp. 26–66. ISSN: 0375-9474. DOI: https://doi.org/10.1016/0375-9474(89)90415-6. URL: http://www.sciencedirect.com/science/article/pii/0375947489904156.

[110] M. Igarashi J. A. Tostevin University of Surrey version of the code TWOFNR (of M. Toyama, N. Kishida), and code FRONT (private communication).

[111] R. Fox and J. Tompkins. *NSCL Data Acquisition Documentation*. URL: http://docs.nscl.msu.edu/daq/newsite/home.php (visited on 05/31/2018).

[112] R. Fox and J. Tompkins. *SpecTcl Home Page*. URL: http://docs.nscl.msu.edu/daq/spectcl/index.htm (visited on 05/31/2018).

[113] F. Marti et al. "Commissioning of the Coupled Cyclotron system at NSCL". In: *AIP Conference Proceedings* 600.1 (2001), pp. 64–68. DOI: 10.1063/1.1435199. eprint: http://aip.scitation.org/doi/pdf/10.1063/1.1435199. URL: http://aip.scitation.org/doi/abs/10.1063/1.1435199.

[114] B.-M. Sherrill. "Scientific Opportunities with the NSCL Coupled Cyclotron Facility". In: *Progress of Theoretical Physics Supplement* 146 (2002), pp. 60–69. DOI: 10.1143/PTPS.146.60. eprint: /oup/backfile/content_public/journal/ptps/146/10.1143/ptps.146.60/2/146-60.pdf. URL: http://dx.doi.org/10.1143/PTPS.146.60.

[115] D. J. Morrissey. "The Coupled Cyclotron Project at the NSCL". In: *Nuclear Physics A* 616 (Feb. 1997), pp. 45–55. DOI: 10.1016/S0375-9474(97)00073-0.

[116] D.J. Morrissey et al. "Commissioning the A1900 projectile fragment separator". In: *Nuclear Instruments and Methods in Physics Research Section B: Beam Interactions with Materials and Atoms* 204 (2003). 14th International Conference on Electromagnetic Isotope Separators and Techniques Related to their Applications, pp. 90–96. ISSN: 0168-583X. DOI: http://dx.doi.org/10.1016/S0168-583X(02)01895-5. URL: http://www.sciencedirect.com/science/article/pii/S0168583X02018955.

[117] R. Meharchand. "Spectroscopy of ^{12}Be Using the (^{7}Li,^{7}Be) Reaction in Inverse Kinematics". PhD thesis. East Lansing, MI, 2009.

[118] M.S. Wallace et al. "The high resolution array (HiRA) for rare isotope beam experiments". In: *Nuclear Instruments and Methods in Physics Research Section A: Accelerators, Spectrometers, Detectors and Associated Equipment* 583.2 (2007), pp. 302–

312. ISSN: 0168-9002. DOI: https://doi.org/10.1016/j.nima.2007.08.248. URL: http://www.sciencedirect.com/science/article/pii/S016890020701947X.

[119] A. H. Wuosmaa et al. "Ground-state properties of ^{5}H from the ^{6}He(d,^{3}He)^{5}H reaction". In: *Phys. Rev. C* 95 (1 Jan. 2017), p. 014310. DOI: 10.1103/PhysRevC.95.014310. URL: https://link.aps.org/doi/10.1103/PhysRevC.95.014310.

[120] A. M. Rogers et al. "Ground-State Proton Decay of ^{69}Br and Implications for the ^{68}Se Astrophysical Rapid Proton-Capture Process Waiting Point". In: *Phys. Rev. Lett.* 106 (25 June 2011), p. 252503. DOI: 10.1103/PhysRevLett.106.252503. URL: https://link.aps.org/doi/10.1103/PhysRevLett.106.252503.

[121] K. W. Brown et al. "Observation of Long-Range Three-Body Coulomb Effects in the Decay of ^{16}Ne". In: *Phys. Rev. Lett.* 113 (23 Dec. 2014), p. 232501. DOI: 10.1103/PhysRevLett.113.232501. URL: https://link.aps.org/doi/10.1103/PhysRevLett.113.232501.

[122] V. Henzl et al. "Angular dependence in proton-proton correlation functions in central ^{40}Ca + ^{40}Ca and ^{48}Ca + ^{48}Ca reactions". In: *Phys. Rev. C* 85 (1 Jan. 2012), p. 014606. DOI: 10.1103/PhysRevC.85.014606. URL: https://link.aps.org/doi/10.1103/PhysRevC.85.014606.

[123] C. A. Klein. "Bandgap Dependence and Related Features of Radiation Ionization Energies in Semiconductors". In: *Journal of Applied Physics* 39 (Mar. 1968), pp. 2029–2038. DOI: 10.1063/1.1656484.

[124] Glenn F Knoll. *Radiation detection and measurement; 4th ed.* New York, NY: Wiley, 2010. URL: https://cds.cern.ch/record/1300754.

[125] George L. Engel et al. "A multi-channel integrated circuit for use in low- and intermediate-energy nuclear physics-HINP16C". In: *Nuclear Instruments and Methods in Physics Research Section A: Accelerators, Spectrometers, Detectors and Associated Equipment* 573.3 (2007), pp. 418–426. ISSN: 0168-9002. DOI: http://dx.doi.org/10.1016/j.nima.2006.12.052. URL: http://www.sciencedirect.com/science/article/pii/S0168900207000058.

[126] A Matta et al. "NPTool: a simulation and analysis framework for low-energy nuclear physics experiments". In: *Journal of Physics G: Nuclear and Particle Physics* 43.4 (2016), p. 045113. URL: http://stacks.iop.org/0954-3899/43/i=4/a=045113.

[127] D. Bazin et al. "The S800 spectrograph". In: *Nuclear Instruments and Methods in Physics Research Section B: Beam Interactions with Materials and Atoms* 204 (2003). 14th International Conference on Electromagnetic Isotope Separators and Techniques Related to their Applications, pp. 629–633. ISSN: 0168-583X. DOI: http://dx.doi.

org/10.1016/S0168-583X(02)02142-0. URL: http://www.sciencedirect.com/science/article/pii/S0168583X02021420.

[128] J Yurkon et al. "Focal plane detector for the S800 high-resolution spectrometer". In: *Nuclear Instruments and Methods in Physics Research Section A: Accelerators, Spectrometers, Detectors and Associated Equipment* 422.1 (1999), pp. 291–295. ISSN: 0168-9002. DOI: http://dx.doi.org/10.1016/S0168-9002(98)00960-7. URL: http://www.sciencedirect.com/science/article/pii/S0168900298009607.

[129] Joseph Ladislas Wiza. "Microchannel plate detectors". In: *Nuclear Instruments and Methods* 162.1 (1979), pp. 587–601. ISSN: 0029-554X. DOI: https://doi.org/10.1016/0029-554X(79)90734-1. URL: http://www.sciencedirect.com/science/article/pii/0029554X79907341.

[130] A.M. Rogers et al. "Tracking rare-isotope beams with microchannel plates". In: *Nuclear Instruments and Methods in Physics Research Section A: Accelerators, Spectrometers, Detectors and Associated Equipment* 795 (2015), pp. 325–334. ISSN: 0168-9002. DOI: http://dx.doi.org/10.1016/j.nima.2015.05.070. URL: http://www.sciencedirect.com/science/article/pii/S0168900215007305.

[131] A.M. Rogers. "Study of ^{69}Br Ground State Proton Emission and Effects on the rp-Process ^{68}Se Waiting Point". PhD thesis. East Lansing, MI, 2009.

[132] Rene Brun and Fons Rademakers. "ROOT — An object oriented data analysis framework". In: *Nuclear Instruments and Methods in Physics Research Section A: Accelerators, Spectrometers, Detectors and Associated Equipment* 389.1 (1997). New Computing Techniques in Physics Research V, pp. 81–86. ISSN: 0168-9002. DOI: https://doi.org/10.1016/S0168-9002(97)00048-X. URL: http://www.sciencedirect.com/science/article/pii/S016890029700048X.

[133] J. Manfredi et al. "On determining dead layer and detector thicknesses for a position-sensitive silicon detector". In: *Nuclear Instruments and Methods in Physics Research Section A: Accelerators, Spectrometers, Detectors and Associated Equipment* 888 (2018), pp. 177–183. ISSN: 0168-9002. DOI: https://doi.org/10.1016/j.nima.2017.12.082. URL: http://www.sciencedirect.com/science/article/pii/S016890021731505X.

[134] M. R. Bhat. *Evaluated Nuclear Structure Data File (ENSDF)*. Ed. by S. M. Qaim. Data extracted using the NNDC On-Line Data Service from the ENSDF database, file revised as of September 29, 2017. Berlin, Germany, 1992.

[135] B. L. Wall et al. "Dead layer on silicon p–i–n diode charged-particle detectors". In: *Nucl. Instrum. Methods Phys. Res., Sect. A* 744.Supplement C (2014), pp. 73–79. ISSN: 0168-9002. DOI: https://doi.org/10.1016/j.nima.2013.12.048. URL: http://www.sciencedirect.com/science/article/pii/S016890021301752X.

[136] David D. Cohen et al. "Silicon detector dead layer thickness estimates using proton bremsstrahlung from low atomic number targets". In: *X-Ray Spectrometry* 37.2 (2008), pp. 125–128. ISSN: 1097-4539. DOI: 10.1002/xrs.1033. URL: http://dx.doi.org/10.1002/xrs.1033.

[137] Micron Semiconductor LTD. *Private Communication*. 2017.

[138] Alan G. Seamster, Ray E.L. Green, and Ralph G. Korteling. "Silicon detector ΔE, E particle identification: a theoretically based analysis algorithm and remarks on the fundamental limits to the resolution of particle type by ΔE, E measurements". In: *Nuclear Instruments and Methods* 145.3 (1977), pp. 583–591. ISSN: 0029-554X. DOI: https://doi.org/10.1016/0029-554X(77)90590-0. URL: http://www.sciencedirect.com/science/article/pii/0029554X77905900.

[139] J. F. Ziegler, M. D. Ziegler, and J. P. Biersack. "SRIM - The stopping and range of ions in matter (2010)". In: *Nucl. Instrum. Methods Phys. Res., Sect. B* 268 (June 2010), pp. 1818–1823. DOI: 10.1016/j.nimb.2010.02.091. URL: http://www.sciencedirect.com/science/article/pii/S0168583X10001862.

[140] A. Sanetullaev. "Neutron Spectroscopic Factors of ^{56}Ni via ^{56}Ni$(p,d)^{55}$Ni Reaction in Inverse Kinematics". PhD thesis. Michigan State University, 2012.

[141] J.R. Winkelbauer. "Precision Measurement of Isospin Diffusion in Peripheral Sn+Sn Collisions at 70 MeV/u". PhD thesis. Michigan State University, 2015.

[142] Eremenko, V. et al. "Towards a Faddeev-AGS description of (d, p) reactions with heavy nuclei: Regularizing integrals with Coulomb functions." In: *EPJ Web of Conferences* 113 (2016), p. 03016. DOI: 10.1051/epjconf/201611303016. URL: https://doi.org/10.1051/epjconf/201611303016.

[143] A. E. Lovell and F. M. Nunes. "Constraining transfer cross sections using Bayes' theorem". In: *Phys. Rev. C* 97 (6 June 2018), p. 064612. DOI: 10.1103/PhysRevC.97.064612. URL: https://link.aps.org/doi/10.1103/PhysRevC.97.064612.

[144] Toshimi Suda and Haik Simon. "Prospects for electron scattering on unstable, exotic nuclei". In: *Progress in Particle and Nuclear Physics* 96 (2017), pp. 1–31. ISSN: 0146-6410. DOI: https://doi.org/10.1016/j.ppnp.2017.04.002. URL: http://www.sciencedirect.com/science/article/pii/S0146641017300376.

[145] Thomas Neff. "Microscopic Calculation of the ^{3}He$(\alpha,\gamma)^7$Be and ^{3}H$(\alpha,\gamma)^7$Li Capture Cross Sections Using Realistic Interactions". In: *Phys. Rev. Lett.* 106 (4 Jan. 2011), p. 042502. DOI: 10.1103/PhysRevLett.106.042502. URL: https://link.aps.org/doi/10.1103/PhysRevLett.106.042502.

[146] Petr Navrátil and Sofia Quaglioni. "Ab Initio Many-Body Calculations of the $^3\mathrm{H}(d,n)^4\mathrm{He}$ and $^3\mathrm{He}(d,p)^4\mathrm{He}$ Fusion Reactions". In: *Phys. Rev. Lett.* 108 (4 Jan. 2012), p. 042503. DOI: 10.1103/PhysRevLett.108.042503. URL: https://link.aps.org/doi/10.1103/PhysRevLett.108.042503.

[147] Serdar Elhatisari et al. "Ab initio alpha-alpha scattering". In: *Nature* 528 (Dec. 2015). URL: http://dx.doi.org/10.1038/nature16067.

[148] F Raimondi et al. "7 Li(d , p) 8 Li transfer reaction in the NCSM/RGM approach". In: *Journal of Physics: Conference Series* 981.1 (2018), p. 012006. URL: http://stacks.iop.org/1742-6596/981/i=1/a=012006.